FANO CONTROL OF PLASMONIC DOUBLE-RESONANT SYSTEMS

A THESIS SUBMITTED TO
THE GRADUATE SCHOOL OF NATURAL AND APPLIED SCIENCES
OF
MIDDLE EAST TECHNICAL UNIVERSITY

BY

SELEN POSTACI

IN PARTIAL FULFILLMENT OF THE REQUIREMENTS
FOR
THE DEGREE OF DOCTOR OF PHILOSOPHY
IN
PHYSICS

FEBRUARY 2021

Approval of the thesis:

FANO CONTROL OF PLASMONIC DOUBLE-RESONANT SYSTEMS

submitted by **SELEN POSTACI** in partial fulfillment of the requirements for the degree of **Doctor of Philosophy in Physics Department, Middle East Technical University** by,

Prof. Dr. Halil Kalıpçılar
Dean, Graduate School of **Natural and Applied Sciences** _____

Prof. Dr. Altuğ Özpineci
Head of Department, **Physics** _____

Assoc. Prof. Dr. Alpan Bek
Supervisor, **Physics, METU** _____

Assoc. Prof. Dr. Mehmet Emre Taşgın
Co-supervisor, **Institute of Nuclear Sciences, Hacettepe Uni.** _____

Examining Committee Members:

Assoc. Prof. Dr. Serhat Çakır
Physics, METU _____

Assoc. Prof. Dr. Alpan Bek
Physics, METU _____

Assoc. Prof. Dr. Sinan Balcı
Photonics, İzmir Institute of Technology _____

Assoc. Prof. Dr. Hande Toffoli
Physics, METU _____

Assist. Prof. Dr. Rasim Volga Ovalı
Physics, Recep Tayyip Erdoğan University _____

Date: 12.02.2021

I hereby declare that all information in this document has been obtained and presented in accordance with academic rules and ethical conduct. I also declare that, as required by these rules and conduct, I have fully cited and referenced all material and results that are not original to this work.

Name, Surname: Selen Postacı

Signature :

ABSTRACT

FANO CONTROL OF PLASMONIC DOUBLE-RESONANT SYSTEMS

Postacı, Selen
Ph.D., Department of Physics
Supervisor: Assoc. Prof. Dr. Alpan Bek
Co-Supervisor: Assoc. Prof. Dr. Mehmet Emre Taşgın

February 2021, 90 pages

The nonlinear response of plasmonic nanostructures can be enhanced as a result of the localization of the incident field into nm-size regions, called hot spots. The Raman signal of a molecule can be enhanced by adsorbing it to the surface of a plasmonic structure. However, the hot spot enhancement is limited with the modification of the vibrational modes, the breakdown of the molecule, and transition to the tunneling regime. The analytical treatment that is presented in this study aims to circumvent these limitations by introducing the nonlinear path interference effects. Coupling a quantum emitter to the double-resonant metal nanostructure yields to path interference, enabling the further manipulation of the SERS signal. The results denote that an extra enhancement of 10^2-10^3 factors can occur, which does not alter the existing hot spot field intensities. Besides the analytical results, 3 Dimensional solutions of Maxwell equations are also utilized in order to understand the effects of retardation on the system.

In the second part, the second harmonic response of a double-resonant metal nanostructure is studied with the coupling of a quantum emitter. The quantum emitter is driven with a source where changing the pump strength enables the modification of

the second converted field intensity. It is observed that as the nonlinear response of the system is enhanced, the nonclassicality measure also shows an increase. This result indicates that pumping the quantum emitter with a source provides the opportunity to modify the nonlinear response via Fano type resonances in plasmonic structures.

Keywords: plasmonics, Fano resonances, surface enhanced Raman scattering, second harmonic generation, quantum entanglement

ÖZ

PLAZMONİK ÇİFT ÇINLAMALI SİSTEMLERDE FANO KONTROLÜ

Postacı, Selen
Doktora, Fizik Bölümü
Tez Yöneticisi: Doç. Dr. Alpan Bek
Ortak Tez Yöneticisi: Doç. Dr. Mehmet Emre Taşgın

Şubat 2021 , 90 sayfa

Plazmonik yapıların doğrusal olmayan tepkileri, nanometre boyutlu sıcak noktalarında oluşabilen, güçlü bir şekilde lokalize edilmiş elektrik alan sayesinde güçlendirilebilir. Bir molekül, plazmonik bir yapının yüzeyine, sıcak nokta civarına yerleştirilirse bu etkiler sayesinde Raman saçılmasında artış sağlanabilir. Fakat sıcak noktada elektrik alan artırımı ile yapılabilecek Raman sinyali güçlendirilmesinde bazı kısıtlamalar vardır. Molekülün titreşim kiplerinin değişikliğe uğraması, molekülün bozunumu ve akım tünelleme durumuna geçmesi bunlar arasında sayılabilir. Bu çalışmada doğrusal olmayan Fano çınlama etkileri kullanılarak bu kısıtlamaların önüne geçecek bir mekanizma geliştirilmesi amaçlanmıştır. Bahsedilen çift çınlamalı plazmonik yapıya bir kuantum yayıcı çiftlenmesi ile yüzeyde güçlendirilmiş Raman sinyalinin kontrolü amaçlanmıştır. Bu teknik ile sıcak noktalarda oluşan elektrik alan artırımına ek olarak 100-1000 çarpanlık ek bir artırım elde edilebilmektedir. Bunu yaparken sıcak nokta üzerindeki elektrik alan şiddetinde herhangi bir değişim meydana gelmediği gösterilmiştir. Dolayısıyla elektrik alan artırımında bahsedilen kısıtlamalar ortadan kalkmaktadır. Sistemin analitik olarak çalışılmasının yanı sıra, 3 boyutlu

Maxwell denklemi çözümleri kullanılarak geciktirme etkileri de incelenmiştir.

Tezin ikinci kısmında, çift çınlama yapısına sahip plazmonik bir nanoyapı kuantum yayıcı ile çiftlenerek, oluşan sistemin ikinci harmonik çevrim tepkisi çalışılmıştır. Bir kaynak ile beslenen kuantum yayıcı sayesinde, bu beslemenin gücünü değiştirerek sistemin ikinci harmonik sinyalinin kontrol edilebilmesi amaçlanmıştır. Çiftlenmiş plazmonik yapı-kuantum yayıcı sisteminin doğrusal olmayan tepkisindeki artışa, klasik olmayan özelliklerindeki bir artış eşlik etmektedir. Bu durum ikinci harmonik çevrim sinyalinin güçlendirilmesinde girişim yolu etkilerinin yer aldığını göstermektedir. Bundan çıkarılabilecek sonuç, çift çınlamalı plazmonik yapıya çiftlenen kuantum yayıcının bir kaynak ile beslenmesi yapılarak sistemin doğrusal olmayan tepkilerinin Fano tipi çınlamalar kullanılarak kontrol edilebileceğidir.

Anahtar Kelimeler: plazmonik, Fano rezonans, yüzey zenginleştirilmiş Raman saçılması, ikinci harmonik üretimi, kuantum dolanıklık

To my husband Emirhan and my son Demir

ACKNOWLEDGMENTS

I would like to express my deepest gratitude to my supervisor Assoc. Dr. Alpan Bek for his guidance, understanding and support through my Ph.D. study. I am deeply thankful to my co-supervisor Assoc. Dr. Mehmet Emre Taşgın for sharing his knowledge, for his lessons and discussions throughout the years. I also would like to thank Dr. Rasim Volga Ovalı, Dr. Bilge Can Yıldız and Dr. Mehmet Günay for their kind help, valuable comments and all the knowledge they share with me. I kindly acknowledge that this project is supported by the Turkish Scientific and Technical Research Council, TUBITAK with grant No. 119F101.

My special thanks are for my parents, Emin and Özlem Saatci, who always supported me and believed that I could manage to obtain any achievement I desire for. Their support in this work is more than it seems, they paused their lives to take care of my son for countless times when I have to study for my thesis. My sister Özge and my brother Murat always bring joy and help whenever I needed, life is always cheerful when I am with them. I am endlessly grateful for my family.

Throughout my study I was lucky to be in company with many friends that I can share everything, discuss physics and have unconditional support from them. I would like to thank Elif Sarıgül Duman and İbrahim Murat Öztürk for their assistance especially when we take the graduate courses together. I also thank Ayşe Nihan Şatgeldi for her sincere friendship for over a decade. I am thankful to Özge Aktaş who is a dear friend and an excellent travel partner. I may not be able to pass the qualification exam with preserving my sanity without her fellowship. Furthermore, I would like to thank Elif Tuğçe Koç, whom I feel very lucky to have her company for almost 20 years. Over the years that we grew up together, I cannot count how many times she supported me.

When I started to work at Tübitak, I couldn't imagine to meet and work with a group of such joyful young friends, Özdenur Uçar, Alperen Çakıroğlu, Farukcan Şoray and Sinan Bosna. You all are the reason that I laugh so much. I thank Sinan for sharing

all his knowledge and experience with me. His constant patience while I write this thesis is very much appreciated.

I am deeply grateful for the little family that I have. My husband Emirhan, my love and my companion in life, makes my life beautiful in every way. Without his support and guidance, this thesis would still be incomplete. Now I am glad that we both can remove the laptops from our dining table. Closing the PhD chapter of our lives, I look forward what life brings us.

Last but not least, I am so lucky to be the mother of my beloved son Demir. It is always thought that parents raise the kids, but he teaches me more than I teach him. Whatever I do, my motivation is always to set a good example and I will always try to be a mother he can be proud of.

TABLE OF CONTENTS

ABSTRACT v

ÖZ vii

ACKNOWLEDGMENTS x

TABLE OF CONTENTS xii

LIST OF FIGURES xv

LIST OF ABBREVIATIONS xxii

CHAPTERS

1 INTRODUCTION 1

2 THEORETICAL BACKGROUND 7

2.1 Surface Plasmon Polaritons 8

2.2 Localized Surface Plasmon Resonances 10

2.3 Nonlinear Plasmonics 11

2.3.1 Second Harmonic Generation 12

2.3.2 Surface Enhanced Raman Scattering (SERS) 14

2.4 Fano Resonance 15

2.4.1 Fano Resonance in Linear Response 17

2.4.2 Fano Resonance in Nonlinear Response 19

3 SILENT ENHANCEMENT OF SURFACE ENHANCED RAMAN SCATTERING 21

3.1 The Setup 22

3.2 Analytical Approach 26

3.2.1 Hamiltonian and Equations of Motion 26

3.2.2 Hamiltonian from Optomechanical Model 29

3.2.3 Enhancement 31

3.2.4 Suppression 32

3.3 3 Dimensional Simulations 33

3.4 Coupling to a Long-live Dark Plasmon Mode: Analytical Approach . 40

3.5 Comments on Possible Implementations 42

4 FANO CONTROL OF NONCLASSICALITY 47

4.1 Introduction 47

4.2 Theoretical Model 49

4.3 Nonclassicality Measure and Quantifying the Entanglement 52

4.3.1 Logarithmic Negativity 53

4.3.2 Simon-Peres-Horodecki Criterion 54

4.4 Beam Splitter Transformations 54

4.5 Nonclassicality Analysis of a Plasmonic Second Harmonic Conversion 58

4.5.1 Plasmonic Mode Fluctuations in the Steady-State Limit 58

4.5.2 Expectation Values of Input Plasmonic Mode Fluctuations . . 61

4.6 Results 63

5 CONCLUSION AND REMARKS 73

REFERENCES 77

CURRICULUM VITAE 89

LIST OF FIGURES

FIGURES

Figure 2.1 Schematic representation of (a) surface plasmon polariton (SPP) oscillations and (b) localized surface plasmon resonance (LSPR). (a) SPP oscillations travel along the metal surface in x and y-directions while they attenuate in z-direction through the dielectric. (b) LSPR, on the other hand, is the collective oscillations of free electrons in the vicinity of positively charged ions, resulting in the strong enhancement in the polarization of the metal surface. 9

Figure 2.2 Representation of nonlinear processes, (a) second harmonic generation (SHG) and (b) Stokes Raman scattering. (a) In SHG, two incident plasmonic oscillations with frequency ω combines to result in a single plasmonic mode with double the energy, 2ω. (b) Stokes Raman scattering occurs when the incident photons scatter inelastically and yield to the Raman signal that provides information about the vibrational modes of the system. 13

Figure 2.3 The Fano dip occurs when an auxiliary particle with sharp dielectric function is placed in the vicinity of the hot spot of a gold MNP. The 3D solutions of Maxwell equations are performed by using the experimental dielectric function for gold. 16

Figure 3.1 (a) The system is developed in order to analyze the enhancement in the SERS signal using 3D solutions of Maxwell equations. The hot spots are formed in the gap between two gold nanoparticles of radii 90 nm and 55 nm. A spherical Raman converter molecule of 4 nm radius (blue) is placed in the vicinity of the hot spots. An auxiliary QE which has a radius of 4 nm (purple) is placed at the hot spots of the dimer. The presence of QE introduces path interference effects which enhances the response of the $\hat{a}_{\mathrm{R}}$-mode. (b) Linear response of the gold dimer supports two plasmon oscillation modes at Λ=530 nm and Λ_{R}=780 nm. The system is excited by a λ=593 nm source and a Stokes-shifted signal emerges at λ_{R}=700 nm. The level spacing, λ_{eg} of the auxiliary QE is varied to determine the conditions in which the enhancement of the $\hat{a}_{\mathrm{R}}$-mode occurs. For 3D simulations, experimental data of gold is used for the MNP dimer and a sharp Lorentzian dielectric function is assigned to the auxiliary QE regarding the discrete states. 24

Figure 3.2 3D simulations of excited and Stokes-shifted plasmon mode hot spots. Electric field profiles of the (a) excited and (b) Raman converted modes given in Fig. 3.1 can be observed. It is shown that the hot spots of the two modes spatially overlap. (c) Mean electric field on the QE is displayed in terms of the position of the center of QE. The mean electric field is proportional to the overlap integral f, which denotes the interaction strength between MNS-QE. 25

Figure 3.3 Numerical time evolution results of the Raman enhancement factor with respect to the QE level spacing values, λ_{eg}. Here, this enhancement of SERS signal is due to the path interference effects and adds up to the enhancement due to the hot spot localization. Presence of the QE, with level spacing $\lambda_{eg} = c/\omega_{eg}$ creates a growth in the SERS response according to Eq. (3.16). It can be observed that as the interaction strength decreases, the QE level spacing values shift to the shorter wavelengths to generate maximum enhancement. 32

Figure 3.4 The effect of using a poor quality QE in terms of its damping rate on the Raman enhancement factors. The damping rate of the QE is increased to resemble the decay rate of the plasmon oscillation modes, $\gamma_{eg} = 10^{-2}\omega$. Even with this value of the damping rate, there still occurs an enhancement factor around ~ 100. 33

Figure 3.5 Suppression of the SERS signal due to path interference effects. From analytical point of view, presence of an auxiliary QE with a level spacing in resonance with the $\hat{a}_{\mathrm{R}}$-mode as $\omega_{\mathrm{R}} = \omega_{eg} = c/\lambda_{eg}$, yields a cancellation in the denominator of the SERS response in Eq. (3.16). . . 34

Figure 3.6 Different values of Raman enhancement factors for different sizes of Raman reporter molecule. All the sizes of Raman reporter molecule is simulated according to different spatial positions of auxiliary QE, (a) z=0.0 nm, (b) z=0.53 nm, (c) z=0.55 nm, (d) z=0.57 nm. It is observed that the size of the reporter does not alter the order of magnitude of the generated enhancement values. 35

Figure 3.7 The sharp Lorentzian dielectric function, $\epsilon(\omega)$ that represents the auxiliary QE in 3D simulations. A sharp Lorentzian function in the form of $\epsilon = 1 + 2\omega_p^2/(\omega_{eg}^2 - \omega^2 - i2\gamma_{eg}\omega)$ is used in order to generate an object with discrete energy levels. 37

Figure 3.8 The additional enhancement of SERS via path interference which is obtained by using the exact solutions of 3D Maxwell equations. When the QE is introduced to the system, the localization of the fields on the Raman converter remains unchanged, however, the SERS signal is increased around 10^3-10^4 factors. This amount of increment multiplies with the enhancement that is already present in the system as a result of the localization. The additional enhancement occurs as predicted by the analytical model in Section 3.2.3 and shifts to longer wavelengths as the MNS-QE coupling increases. In the simulations, moving QE closer to the center of the dimer (z=0) implies that the interaction between QE and the hot spots are getting stronger, until the system reaches to a region where it enters to a strong coupling regime. 38

Figure 3.9 The results of 3D simulations for the maximum enhancement factors with respect to the (a) slightly different level spacing values and (b) slightly different positions of the QE. (a) When the QE is brought closer to the center of the dimer, the enhancement factor starts to decrease as the system moves into the strong coupling regime. The simple treatment that is presented here cannot model the excitations in the strong coupling regime. For practical reasons, it is not realistic to expect that a bunch of molecules could have the exact same level spacing values, as well as could be placed to certain positions without any errors. Instead, a bundle of molecules with similar level spacing values can be placed to a close vicinity near the desired point. This figure shows what might be the possible enhancement achievement according to realistic expectations. 40

Figure 3.10 The analytical Stokes-shifted enhancement results of dark-mode coupling to the MNS. The similar positioning of maximum enhancement with respect to $\lambda_{\text{dark mode}}$ is observed compared to Fig. 3.8. 42

Figure 3.11 The suppression of the Stokes-shifted Raman signal in the case of DM coupling to the λ_{R}-mode of the MNS. At the resonance condition where $\lambda_{\text{DM}} = \lambda_{\text{R}}$ = 700 nm, the suppression takes place for several orders of magnitude. 43

Figure 3.12 The setup of an AFM tip utilized with a Raman reporter molecule. The simple analytical model proposes that when the AFM tip is contaminated with appropriate auxiliary molecules, the path interference effects will be introduced and an enhanced TERS signal will be produced without increasing near-field intensity. 44

Figure 4.1 The schematic representation of the beam splitter operation. The input states are $|\psi_a\rangle$ and vacuum $|0\rangle$, composing the initial state as $|\psi_a\rangle_1 \otimes |0\rangle_2$. The two-mode output state after the transformation is $|\psi_{12}\rangle = f\left(\mu_1 \hat{a}_1^\dagger + \mu_2 \hat{a}_2^\dagger\right)|0\rangle_1 \otimes |0\rangle_2$. 56

Figure 4.2 (a) The enhancement factor of the SH converted photons with respect to the different level spacing values of the QE. Corresponding (b) nonclassicality measure $\mathcal{N}_{\mathrm{SMNc}}$ and (c) nonclassicality witness η_{SMNc} are presented. Here, all the parameters are given in proportion with the incident light that stimulates $\hat{a}$-mode of the plasmonic structure with the frequency ω. The MNS supports the SH mode at $\Omega_2 = 1.9\omega$ and the second order susceptibility is taken as $\chi^{(2)} = 10^{-3}\omega$. The interaction strength between the MNS-QE is taken as $f = 0.1\omega$. The strength of the source that drives the $\hat{a}$-mode is $\varepsilon_{\mathrm{s}} = 10^{-2}\omega$. The pumping strength for the source that drives the QE is also determined as $\varepsilon_{\mathrm{p}} = 10^{-2}\omega$. It can be observed that at the region where SH converted photons reach their maximum enhancement around $\Omega_2 = 1.9\omega$, both of the nonclassicality measure and witness reveal the same form of increment. This indicates that the presented enhancement around 10^3 factors occurs as a result of the nonlinear path interference phenomenon. 65

Figure 4.3 (a) The amount of enhancement in the SH converted plasmon mode is presented. The pumping strength of the QE is decreased 3 orders of magnitude compared to Fig. (4.2), becoming $\varepsilon_{\mathrm{p}} = 10^{-5}\omega$. The other parameters are kept the same as; $\Omega_2 = 1.9\omega$, $\chi^{(2)} = 10^{-3}\omega$, $\varepsilon_{\mathrm{s}} = 10^{-2}\omega$ and $f = 0.05\omega$. (b) The nonclassicality measure $\mathcal{N}_{\mathrm{SMNc}}$ and (c) nonclassicality witness η_{SMNc} increase in the same trend with the SH converted plasmon mode, implying that the enhancement phenomenon accommodate nonlinear effects. With decreasing the QE pump strength, the maximum enhancement factor decreased to $\sim 10^2$. 67

Figure 4.4 (a) The SH enhancement factor is presented along with the (b) nonclassicality measure $\mathcal{N}_{\mathrm{SMNc}}$ and (c) SPH nonclassicality witness η_{SMNc}. The interaction strength between MNS-QE, $f = 0.05\omega$ is reduced to half compared to that of Figs. (4.2) and (4.3). All other parameters are unchanged as follows; $\Omega_2 = 1.9\omega$, $\chi^{(2)} = 10^{-3}\omega$ and $\varepsilon_{\mathrm{s}} = 10^{-2}\omega$. Similar to previous figures, (b) the nonclassicality measure $\mathcal{N}_{\mathrm{SMNc}}$ and (c) nonclassicality witness η_{SMNc} also increase with increasing SH response. This implies the presence of path interference effects in the enhancement process. Comparing to the case where the interaction strength is higher as $f = 0.1\omega$, the maximum enhancement value is decreased an order of magnitude when the interaction is reduced. 68

Figure 4.5 (a) The results of enhancement in the SH signal where the QE pump strength is $\varepsilon_{\mathrm{s}} = 10^{-4}\omega$ and the interaction strength is $f = 0.05\omega$. (b), (c) The nonclassicality measurement and witness denote that path interference effects take place. Since both the interaction strength and the QE pump strength is taken relatively very small, the maximum enhancement factor is around 25, however this implies that even when the interaction is very small, the SH signal can be altered due to the presence of Fano resonance. 69

Figure 4.6 (a) The SH converted field enhancement with respect to the QE pump strength value. As the pump strength is increased, the enhancement factor also increases. The parameters are taken the same as Figs. (4.2) and (4.3). (b)-(c) The corresponding nonclassicality measure and witness indicate the presence of nonlinear processes. At the values greater than $\varepsilon_{\mathrm{p}} = 0.01\omega$, the system do not reach a steady-state. . 70

Figure 4.7 (a) The enhancement results with respect to the QE pump strength are presented with reduced interaction value of $f = 0.05\omega$. Since the MNS-QE interaction is small compared to Fig. (4.6), the maximum enhancement factor is also reduced. However, by observing nonclassicality measure and witness in (b) and (c), it can be acknowledged that although it is mostly reduced, the SH response can still be manipulated as a result of path interference. 71

LIST OF ABBREVIATIONS

EM	Electromagnetic
SP	Surface plasmon
nm	Nanometer
QE	Quantum emitter
MNS	Metal nanostructure
SERS	Surface enhanced Raman scattering
SH	Second harmonic
3D	3 Dimensional
MNPBEM	Metal nanoparticle boundary element method
MNP	Metal nanoparticle
SPP	Surface plasmon polariton
LSPR	Localized surface plasmon resonance
SHG	Second harmonic generation
Hz	Hertz
DM	Dark-mode
AFM	Atomic force microscope
DNA	Deoxyribonucleic acid
TERS	Tip enhanced Raman scattering
SPH	Simon-Peres-Horodecki
SMNc	Single mode nonclassicality

CHAPTER 1

INTRODUCTION

Light carries information in such a way that it makes communication and data transfer possible around the globe. This leads the researchers to be highly interested in photonic devices, which can replace the electronic components in microprocessors and computer chips, someday not very far from our time. However, there is a constraint on the performance of photonic devices, named as the diffraction limit, the optical phenomenon that restricts the resolution of a system stating that the width of an optical fiber carrying the electromagnetic (EM) wave must be at least the half of the field's wavelength [1, 2]. Nevertheless, there are some structures that can provide ways to exceed the diffraction limit, asserting techniques to direct light at the interface between the metal and a dielectric.

In an assembly of such a structure where a metal interfacing a dielectric, surface plasmons (SPs) are generated when the collective oscillations of electrons at the surface of the metal matches with the wavelength of the external EM-field. This makes the EM-field to be confined to a region below the diffraction limit [3]. In the year of 2000, this new emerging field has given the name of "plasmonics" at CalTech, USA [1]. Since then, studies showed that there is an increasing range of applications of plasmonics, including light concentration, nanophotonic lasers, biochemical sensing and nanoantennas [3–5]. Nanoplasmonics is the branch of this wide area devoted to nanoscale optical phenomena in nanostructured metal systems. The ability of a metal system to generate surface plasmons depends on the material's dielectric function to have a negative real part [6].

When metal nanoparticles (MNPs) interact with light, the nm-sized localized optical fields, which are called as the hot spots, are generated at the metallic surface where

the incident EM-field is confined as a result of induced surface plasmons [7]. At these regions the field intensity can be enhanced up to 10^5 factors depending on the details of the nanostructure [8]. This strongly enhanced EM-field allows weak nonlinear processes to be significantly increased, underlying the fact that nonlinear responses depend on the higher order powers of the induced EM-field polarization [7, 9].

Coupling a discrete state object of small decay rate, such as a quantum emitter (QE) to a continuum, such as a MNS, can yield to a destructive interference resulting in an asymmetric dip in the otherwise Lorentzian-shaped plasmonic spectrum. This phenomenon, known as the Fano resonance [10] can be used to take control over nonlinear processes and provide further enhancement of the localized hot spot field [11] as well as extending the lifetime of plasmonic excitations [12]. Furthermore, it has been demonstrated that a double-resonance scheme has significant advantages over single-resonance structures considering the strength of the nonlinear process [13–15].

Surface Enhanced Raman Scattering (SERS) is one of the nonlinear responses that a MNS-dielectric assembly can possess. It is a powerful and unique tool that allows the detection of the molecular structure. Fundamentally, SERS is a technique that significantly increases the weak signal of Raman scattering from a substance. Due to the large enhancement that it provides, SERS even allows the detection of single molecules, making itself an extraordinary technique for the characterization of a few molecules in the neighborhood of plasmonic structures [16–18].

Although the hot spot enhancement provides a useful approach to enhance the nonlinear processes in plasmonic structures, it is limited with various restrictions. Among the limitations, the modification of vibrational modes [19], the breakdown of the molecule [20] and the transition to the tunnelling regime [21] can be mentioned. In this study, a new channel of enhancement is introduced which utilizes the path interference phenomena in the SERS response of a coupled MNS-QE system. It is of importance to emphasize that as a result of the path inference phenomena, the enhancement factors can be multiplied by $10^2 - 10^3$ without an increase in the localized field intensities. In that sense, the extra enhancement appears to be "silent" in which the localized field on the Raman active molecule is not affected. Therefore the limitations on the hot spot enhancement can be overcome. The cause of this extra

enhancement is explained with the effects of Fano resonance which comes up when a discrete state object is coupled to the continuum distribution of plasmonic MNS. In other words, coupling of a discrete state such as a QE to a MNS reveals the path interference phenomena and can be utilized to either enhance and suppress the nonlinear response of the system.

Here, the question arises whether is it possible to further control the QE in order to manipulate the nonlinear response as desired. The second part of this thesis addresses this question by examining another significant feature of the Fano type coupling considering a similar MNS-QE structure to that of first part. Here, the SH response of the double-resonant MNS is studied. Driving the QE with a small pumping source enables the further control of nonlinear signal from the structure. Therefore, the nonlinear response is either enhanced or suppressed as a result of changing the strength of the QE pumping source. In such a setup, a double-resonant MNS is coupled to the QE in its higher energy mode, while the lower energy plasmon mode is driven with a source. It is suggested that driving the QE with a source enables the modification of the SH response. While controlling the SH signal, it is also desired to acknowledge that if the emerged SH signal is a result of the path interference effects or due to the energy transferred to the system by the QE pump source. The possible method to investigate the origin of the enhancement is to analyze the entanglement features of the emerging SH signal.

The subject of entanglement is now at the heart of quantum physics and information processing, albeit once it was a controversial phenomenon which is thought to indicate the incompleteness of the quantum theory. When it is first described in 1935 by Einstein, Podolsky and Rosen as a "spooky action at a distance", it was unthinkable that the entanglement properties of quantum states could actually be measured by controlled experiments. However before even a century has passed, it is now possible to think of the entanglement as a resource for various quantum applications, such as quantum cryptography, information, teleportation or measurement based quantum computation [22, 23]. To describe in its simplest form, quantum entanglement occurs when two or more particles have quantum states that cannot be identified independently from each other, even when the spatial distance between particles are extremely large. The entanglement feature cannot be observed in classical mechan-

ics, it is a specific feature of quantum physics. Hence, quantum correlations make the tasks possible which are either impossible or inefficient when the classical systems are considered [23].

As a result of its importance in quantum world, it becomes an important task to detect and quantify the entanglement features in a quantum system. Furthermore, the entanglement can be likened to energy where they both can be consumed and converted into different forms once they are generated [24]. One of the approaches that are best known to generate entangled states are the beam splitter-like operations. A necessarily nonclassical single-mode state at the input have the ability to generate two-mode entangled states at the beam splitter output [25–28]. In Ref. [28], it is demonstrated that at such a beam splitter setup, the degree of the nonclassicality is related with the ability of the single-mode field to produce two-mode entanglement at the output. Furthermore, it can also be shown that the rank of entanglement is equal to the rank of the expansion of the nonclassical state in terms of classical coherent states [29].

In this work, the effect of Fano resonance for double-resonant plasmonic structures coupled with a discrete energy object is investigated. In Chapter 2, a theoretical background for plasmonics, linear and nonlinear Fano resonance, and overlap integrals for nonlinear conversions are presented. In Chapter 3, one of the nonlinear responses, the surface enhanced Raman scattering (SERS) is examined for a double-resonant MNS coupled with a QE. The analytical solutions of the coupled system is provided where the second quantized SERS Hamiltonian is utilized in order to obtain the time evolved expressions for the plasmonic and discrete states. With this analytical approach, the enhancement and suppression of the SERS signal is demonstrated. It should also be noted that with the SERS mechanism, the Raman signal is already enhanced up to 10^8 factors as a result of the incident field localization at the MNS hot spots. The presented enhancement here do not replace these effects of localization, on the contrary they add up on top the hot spot enhancement that is already present. The hot spot enhancement is restricted with several limitations, such as the modification of the vibrational modes, the breakdown of the molecule or transition to the tunneling regime. The approach that is presented here aims to provide an insight on how the path interference effects lead to the enhancement of nonlinear response without altering the hot spot fields and modifying the Raman modes. It is also beneficial to show that the non-

linear response of a plasmonic system can also be modified by using the coupling of a longer lifetime object, such as the plasmonic dark mode. Therefore, within the analytical approach the enhancement mechanism of the dark-mode coupling to the MNS is also presented. To continue, the numerical solutions of 3D Maxwell equations for the SERS enhancement are obtained by developing the Raman response module on the Metal Nanoparticle Boundary Element Method (MNPBEM) toolbox of Matlab. The two different approaches that are presented here, the analytical solutions and the 3D simulations demonstrate the similar behaviour for the enhancement of nonlinear response. As a result of the 3D simulations, an enhancement around 10^3 factors is added on top of the localized field enhancement, without increasing the hot spot strength. The effects of different parameters on the system, such as increasing the QE damping rate, the excitation strength and the Raman susceptibility are also examined.

In Chapter 4, a similar analytical model is described for SH conversion from a MNS-QE assembly. Congruently, the SH Hamiltonian of the system is presented and the steady-state solutions for the plasmonic and discrete modes are obtained. By driving the QE with a source, the effect of path interference among the states of the system is investigated. The nonclassicality measure is utilized in order to show that the emerging SH signal occurs to have entanglement features, which leads to the consequence that the obtained enhancement is a result of the Fano effect and not a direct energy transfer from the source that pumps the QE. For the MNS-QE assembly described above, the entanglement features of the second converted signal are examined by using the beam splitter approach, where the input ($\hat{a}_1$) and output ($\hat{a}_2$) states can be characterized as Gaussian states. After the covariance matrix is produced, the logarithmic negativity can be defined as an entanglement criteria $\mathcal{E}_{\mathrm{SMNc}}$ which eventually yields to the nonclassicality measure, $\mathcal{N}_{\mathrm{SMNc}}$ of the input ($\hat{a}_1$) state. Additionally, the entanglement criteria of Simon-Peres-Horodecki is also implemented to obtain another entanglement witness, η_{SMNc} which can also be used for non-Gaussian states. Utilizing the beam splitter approach provides a benefit as follows; the nonclassicality measure $\mathcal{N}_{\mathrm{SMNc}}$ only requires the knowledge of the fluctuations in the noise operators of the single state input mode. Therefore, by using $\langle \hat{a}_1^2 \rangle$ and $\langle \hat{a}_1^\dagger \hat{a}_1 \rangle$, it is demonstrated that the entanglement characteristics of the coupled MNS-QE assembly increase as the the second converted signal is enhanced. For certain values of the QE level-

spacing, the SH response of the system is enhanced accompanied by an increased amount of nonclassicality. In other words, for the enhanced SH response, the input mode appears to have increased nonclassicality. This result underlies the fact that the enhancement of the SH response of the MNS-QE assembly is due to the Fano type coupling and not a direct result of the energy provided by the source terms.

CHAPTER 2

THEORETICAL BACKGROUND

Surface plasmons are the collective oscillations of free electrons originating at the interface between a conductor and a dielectric, driven by incident electromagnetic radiation. Almost two decades ago, the science beneath the surface plasmons named as plasmonics. Ever since that time, plasmonics find a wide range of applications in practical science such as manipulating and guiding the light at nanoscale, single molecule detection and its biomedical applications, optical imaging below diffraction limit and enhanced optical transmission through subwavelength structures [30].

Although the academic studies are relatively young in nanoscience, the optical properties of metal nanoparticles have been instruments of art throughout history. The best known example, the Lycurgus cup dates back to 4th century A.D. from Byzantine empire. Two millennia later, the labor for surface plasmons begin as Robert W. Wood made an abrupt observation about optical reflection on metallic gratings. Fifty years later, David Pines described the energy losses of fast electrons as forms of collective oscillations, naming them as "plasmons". In the same year, Robert Fano introduced the term polariton for the coupled oscillations of bound electrons. Over and above, Ritchie and coworkers implemented surface plasmon resonances to describe the anomalous behaviour that occurred in Wood's observations. In 1970, Uwe, Kreibig and Zacharias described the optical properties of the metal nanoparticles in terms of surface plasmons for the first time. Hence, the discovery of surface enhanced Raman scattering (SERS) the same year made a major contribution to the field of nano-optics. Ever since, all these major contributions in plasmonics led the growth of the field not only as a branch of physics but in biology and chemistry as well [30].

2.1 Surface Plasmon Polaritons

Considering the interaction of light with a volume plasmon, the energy and momentum cannot be conserved simultaneously, so some coupling mechanism must be introduced in geometrical form. However at an interface, the energy momentum relation of the plasmon can be matched to that of light in the form of collective free electron oscillations, describing a surface plasmon (SP). This so called surface plasmons can be excited by prism coupling, grating coupling or with any nanostructure that produces subwavelength corrugation [31]. An incident light with a wave vector nearly parallel to the interface generates stronger coupling as the excitation of surface plasmons occur in accordance with the oscillating electric field [31]. Materials that possess a negative real and small positive imaginary dielectric constant have the ability to produce surface plasmon resonances [32].

Surface plasmons take different forms according to the surroundings, along metal surfaces they freely propagate as electron density waves while on metal nanoparticles they become localized electron oscillations [30]. The two types of surface plasmons, propagating and localized resonances are shown in Fig. 2.1 [32]. While the propagating surface plasmons can travel along the metal-dielectric interface through x- and y- directions, localized surface plasmons are resonances around nanoparticles arising from the interaction of incident electromagnetic field with the metal nanoparticle (MNP) which is smaller in size than the incident wavelength [32].

Considering a classical semi-infinite system with two non-magnetic media with dielectric functions ϵ_1 and ϵ_2, separating by a planar interface at $z = 0$, the Maxwell's equations are written as [33]

$$\begin{aligned} \nabla \times \boldsymbol{H}_i &= \epsilon_i \frac{1}{c} \frac{\partial \boldsymbol{E}_i}{\partial t}, \\ \nabla \times \boldsymbol{E}_i &= -\frac{1}{c} \frac{\partial \boldsymbol{H}_i}{\partial t}, \\ \nabla \cdot (\epsilon_i \boldsymbol{E}_i) &= 0, \\ \nabla \cdot \boldsymbol{H}_i &= 0, \end{aligned} \tag{2.1}$$

where $i = 1$ at $z = 0$ and $i = 2$ at $z > 0$. Choosing the x-axis to be the propagation

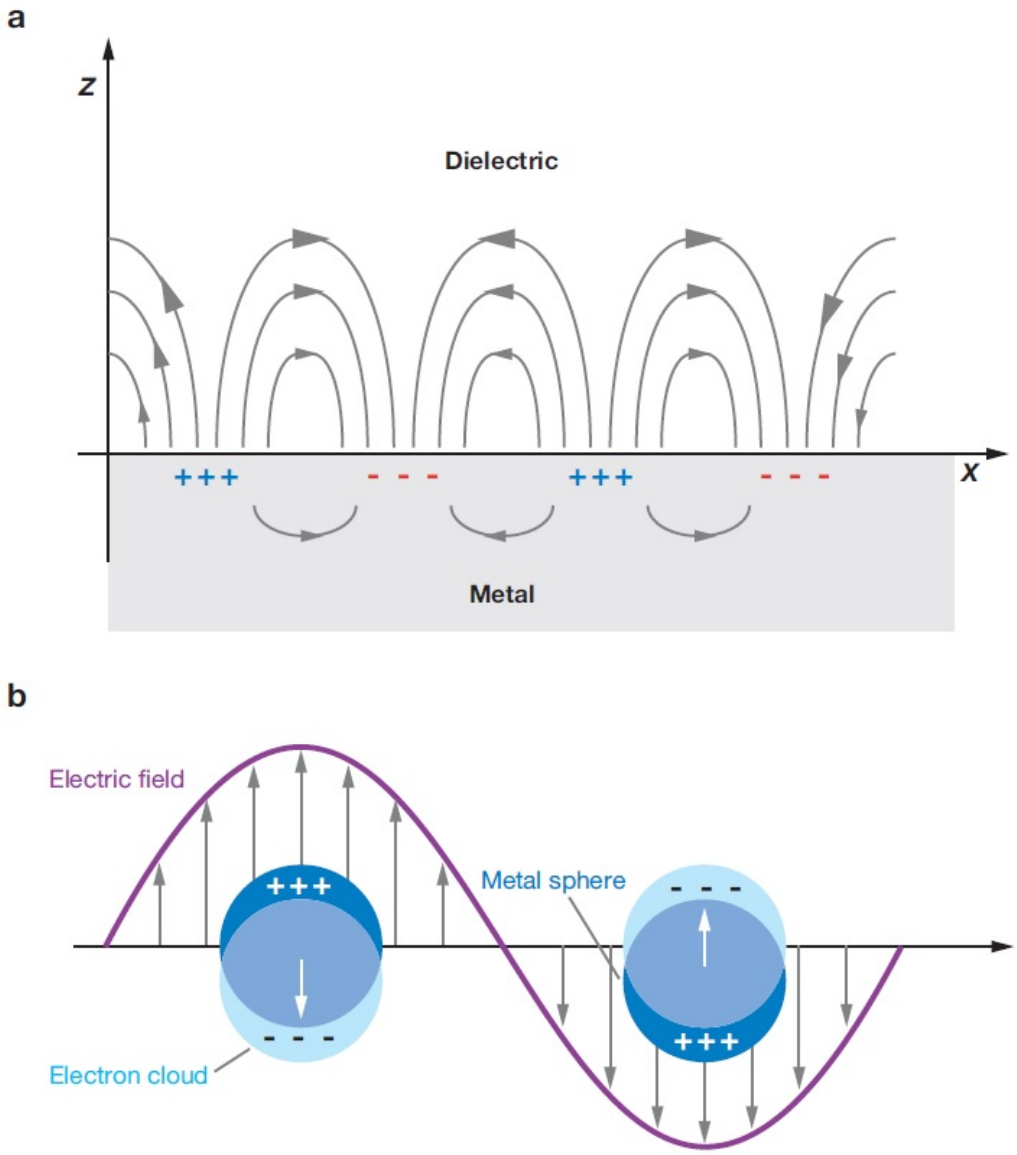

Figure 2.1: Schematic representation of (a) surface plasmon polariton (SPP) oscillations and (b) localized surface plasmon resonance (LSPR). (a) SPP oscillations travel along the metal surface in x and y-directions while they attenuate in z-direction through the dielectric. (b) LSPR, on the other hand, is the collective oscillations of free electrons in the vicinity of positively charged ions, resulting in the strong enhancement in the polarization of the metal surface.

direction, the surface plasmon condition occurs as

$$q(\omega) = \frac{\omega}{c}\sqrt{\frac{\epsilon_1\epsilon_2}{\epsilon_1+\epsilon_2}}. \tag{2.2}$$

This frequency dependent equation for wave vector expresses the surface-plasmon condition where ϵ_1 and ϵ_2 are permittivity values of metal and dielectric and ω/c determines the magnitude of the incident field. Hence, the energy dispersion relation for the surface plasmon polariton becomes

$$\omega^2(q) = \frac{\omega_p^2}{2} + c^2q^2 - \sqrt{\frac{\omega_p^4}{4} + c^4q^4}, \tag{2.3}$$

with ω_p being the corresponding plasma frequency [33].

2.2 Localized Surface Plasmon Resonances

As the size of a MNP is comparable to that of the incident wavelength, free electrons of the nanoparticle participate in the collective oscillations. Exciting a MNP by an EM field at frequencies in which the polarizability of the metal would be strongly enhanced, generates localized surface plasmon resonances (LSPRs). As a result of the light confinement in nanoscale, the local EM fields are strongly enhanced [3, 6, 33]. The so called "hot-spots" are created where the oscillations are greatest at the surface and gradually decrease with distance. The field enhancement associated with surface plasmon resonance is characterized by the local field factor $L(\omega, \vec{r}) = |E_{loc}(\omega, \vec{r})/E_0(\omega)|$, where $\vec{r}$ is the position vector, $E_0(\omega)$ is the incident and E_{loc} is the intense localized fields [7].

The properties of the absorption bands, such as the resonance frequency and intensity depend on the composition, size, shape and spatial distribution in case of multiple MNPs, as well as the environment [31, 34]. Common materials that exhibit LSPR features are noble metals such as Au and Ag [35]. Furthermore, even the slightest variations in the local refractive index can be detected by using MNPs as a result of the intensely localized electromagnetic field, making the LSPR studies a good origin for sensing applications [31].

When the radius to incident wavelength ratio of a MNP is small enough (i.e. $R/\lambda < 0.1$), conduction electrons begin to oscillate coherently, leading to the building up

of polarization charges on the surface. Considering only the dipole oscillations, the extinction cross section σ_{ext}, can be obtained using the Mie approach to Maxwell's equations [35],

$$\sigma_{\text{ext}} = \frac{24\pi^2 R^3 \epsilon_m^{3/2} N}{\lambda ln(10)} \frac{\epsilon_i}{(\epsilon_r + \chi\epsilon_m)^2 + \epsilon_i^2} \tag{2.4}$$

where ϵ_m is the dielectric constant for the environment, ϵ_r and ϵ_i are real and imaginary dielectric parts of the metal dielectric function, R is the radius of the MNP and N is the electron density. χ appears as a constant that depends on the shape of the particle, obtained as 2 for a spherical distribution [31, 35]. In case of a metal nanostructure, the polarizability is described as the distortion of the electron cloud as a result of the interaction with an incident electric field. The given equation,

$$\alpha(\lambda) = 4\pi\epsilon_m(\lambda) R^3 \frac{\epsilon(\lambda) - \epsilon_m(\lambda)}{\epsilon(\lambda) + 2\epsilon_m(\lambda)} \tag{2.5}$$

defines the poarizability exhibiting a dipolar resonance as the denominator vanishes at $\epsilon_r = -2\epsilon_m$, indicating the relation between the LSPR extinction peak with the dielectric environment. The real part of the dielectric function, ϵ_r, can be explained by using the Drude model as

$$\epsilon_r = 1 - \frac{\omega_p^2}{\omega^2 + \gamma^2} \tag{2.6}$$

with ω_p is the plasma frequency and γ is the damping rate of the bulk metal. The imaginary part of the dielectric function is also significant as it is related to the broadening of the resonance peak, in other words, damping. By using Eq.(2.6) and the dipole condition $\epsilon_r = -2\epsilon_m$, the peak LSPR frequency at the resonance condition can be found as

$$\omega_{\text{LSPR}} = \sqrt{\frac{\omega_p^2}{1 + 2\epsilon_m} - \gamma^2}. \tag{2.7}$$

For visible and near-infrared frequencies where $\gamma << \omega_p$, the LSPR peak wavelength exhibits an approximately linear dependency on the refractive index at optical properties [36].

2.3 Nonlinear Plasmonics

The electromagnetic properties that accompany the surface plasmons uncover opportunities for light confinement at nanoscale. This confined light produce strong EM

fields resulting in the significant enhancement of weak nonlinear processes. This nonlinear effects have important outcome in photonic applications such as generation of ultrashort pulses, all-optical signal processing and ultrafast switching [7].

As they result from photon-photon interactions, optical nonlinearities are inherently weak, albeit can be enhanced through plasmonic effects. A nonlinear effect arises when the sinusoidal wave-from of the incident electric field is lost through a nonlinear material and experiencing a harmonic distortion, obeying the law of conversation of energy.

The optical response of this kind of a nonlinear material under the illumination of an incident field can be written in terms of the Taylor expansion of the electric field, defined as the polarization;

$$P = \epsilon_0[\chi^{(1)}E + \chi^{(2)}E^2 + \chi^{(3)}E^3 + ...] \tag{2.8}$$

where ϵ_0 is the vacuum permittivity, and $\chi^{(n)}$ is the nth order susceptibility of the material. The first term in this equation denotes the linear response for an optically linear medium [7].

2.3.1 Second Harmonic Generation

One of the nonlinear effects that is described above is the second harmonic generation (SHG). This process is described in Fig. 2.2 (a), where two photons from the incident beam with frequency ω is annihilated to create a single photon with a second harmonic frequency, 2ω. As a result of the interaction between the electric field and the nonlinear medium, the nonlinear polarization reveals itself in the second and higher order terms of Eq. (2.8). The second order susceptibility, $\chi^{(2)}$, harbours the generally complex structured information on electric and symmetry properties of the nonlinear material. In the second quantized framework, the second harmonic Hamiltonian can be obtained as follows;

$$\hat{H}_{SH} = \left(\int d^3\boldsymbol{r} E_2^*(\boldsymbol{r}) E_1^2(\boldsymbol{r}) \chi_2(\boldsymbol{r}) \right) \hat{a}_2^\dagger \hat{a}_1 \hat{a}_1 + H.c. \tag{2.9}$$

The term in the parenthesis determines the overlap integral, $\hbar\chi^{(2)}(\boldsymbol{r})$ where $\chi^{(2)}(\boldsymbol{r})$ is a step function that is constant over MNP and zero elsewhere. From the overlap

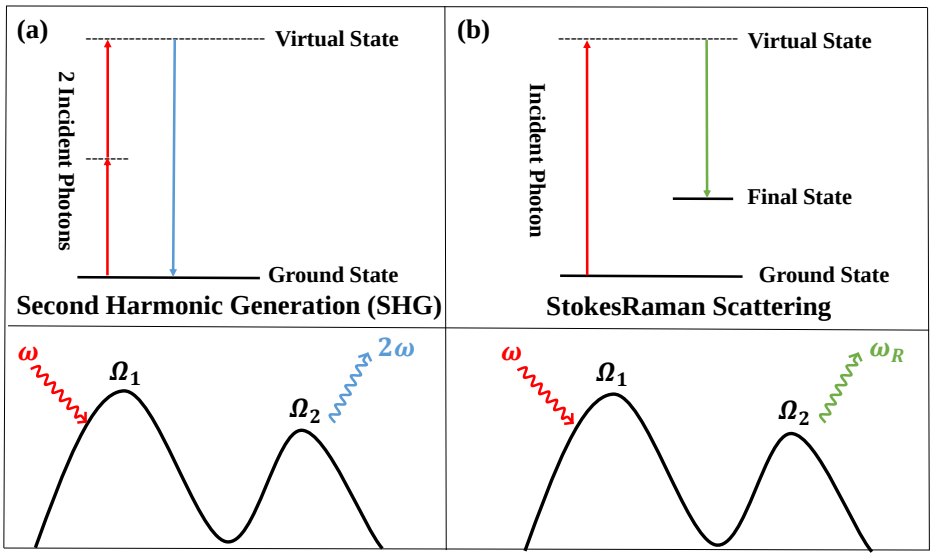

Figure 2.2: Representation of nonlinear processes, (a) second harmonic generation (SHG) and (b) Stokes Raman scattering. (a) In SHG, two incident plasmonic oscillations with frequency ω combines to result in a single plasmonic mode with double the energy, 2ω. (b) Stokes Raman scattering occurs when the incident photons scatter inelastically and yield to the Raman signal that provides information about the vibrational modes of the system.

integral it can be observed that if $E_2(\boldsymbol{r})$ is an odd function, then the overlap integral vanishes for a centrosymmetric MNS since $E_1(\boldsymbol{r})$ is the dipole-like driving field. As a result, SH generated plasmon modes cannot be observed in the far field for centrosymmetric systems. Thus, the emission of SH signal is only allowed when the system lacks the centrosymmetry [11, 37], unless the inversion symmetry is broken at the surface of the material. For such a system, SHG can be used as a surface probe. The examples of metallic nanostructures that exhibit strong SHG emission are metallic tips [38], multiple resonant structures [39, 40], split ring resonators [41], and metamaterials [42, 43].

2.3.2 Surface Enhanced Raman Scattering (SERS)

Surface enhanced Raman Scattering (SERS) is another nonlinear process which appears as a powerful observational tool that gathers growing interest in many areas of science since it's discovery in 1974 [44]. In its fundamental form, SERS is a technical method to enhance the inherently weak Raman scattered photons. Its uniqueness lies in the revelation of the chemical composition by determining the inner vibrational energy modes of the molecules that are subject to incident EM field, Fig. 2.2 (b). As a result, Raman spectroscopy enables scientists to use it in many ways to gather information about the structure of the materials [16].

The major drawback of using the spontaneous Raman scattering for material characterization is the weakness of the process. It is not a simple task to separate the inelastically scattered Raman signal from the intense Rayleigh scattered photons. At a rough estimation, only one in 10^8 photons undergo spontaneous Raman scattering [45]. With the following implementation, however, this hassle can be defeated. When a metal surface is roughened by adsorbing molecules in nanometer scale, this process significantly alters the electromagnetic modes of the material, as well as the lifetime and the emission intensity of the excited states of the adsorbed molecule. SERS is only one of the effects of this adsorbing and roughening process. Eventually, the enhancement of the weak Raman signal can be up to 10^6 factors [46].

The SERS enhancement factor depends on various mechanisms in which most of them are not fully understood yet. When the SERS mechanism was first interpreted, the initial understanding was to relate the observed enhancement to the number of molecules that is adsorbed to the metal surface. Later on it is observed that, although it is still not a complete approach, the enhancement is proportional to the increase in the cross-sectional area of the molecules [47].

Two major mechanisms that contribute to SERS are the electromagnetic and chemical enhancements. The details of the electromagnetic enhancement can mostly be studied through the electrostatic properties of a polarizable metal sphere under a uniform incident radiation. However, experimental studies show that this approach cannot be the only mechanism contributing to SERS, evidence propose that there occurs also

chemical enhancement which operates independently. To a first approximation, the electromagnetic enhancement factor (EF) is associated with the fourth power of the ratio of the electric field at a given position of the molecule ($\boldsymbol{r}_m$), to the incident field $E_{inc}(\omega)$ as [46, 48];

$$EF(\boldsymbol{r}_m, \omega) = \left| \frac{E(\boldsymbol{r}_m, \omega)}{E_{inc}(\omega)} \right|^4 . \tag{2.10}$$

Single molecule detection via SERS with high sensitivity is of great interest in many fields such as chemistry [17], nanobiology [49, 50], tumor targeting and cancer applications [51]. In a double-resonant structure, as a result of very intense electromagnetic fields at the nm-sized hot spots, the surface configuration and mapping of the inner structure of a single molecule is achieved.

Considering a plasmonic point of view, the enhanced electromagnetic fields by localized surface plasmon resonances interact with the vibrational modes of the molecule. In a Stokes-shifted process, a plasmon with frequency ω is absorbed to excite a vibrational mode with frequency ν and generate another plasmon with lower energy, ω_R. The corresponding Hamiltonian can be written similar to that of SHG in Eq. (2.9), as;

$$\hat{H}_R = \left(\int d^3(\boldsymbol{r}) \rho(\boldsymbol{r}) E_1^*(\boldsymbol{r}) E_2(\boldsymbol{r}) \right) \hat{b}^\dagger \hat{a^\dagger}_1 \hat{a}_2 + H.c. \tag{2.11}$$

where $\hat{b}^\dagger$ is the creation operator for the vibrational mode and $\rho(\boldsymbol{r})$ is the density of the molecule which can be considered as a 3D step function. The overlap integral term in the parenthesis defines the selection rules for the Raman process. It can be observed that as the overlap between the electromagnetic fields is greater, the obtained Raman intensity will be stronger [11].

2.4 Fano Resonance

For many years, the Lorentzian line shape is considered to be the fundamental and most common spectral dependence for many types of resonances both in classical and quantum systems. In 1935, it has been observed that the Rydberg spectral atomic lines exhibit an asymmetric profile. Introducing the first theoretical explanation the same year, Ugo Fano suggested a formula by utilizing the superposition principle from quantum mechanics [52, 53]. In 1961, he published a detailed, more elaborated

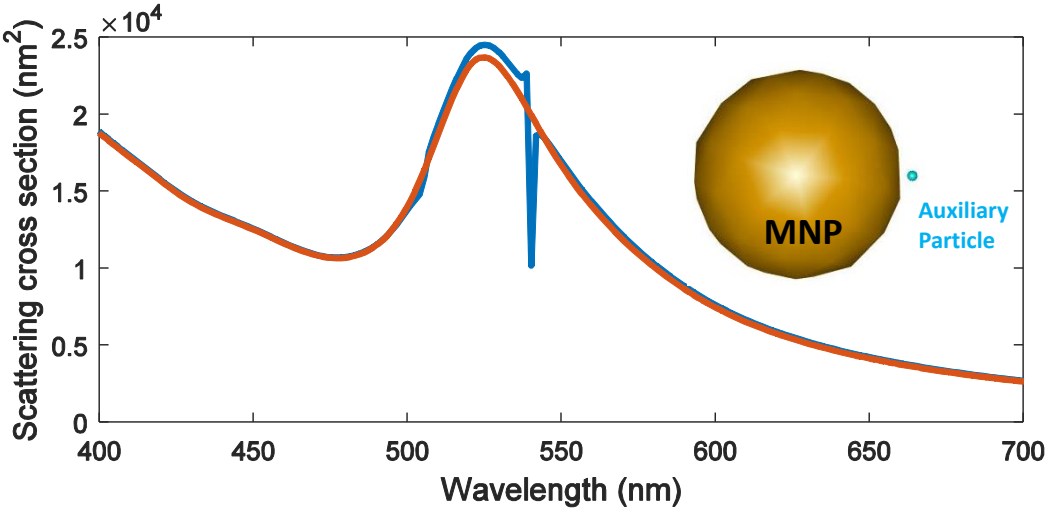

Figure 2.3: The Fano dip occurs when an auxiliary particle with sharp dielectric function is placed in the vicinity of the hot spot of a gold MNP. The 3D solutions of Maxwell equations are performed by using the experimental dielectric function for gold.

article on the subject [54], that later became one of the most important articles in physics of 20th century, explaining the phenomena in a system where the conversion paths interfere between a discrete state and a continuum [10,52]. The overlap between two pathways, one being a discrete excited state and the other being a continuum sharing the same energy level, creates destructive and constructive interference in the proximity of very close energy states, resulting in the asymmetric lineshape [55]. In Fig. 2.3, the Fano lineshape is observed when a sharp dielectric object is coupled to a gold MNP through its hot spot. This spectra is obtained by solving the 3D Maxwell equations in the Metal nanoparticle boundary element method (MNPBEM) toolbox of Matlab [56]. For the gold MNP, the experimental dielectric function for gold is used. Furthermore, the auxiliary particle is represented by a sharp Lorentzian profile, which corresponds to a structure with discrete energy levels.

Fano resonance provides a successful tool to explain a various number of phenomena in several quantum systems such as; quantum transport in quantum dots, wires and tunnel junctions, the absorption profile of some molecular structures and the asymmetric distribution of density of states in various optical systems. Although

fundamentally studied for quantum systems, Fano resonance also finds its counterpart in classical systems of coupled oscillators [52, 55, 57]. In its simplest form, the phenomenon can be studied through the example of two weakly coupled oscillators where one is under the influence of a periodic external force. Such a system would have two normal modes, first the oscillators swing back and forth together and second, they move in opposite directions. Driving one of the oscillators with an external force would reveal two resonance modes in the amplitude spectra of the forced oscillator. The first resonance with frequency ω_- is a symmetric profile with a Lorentzian shape, while the second resonance ω_+ is characterized with an asymmetric lineshape. The essence of Fano resonance is observed in the suppression that occurs in the ω_+ mode as a result of the destructive interference of the external force with the second oscillator.

2.4.1 Fano Resonance in Linear Response

Considering a plasmonic system, the Fano resonance can be studied through the path interference between a metallic nanostructure and a quantum emitter. Under an incident illumination, the excited state becomes weakly hybridized into two different states however their resolution still relies in the broadening of the excited state. These two hybridized paths are out of phase with each other as one absorbs the incident light while the other one emits. As a result, there occurs a transparency window in the absorption spectra of the plasmonic structure as the signal vanishes at the corresponding gap. This mechanism does not necessitate a driving field since the coupling between the plasmonic and the quantum objects is induced by the hot spot field of the MNS. As stated before, Fano resonance is not necessarily a quantum intervention as it reveals itself in the coupling of two plasmonic structures with one having a longer lifetime. One example for this effect is the split ring resonators [11]. Furthermore, Fano resonances may be utilized to increase the lifetime of the plasmonic oscillations, which can become significantly important as the enhanced lifetime results into the accumulation of the field strength at the hot spots [11].

Theoretical consideration of a system in which a MNS is coupled to a QE can provide an understanding of how path interference effects are interpreted. When the MNS

is illuminated with an excitation field of frequency ω, the corresponding plasmon mode would be excited. When placed properly close to the localized field, the dipole moment of the QE interacts strongly with the hot spot which is created in the near-field of the MNS. As the localized field is at least five orders of magnitude intense from the incident radiation, the coupling of QE to the incident field can safely be neglected. The Hamiltonian for such a system can be written as;

$$\hat{H} = \hbar\Omega\hat{a}^{\dagger}\hat{a} + \hbar\omega_{eg}\left|e\right\rangle\left\langle e\right| + \hbar(f\left|e\right\rangle\left\langle g\right|\hat{a} + H.c.) + \hbar(\hat{a}^{\dagger}\varepsilon_{p}e^{-i\omega t} + H.c.), \quad (2.12)$$

where $|e\rangle$ and $|g\rangle$ are the excited and ground states of the QE, respectively. Since the only quantity that matters is the energy difference between the ground and excited levels of the QE, the ground state energy can be assigned to zero. The term $\hat{a}^{\dagger}\hat{a}$ gives the number of excited plasmons in the system and f denotes the interaction strength between MNS-QE. The equations of motion can be derived through the Heisenberg relation $i\hbar\dot{a} = [\hat{a}, \hat{H}]$, where $\hat{a}$ is the annihilation operator for the plasmon mode and $\hat{\rho}_{i,j} = |i\rangle\langle j|$ is the density matrix operator of the QE, with $i, j = e, g$. By implementing these relations, the equations of motion becomes

$$\dot{\hat{a}} = (-i\Omega - \gamma)\hat{a} - if^{*}\hat{\rho}_{ge} + \varepsilon_{p}e^{-i\omega t}, \quad (2.13)$$

$$\dot{\hat{\rho}}_{ee} = -\gamma_{ee}\hat{\rho}_{ge} - if\hat{a}\hat{\rho}_{ge}^{\dagger} + if^{*}\hat{a}^{\dagger}\hat{\rho}_{ge}, \quad (2.14)$$

$$\dot{\hat{\rho}}_{ge} = (-i\omega_{eg} - \gamma_{eg})\hat{\rho}_{ge} + if^{*}\hat{a}(\hat{\rho}_{ee} - \hat{\rho}_{gg}). \quad (2.15)$$

Here, the decay rate of the plasmon mode ($\gamma \sim 10^{13} - 10^{14}$ Hz) and the damping rate of the quantum emitter ($\gamma_{eg} \sim 10^{9}$ Hz) is introduced.

Upon reaching the steady-state, both QE and the plasmon mode oscillates with the driving frequency $\sim e^{-i\omega t}$, where $\hat{\alpha} = \tilde{\alpha}e^{-i\omega t}$ and $\hat{\rho}_{ge} = \tilde{\rho}_{ge}e^{-i\omega t}$. Consequently, the plasmon mode amplitude in the steady-state can be denoted as

$$\tilde{\alpha} = \frac{\varepsilon_{p}}{[i(\Omega - \omega) + \gamma] - \frac{|f|^{2}y}{[i(\omega_{eg} - \omega) + \gamma_{eg}]}}. \quad (2.16)$$

Observing Eq. (2.16) leads to an understanding of how the response of the system changes as the level spacing of the QE is altered. When the interaction between MNS-QE is present, f is greater than zero. For simplicity, all quantities are denoted in proportion to the incident photon frequency, ω. For the condition where $\omega_{eg} = \omega$, the second term in the denominator becomes very large as the damping rate of the

emitter is very small compared to the photon frequencies. Hence, $\tilde{\alpha}$ becomes very small and a transparency is observed in the response of the system.

Among the suppression effect that takes place at the condition $\omega_{eg} = \omega$, there also occurs an enhancement if the proper conditions are met. If ω_{eg} is chosen such that the real parts of the two terms in the denominator are cancelled, the plasmon mode can be excited at the resonant position even if the incident radiation is off-resonant, $\omega \neq \Omega$ [11]. Another effect in such a coupled system is that the plasmon decay can be delayed by coupling a QE with a longer excitation lifetime [58].

2.4.2 Fano Resonance in Nonlinear Response

The efficiency of nonlinear responses in plasmonic systems is restricted by radiative losses, such as the optical scattering that an electromagnetic wave experience in the metal nanostructure, and nonradiative losses like heat generation. The total losses are associated with the width of the plasmon resonances in which a narrower response would mean a lower loss in total. Maintaining control over the width of the resonance is not straightforward as it is strongly related with controlling the localized field, however utilizing Fano resonances can introduce a way to manipulate the near-field and therefore, the width of the plasmon resonances [43].

The nonlinear processes can be enhanced via three different mechanisms in plasmonic systems, that add up as multiplication with each other. The first mechanism is described above as the localization of the incident EM field into hot spots, leading an increase in the local field up to 10^5 factors. This intense localized field yields to the enhancement of nonlinear effects as these are proportional with the higher orders of incident field polarizability. The second factor is the effect of Fano resonance in linear response, that adds up on top of the localized field enhancement. The third and final mechanism which contributes to the total enhancement is the path interference effect arising from the impact of Fano resonance in the nonlinear response [11]. Similar to the effects of Fano resonance in linear responses, the path interference effects suppress or enhance the response of nonlinear processes. In the following sections, the theoretical details for the path interference effects on SHG and SERS will be presented.

CHAPTER 3

SILENT ENHANCEMENT OF SURFACE ENHANCED RAMAN SCATTERING

For a plasmonic structure, the Fano mechanism occurs when the plasmon modes interact with a substance of sharp dielectric function, i.e., a discrete state, such as a quantum emitter (QE). The coupling of the QE with the MNS modifies the linear response as the localized hot spot field can be enhanced further. Therefore, the response of a Raman active molecule that is adsorbed to the MNS-QE coupled structure can be enhanced by placing it in the vicinity of the hot spots. As the field strength of the hot spots are increased, the nonlinear responses of plasmonic structure are also revealed as they are proportional to the higher order terms of the EM-field.

One of the nonlinear responses that a plasmonic structure can possess, Surface Enhanced Raman Scattering (SERS) is a very important technique that finds use in various aspects of science. The significance of SERS lies in the fact that it provides information about the chemical composition of a structure by determining the inner bonds. Furthermore, the mapping and surface configuration of a single molecule can be achieved by using a double-resonance plasmonic scheme [13]. The single molecule detection process requires very intense fields to be localized in the hot spots. Here, the imaging can be performed by placing the molecule in the close vicinity of an imaging tip, which makes the hot spot fields more and more intense as the two come closer. However, hot spot enhancement due to the localization is restricted with several limitations. For instance, as the intensity of the hot spot increases, the fragile molecules can be damaged by exceeding their threshold [20, 59]. Besides, it is experimentally demonstrated that the vibrational modes in a nanostructure can be modified due to the close proximity of the Raman-imaging tip [19]. Also, the field in-

tensity enhancement in the gaps can be restricted according to the electron tunneling regime [21].

The method that is presented in this chapter, aims to circumvent these limitations and provide an insight on how the path interference effects lead to the enhancement of nonlinear response [60]. It is shown that the SERS response of a double-resonant system can be modified without altering the hot spot intensities and modifying the Raman vibrational modes. A Raman reporter molecule is placed closely to the gap of a MNP dimer. Also in the hot spot of the dimer, an auxiliary QE (which can be a molecule or a nitrogen vacancy center) is positioned in order to utilize path interference effects. The "proof of principal" examination of the system shows that it is possible to enhance the SERS signal without affecting the electric field strength in the vicinity of the Raman active molecule. Additionally, the exact solutions of 3D Maxwell equations are performed to show that the SERS signal can be enhanced by a factor of 10^2-10^3, where the field intensities at the excited and the Stokes-shifted hot spots remain the same. The localization of the excited and the Stokes-shifted fields already provides enhancement in the Raman signal by an amount 10^8 factors in a plasmonic system [13]. The enhancement arising from path interference multiplies with this amount, making the total enhancement factor around 10^{10}-10^{11}. For systems that are already operate in the breakdown or tunneling regimes, the SERS imaging efficiency can be further increased by utilizing this phenomenon. For materials with small SERS imaging responses this gains vital importance. Additionally, the modifications in Raman vibrational modes can be avoided when using larger tip-surface spacing, or smaller incident laser strength, and hence, better signal intensities can be obtained.

3.1 The Setup

In this part, the system that is composed of a gold MNP dimer, an auxiliary QE and a Raman converter molecule is described in detail. In plasmonic systems, an efficient conversion occurs when the nonlinear process takes place between plasmonic excitations of different frequencies due to the localization [13, 61, 62]. Recently, it has been shown that structures that support plasmon resonances at both excitation

and Stokes frequencies (double-resonance) provide better enhancement factors for Raman intensities [13–15]. Therefore in this study, a double-resonance scheme is utilized which promotes two plasmon modes.

In Fig. 3.1 (a), the gold MNP dimer that supports the two plasmon modes can be observed. With their diameters of 90 nm and 55 nm, the two particles are separated with a gap of 4 nm. An x-polarized plane-wave propagating along the y-direction illuminates the dimer. The scattering cross section of the MNP dimer under this plane-wave illumination is given in In Fig. 3.1 (b). The two plasmon modes, $\hat{a}$ and $\hat{a}_{\mathrm{R}}$, can be observed with peak resonance values at $\Lambda = c/\Omega$ = 530 nm and $\Lambda_{\mathrm{R}} = c/\Omega_{\mathrm{R}}$ = 780 nm respectively.

Electric field distributions of the two hot spots corresponding to 530 and 780 nm are shown in Fig. 3.2 (a)-(b). The simulations are performed using the experimental, frequency dependent dielectric function for gold [56]. It is observed that the hot spots of the two modes spatially overlap. In Fig. 3.2 (c), the mean electric field is calculated at the spatial positions where the QE lies between z = 0-2 nm. The mean electric field gradually decreases as the spatial coordinates move away from the origin.

The plasmon-polaritons in the $\hat{a}$-mode are excited with the incident driving field at the wavelength $\lambda_{\mathrm{L}} = c/\omega$=593 nm. A Raman-active molecule with a diameter of 4 nm (blue) that interacts with the hot spots of the two modes $\hat{a}$ and $\hat{a}_{\mathrm{R}}$, [63] is placed in the close vicinity of the hot spots. The substantial overlap between the hot spots and the reporter molecule results in a significant overlap integral, χ, for the Stokes Raman process. When the $\hat{a}$-mode of the MNP dimer is activated with the incident field, the generated plasmons excite the Stokes-shifted plasmon mode, $\hat{a}_{\mathrm{R}}$ with $\lambda_R = c/_R$ = 780 nm [13–15]. Since the aim in this study is to provide basic understanding on the path interference effects, only a single vibrational mode at ν = 2600 cm^{-1} is considered for the Raman reporter molecule for the sake of simplicity.

An auxiliary QE with a diameter of 4 nm (purple) is introduced in the system as can be observed in Fig. 3.1 (a). The purpose of utilizing the QE in the system is to catalyze the nonlinear conversion by making use of its strong interaction with the hot spot of the $\hat{a}_{\mathrm{R}}$-mode. The level spacing of the QE, ω_{eg}, is taken to be off-resonant with both plasmon modes, which is chosen to be around $\lambda_{eg} = c/\omega_{eg} \sim$ 830 nm. The coupling

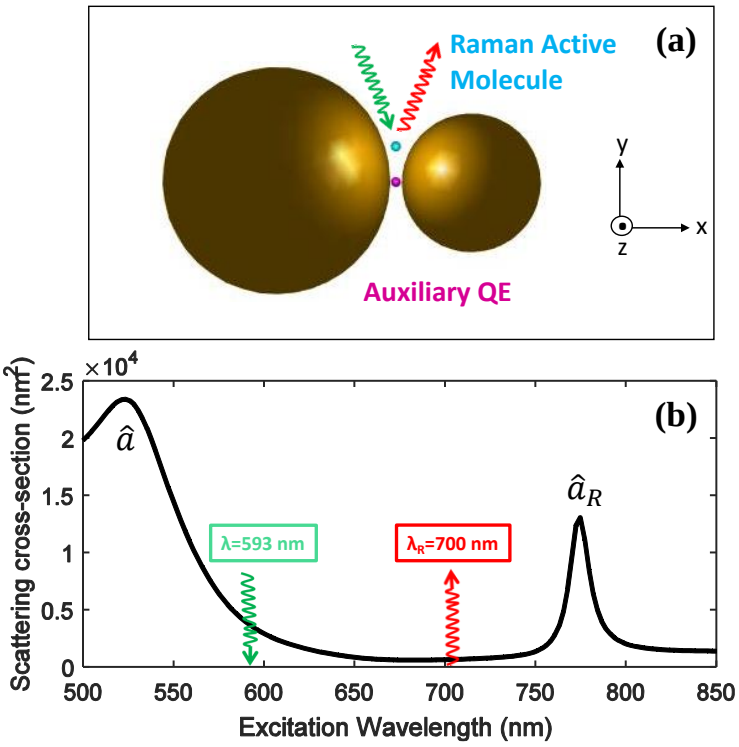

Figure 3.1: (a) The system is developed in order to analyze the enhancement in the SERS signal using 3D solutions of Maxwell equations. The hot spots are formed in the gap between two gold nanoparticles of radii 90 nm and 55 nm. A spherical Raman converter molecule of 4 nm radius (blue) is placed in the vicinity of the hot spots. An auxiliary QE which has a radius of 4 nm (purple) is placed at the hot spots of the dimer. The presence of QE introduces path interference effects which enhances the response of the $\hat{a}_{\mathrm{R}}$-mode. (b) Linear response of the gold dimer supports two plasmon oscillation modes at Λ=530 nm and Λ_{R}=780 nm. The system is excited by a λ=593 nm source and a Stokes-shifted signal emerges at λ_{R}=700 nm. The level spacing, λ_{eg} of the auxiliary QE is varied to determine the conditions in which the enhancement of the $\hat{a}_{\mathrm{R}}$-mode occurs. For 3D simulations, experimental data of gold is used for the MNP dimer and a sharp Lorentzian dielectric function is assigned to the auxiliary QE regarding the discrete states.

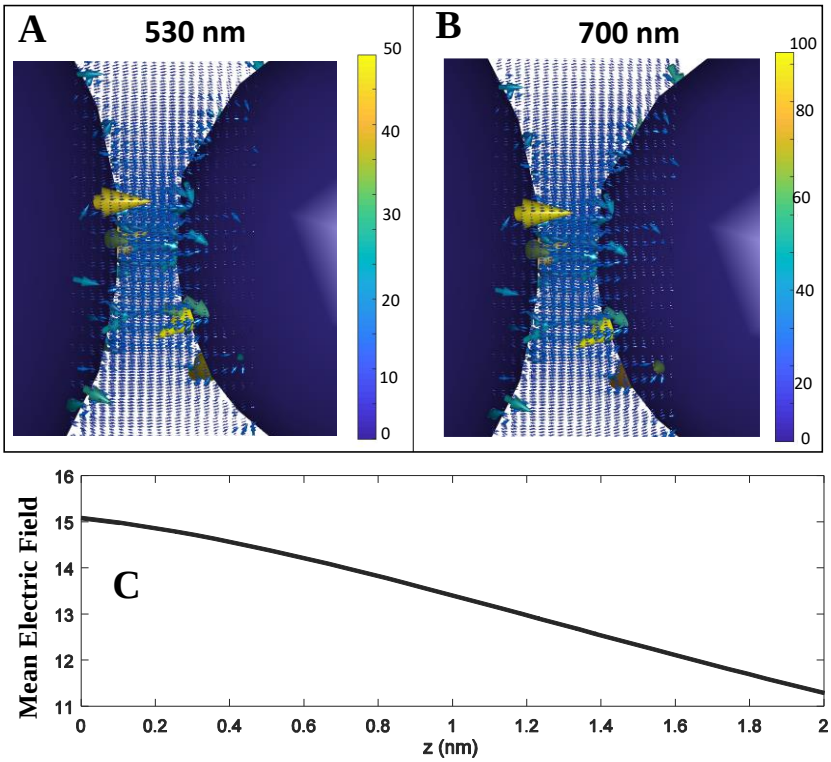

Figure 3.2: 3D simulations of excited and Stokes-shifted plasmon mode hot spots. Electric field profiles of the (a) excited and (b) Raman converted modes given in Fig. 3.1 can be observed. It is shown that the hot spots of the two modes spatially overlap. (c) Mean electric field on the QE is displayed in terms of the position of the center of QE. The mean electric field is proportional to the overlap integral f, which denotes the interaction strength between MNS-QE.

between the $\hat{a}_{\mathrm{R}}$-mode and the QE can be altered by moving the QE along the z-axis where the hot spot fields take place. As shown in Fig. 3.2 (c), the mean electric field on the QE is maximum at the origin where z = 0 nm. The QE is treated as a two-level system with ground and excited states in the analytical calculations. In 3D simulations it is modeled by a Lorentzian dielectric function [64] with a decay rate of $\gamma_{eg} \approx 10^{11}$ Hz. This indeed, is a low quality QE in terms of the decay rate, however it serves the purpose to demonstrate that even with a low quality QE, the presented phenomenon provides 10^2-10^3 factors of additional enhancement in the system. The typical values for QE decay rates are around 10^9 Hz. Furthermore, the interaction of the QE with the $\hat{a}_{\mathrm{R}}$-mode and the Raman-reporter molecule is neglected for simplicity.

3.2 Analytical Approach

3.2.1 Hamiltonian and Equations of Motion

The system that is introduced in Section 3.1 can be treated with a set of analytical calculations in order to analyze the behaviour of the system. For this purpose, the effective Hamiltonian including the double-resonance scheme coupled with the QE is studied for Raman conversion. The total Hamiltonian, $\hat{\mathcal{H}} = \hat{\mathcal{H}}_0 + \hat{\mathcal{H}}_{\mathrm{QE}} + \hat{\mathcal{H}}_{\mathrm{L}} + \hat{\mathcal{H}}_{\mathrm{int}} + \hat{\mathcal{H}}_{\mathrm{R}}$, can be written in terms of the following,

$$\hat{H}_0 = \hbar\Omega\hat{a}^\dagger\hat{a} + \hbar\Omega_{\mathrm{R}}\hat{a}_{\mathrm{R}}^\dagger\hat{a}_{\mathrm{R}} + \hbar\Omega_{\mathrm{ph}}\hat{a}_{\mathrm{ph}}^\dagger\hat{a}_{\mathrm{ph}}, \tag{3.1}$$

$$\hat{H}_{\mathrm{QE}} = \hbar\omega_{eg} \left|e\right\rangle \left\langle e\right|, \tag{3.2}$$

$$\hat{H}_{\mathrm{L}} = i\hbar(\hat{a}^\dagger\varepsilon e^{-i\omega t} - \hat{a}\varepsilon^* e^{i\omega t}), \tag{3.3}$$

$$\hat{H}_{\mathrm{int}} = \hbar(f\hat{a}_{\mathrm{R}} \left|e\right\rangle \left\langle g\right| + f^*\hat{a}_{\mathrm{R}}^\dagger \left|g\right\rangle \left\langle e\right|), \tag{3.4}$$

$$\hat{H}_{\mathrm{R}} = \hbar\chi(\hat{a}_{\mathrm{R}}^\dagger\hat{a}_{\mathrm{ph}}^\dagger\hat{a} + \hat{a}^\dagger\hat{a}_{\mathrm{ph}}\hat{a}_{\mathrm{R}}). \tag{3.5}$$

Here, $\hat{H}_0$ includes the energies for the driven, $\hat{a}$, and Raman shifted, $\hat{a}_{\mathrm{R}}$, plasmon modes as well as the molecular phonon vibrations, $\hat{a}_{\mathrm{ph}}$. $\hat{H}_{\mathrm{QE}}$ is the energy of the auxiliary QE which is a two-level system with ground $|g\rangle$ and excited $|e\rangle$ states. Here, the ground state energy can be assigned to zero by using the fact that the only quantity that matters is the energy difference between the ground and excited levels [65]. $\hat{H}_{\mathrm{L}}$ denotes the energy of the incident laser pump that drives the $\hat{a}$-mode. $\hat{H}_{\mathrm{R}}$ rep-

resents the Raman process [13–15] and $\hat{H}_{\rm int}$ is the interaction of the auxiliary QE with the Stokes-shifted plasmon-polaritons of $\hat{a}_{\rm R}$-mode. Here the parameter f denotes the interaction strength between the QE and $\hat{a}_{\rm R}$-mode. χ is the overlap integral that determines the strength of the Raman process, while ε represents the strength of the incident laser pump. Coupling of the auxiliary QE to $\hat{a}$-mode is not taken into account due to far-off-resonance.

In this analytical study, localized plasmon modes are chosen to carry and enhance the Raman process instead of unlocalized structures such as photons. The reason for that is, as the light interacts with particles that are smaller than the incoming wavelength, the incident EM-field is confined in the hot spots of the system, creating localized surface plasmon resonances (LSPR). As a result of this localized field at the hot spots, nonlinear processes can be enhanced orders of magnitude. When a molecule is present in the system, localized plasmon polarization interacts with the vibrational modes of the molecule. For the Stokes Raman shift, this process occurs as follows; a plasmon with frequency ω is adsorbed by the molecule, on return exciting a vibrational mode of the molecule, ν, and another plasmon of lower energy $\omega_{\rm R}$ on the surface of the MNS. In fact, at the output and input hot spots, both the excited and converted field intensities are enhanced resulting in a quadratic enhancement of the nonlinear process [65]. If the mediator particle was chosen as an unlocalized object, the overlap integral would be significantly small. However, the experimental studies proved countless times that this is not the case in the physical reality. According to the experimental studies, the emerged Raman intensity is much larger since the generated frequency in the first plasmon mode is converted into the second. The Hamiltonian for this process is depicted in Eq.(2.11) [11].

The dynamics of the system is obtained through Heisenberg equations, $i\hbar\dot{\hat{a}} = [\hat{a}, \hat{H}]$. In this part of the study, the quantum optical effects of the system such as the entanglement features are out of interest, therefore the operators can be replaced with the corresponding complex numbers [66]; $\hat{a} \rightarrow \alpha$, $\hat{a}_{\rm R} \rightarrow \alpha_{\rm R}$, $\hat{a}_{\rm ph} \rightarrow \alpha_{\rm ph}$, $\hat{\rho}_{eg} =$

$|e\rangle\langle g| \rightarrow \rho_{eg}$ and $\hat{\rho}_{ee} = |e\rangle\langle e| \rightarrow \rho_{ee}$. The equations of motions are found as,

$$\dot{\alpha}_{\mathrm{R}} = (-i\Omega_{\mathrm{R}} - \gamma_{\mathrm{R}})\alpha_{\mathrm{R}} - i\chi\alpha^{*}_{\mathrm{ph}}\alpha - if^{*}\rho_{eg}, \tag{3.6}$$

$$\dot{\alpha} = (-i\Omega - \gamma)\alpha - i\chi\alpha_{\mathrm{ph}}\alpha_{\mathrm{R}} + \varepsilon e^{-i\omega t}, \tag{3.7}$$

$$\dot{\alpha}_{\mathrm{ph}} = (-i\Omega_{\mathrm{ph}} - \gamma_{\mathrm{ph}})\alpha_{\mathrm{ph}} - i\chi\alpha^{*}_{\mathrm{R}}\alpha + \varepsilon_{\mathrm{ph}}e^{-i\omega_{\mathrm{ph}}t}, \tag{3.8}$$

$$\dot{\rho}_{eg} = (-i\omega_{eg} - \gamma_{eg})\rho_{eg} + if\alpha_{\mathrm{R}}(\rho_{ee} - \rho_{gg}), \tag{3.9}$$

$$\dot{\rho}_{ee} = -\gamma_{ee}\rho_{ee} + if^{*}\alpha^{*}_{\mathrm{R}}\rho_{eg} - if\alpha_{\mathrm{R}}\rho^{*}_{eg}, \tag{3.10}$$

where the damping rates are introduced as γ, γ_{R}, γ_{ph}, γ_{ee}, and γ_{eg} [65,66] respectively for the excited and Raman converted plasmon modes, phonon coupling and diagonal and off-diagonal elements of QE states. The typical decay rates are; $\gamma = \gamma_{\mathrm{R}} \approx 10^{13} - 10^{14}$ Hz for plasmons, $\gamma_{\mathrm{eg}} = \gamma_{ee}/2 \approx 10^{9}$ Hz for quantum emitters and $\gamma_{\mathrm{ph}} \approx 10^{12}$ Hz for phonon modes. The conservation of probability yields to the constraint $\rho_{ee} + \rho_{gg}$ = 1. $\varepsilon_{\mathrm{ph}}$ is introduced for the vibrations due to the finite ambient temperature [67, 68] however, the actual value of it has no influence in the relative manipulation of the SERS signal.

In the steady-state, solutions take the following form; $\alpha_{\mathrm{R}}(t) = \tilde{\alpha}_{\mathrm{R}}e^{-i\omega_{\mathrm{R}}t}$, $\alpha(t) = \tilde{\alpha}e^{-i\omega t}$, $\alpha_{\mathrm{ph}}(t) = \tilde{\alpha}_{\mathrm{ph}}e^{-i\omega_{\mathrm{ph}}t}$, $\rho_{\mathrm{eg}}(t) = \tilde{\rho}_{\mathrm{eg}}e^{-i\omega_{\mathrm{R}}t}$, $\rho_{\mathrm{ee}}(t) = \tilde{\rho}_{\mathrm{ee}}$. When the steady-state forms are placed in Eqs. (3.6)-(3.10), the exponential terms cancel in each equation. In other words, energy is conserved in the long term limit. Then, Eqs. (3.6)-(3.10) become

$$[i(\Omega_{\mathrm{R}} - \omega_{\mathrm{R}}) + \gamma_{\mathrm{R}}]\tilde{\alpha}_{\mathrm{R}} = -i\chi\tilde{\alpha}^{*}_{\mathrm{ph}}\tilde{\alpha} - if^{*}\tilde{\rho}_{\mathrm{eg}}, \tag{3.11}$$

$$[i(\Omega - \omega) + \gamma]\tilde{\alpha} = -i\chi\tilde{\alpha}_{\mathrm{ph}}\tilde{\alpha}_{\mathrm{R}} + \varepsilon, \tag{3.12}$$

$$[i(\Omega_{\mathrm{ph}} - \omega_{\mathrm{ph}}) + \gamma_{\mathrm{ph}}]\tilde{\alpha}_{\mathrm{ph}} = -i\chi\tilde{\alpha}^{*}_{\mathrm{R}}\tilde{\alpha} + \varepsilon_{\mathrm{ph}}, \tag{3.13}$$

$$[i(\omega_{eg} - \omega_{\mathrm{R}}) + \gamma_{eg}]\tilde{\rho}_{\mathrm{eg}} = if\tilde{\alpha}_{\mathrm{R}}(\tilde{\rho}_{\mathrm{ee}} - \tilde{\rho}_{\mathrm{gg}}), \tag{3.14}$$

$$\gamma_{\mathrm{ee}}\tilde{\rho}_{\mathrm{ee}} = -if\tilde{\alpha}_{\mathrm{R}}\tilde{\rho}^{*}_{\mathrm{eg}} + if^{*}\tilde{\alpha}^{*}_{\mathrm{R}}\tilde{\rho}_{\mathrm{eg}}. \tag{3.15}$$

By solving Eqs. (3.11)-(3.14), a simple expression is obtained for the steady-state Stokes-shifted plasmon amplitude as follows,

$$\tilde{\alpha}_{\mathrm{R}} = \frac{-i\chi\varepsilon^{*}_{\mathrm{ph}}}{\beta^{*}_{\mathrm{ph}}\left([i(\Omega_{\mathrm{R}} - \omega_{\mathrm{R}}) + \gamma_{\mathrm{R}}] - \frac{|f|^{2}y}{[i(\omega_{eg} - \omega_{\mathrm{R}}) + \gamma_{eg}]}\right) - |\chi|^{2}|\tilde{\alpha}|^{2}}\tilde{\alpha}, \tag{3.16}$$

where $\beta_{\rm ph} = [i(\Omega_{\rm ph} - \omega_{\rm ph}) + \gamma_{\rm ph}]$. Here y=$\rho_{ee} - \rho_{gg}$ is the population inversion of the auxiliary QE. $|\chi|^2|\tilde{\alpha}|^2$ term is significantly small compared to the others in the denominator and can be neglected. The enhancement/suppression effects of the SERS signal can be anticipated from Eq. (3.16). It can be seen that, with a proper choice of ω_{eg}, the imaginary parts in the denominator cancel each other, which are the nonresonant term ($\Omega_{\rm R}$-$\omega_{\rm R}$) and the term containing the MNP-QE coupling, f. The condition that maximizes $\alpha_{\rm R}$ in Eq. (3.16) can be found as

$$\omega_{eg}^{*} = \omega_{\rm R} + \frac{|f|^2 y}{2(\Omega_{\rm R} - \omega_{\rm R})} - \sqrt{\frac{|f|^4|y|^2}{4(\Omega_{\rm R} - \omega_{\rm R})^2} - \gamma_{\rm eg}^2}. \tag{3.17}$$

By choosing the level spacing of the QE according to Eq. (3.17), the denominator of Eq. (3.16) can be minimized resulting in the enhancement of the SERS signal amplitude. This type of enhancement does not alter the inner structure of plasmon modes as it emerges from the path interference effects between MNS-QE. The constructive and destructive interference of the frequency conversion paths result in the enhancement/suppression of the SERS amplitude.

The aim of presenting this expression is to provide basic understanding about the path interference effects by simply examining the denominator. Nevertheless, for analytical solutions that are presented in the following section, the Eqs. (3.6)-(3.10) are numerically evolved through time with the initial conditions $\alpha(t = 0) = \alpha_R(t = 0) = 0$ and $\rho_{ee}(t = 0) = \rho_{eg}(t = 0) = 0$. Therefore no assumptions are made when the analytical results are obtained.

3.2.2 Hamiltonian from Optomechanical Model

In Eq. (3.1), a standard, second quantized Hamiltonian is used for the Raman conversion process. According to this Hamiltonian, the frequency conversion occurs between the excited ($\hat{a}$) and Stokes-shifted Raman ($\hat{a}_{\rm R}$) plasmon modes and they both participate in the enhancement process through double localization [13–15, 69]. This mechanism is the result of the $|E|^4$-fold enhancement in the SERS process. In this section, the standard Hamiltonian will additionally be derived from an optomechanical model [67, 68] for a double-resonance scheme [13]. This treatment do not constitute the origin of the frequency conversion Hamiltonian in Eq. (3.1) however it is an

additional approach that ensures the validity of it.

The plasmonic Raman process can also be modeled from an approach that utilizes a radiation-pressure interaction of the plasmons with the molecular vibrations [67, 68]. Therefore, according to this treatment, $\hat{H}_{\mathrm{R}}$ can also be derived from an optomechanical point of view. When the Raman converter molecule is placed in the vicinity of a MNS, the radiation pressure depends on the interaction between the vibrational modes of the molecule and the strength of the electric field at the position where the molecule stands. If a uniform vibration is assumed within the molecule, the interaction density becomes,

$$\hat{H}_{\mathrm{int}}(\boldsymbol{r}) = \hbar g \hat{E}^{\dagger}(\boldsymbol{r})\hat{E}(\boldsymbol{r})\hat{x}f(\boldsymbol{r}), \tag{3.18}$$

which is in the units of [energy]/[volume]. Here, $f(\boldsymbol{r})$ can be considered as a step-function depending on the position of the Raman converter molecule, $f(\boldsymbol{r}) = 1/V$ within the molecular volume and $f(\boldsymbol{r})$ = 0 elsewhere. Assuming a double-resonance scheme for the MNS, the electric field operator can be written as $\hat{E}(\boldsymbol{r}) = \varepsilon_1 u_1(\boldsymbol{r})\hat{a}_1 + \varepsilon_2 u_2(\boldsymbol{r})\hat{a}_2$, where $u_i(\boldsymbol{r})$ is the electric field distribution of the corresponding plasmon mode and ε_{i} has the dimension of the electric field [70]. Therefore, the interaction density is obtained as

$$\hat{H}(\boldsymbol{r}) = \hbar g \left[\varepsilon_1 u_1^*(\boldsymbol{r})\hat{a}_1^{\dagger} + \varepsilon_2 u_2(\boldsymbol{r})\hat{a}_2^{\dagger}\right]\left[\varepsilon_1 u_1(\boldsymbol{r})\hat{a}_1 + \varepsilon_2 u_2(\boldsymbol{r})\hat{a}_2\right] f(\boldsymbol{r})(\hat{b}_{\mathrm{r}}^{\dagger} + \hat{b}_{\mathrm{r}}). \tag{3.19}$$

Here, the terms which do not satisfy the conservation of energy are not taken into account, so Eq. (3.19) becomes,

$$\hat{H}(\boldsymbol{r}) = \hbar g \varepsilon_1 \varepsilon_2 \left[u_1^*(\boldsymbol{r})u_2(\boldsymbol{r})\hat{a}_1^{\dagger}\hat{a}_2\hat{b}_{\mathrm{r}}^{\dagger} + u_1(\boldsymbol{r})u_2^*(\boldsymbol{r})\hat{a}_1\hat{a}_2^{\dagger}\hat{b}_{\mathrm{r}}\right] f(\boldsymbol{r}), \tag{3.20}$$

where the energy of the $\hat{a}_2$-mode is considered to be larger than the energy of $\hat{a}_1$-mode. The total interaction energy is found by integrating Eq. (3.20) over all space,

$$\mathcal{H}(\boldsymbol{r}) = \int d^3\boldsymbol{r}\hat{H}(\boldsymbol{r}) = \Big(\int d^3\boldsymbol{r} f(\boldsymbol{r})u_1^*(\boldsymbol{r})u_2(\boldsymbol{r})\Big)\hbar g \varepsilon_1 \varepsilon_2 \hat{b}_{\mathrm{r}}^{\dagger}\hat{a}_1^{\dagger}\hat{a}_2 + H.c.. \tag{3.21}$$

The dimensionless term in the parenthesis is the overlap integral, I, which determines the strength of the Raman process denoted in the form; $\chi = g\varepsilon_1\varepsilon_2 I$, where g, ε_1, ε_2 are in units of frequency and $\varepsilon_{1,2}$=$(\frac{\hbar\omega_1}{\varepsilon_0 V_1})^2$ [70]. The overlap integral reaches

its higher value when the spatial profiles of the excited and Raman-shifted plasmon modes overlap better with the spatial position of the Raman converter molecule. As a result, Eq. (3.21) takes the form of Eq. (3.1).

3.2.3 Enhancement

To understand the behaviour of the system and examine the dependence of the enhancement to the level spacing of the QE, ($\lambda_{eg} = c/\omega_{eg}$), the equations of motion Eqs. (3.6)-(3.10) are time evolved where QE is initially in the ground state and no plasmon occupation occurs. In the calculations, all parameters are given in proportion with the incident laser pump energy $\omega = 5 \times 10^{14}$ Hz, corresponding to a wavelength of $\lambda = c/\omega$ = 593 nm. Therefore, the decay rates of the plasmon modes are chosen as γ=0.01ω, γ_{R}=0.005ω and γ_{ph}=0.001ω. Nevertheless, it can be realized that Ω_{ph} and γ_{ph} have no effect in the cancellation of the denominator in Eq. (3.16). The spectral width (damping rate) of the auxiliary QE is taken as γ_{eg}=$10^{-5}\omega$. The strength of the Raman process, denoted by the susceptibility χ, is assumed to have a small value such as $\chi = 10^{-5}\omega$. The amplitude (strength) of the initial laser pump is taken as $\varepsilon = 0.1\omega$. To examine the effect of coupling between MNS-QE, the coupling strength f is also varied as f = 0.1ω, 0.105ω, 0.11ω. Additionally, the relative enhancement factor (EF) is calculated as the ratio of the Raman converted mode intensity, $|\alpha_{\mathrm{R}}|^2$, with and without the presence of QE as follows,

$$EF = \frac{|\alpha_{\mathrm{R}}(f \neq 0)|^2}{|\alpha_{\mathrm{R}}(f = 0)|^2}. \tag{3.22}$$

The enhancement factors with respect to the level spacing, ω_{eg}, can be observed in Fig. 3.3 for different values of coupling strengths, f. The additional enhancement due to nonlinear path effects is around 300 factors. Close examination of Eq. (3.17) reveals that when $\Omega_{\mathrm{R}} < \omega_{\mathrm{R}}$, the maximum enhancement shift to longer wavelengths of $\lambda_{eg} = c/\omega_{eg}$ as the coupling strength f increases. Therefore, as can be seen from Eq. (3.16), introducing additional interference paths via additional QEs [71] or plasmon conversion modes will result in an increased amount of enhancement. Eq. (3.16) provides a pure and simple tool to understand the possible interference effects without including any complications.

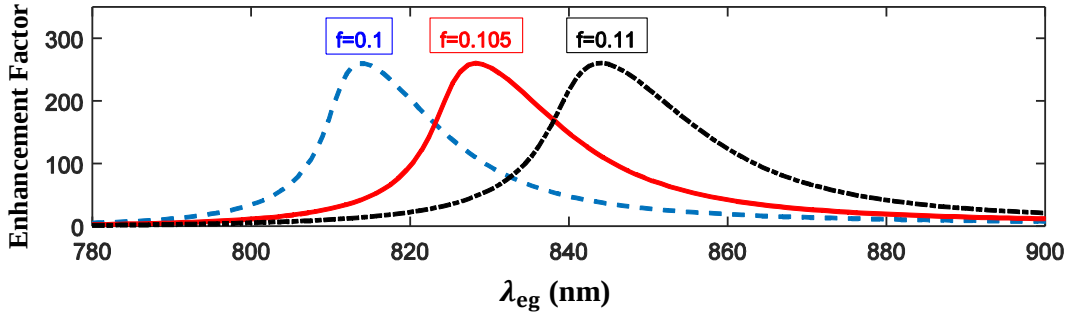

Figure 3.3: Numerical time evolution results of the Raman enhancement factor with respect to the QE level spacing values, λ_{eg}. Here, this enhancement of SERS signal is due to the path interference effects and adds up to the enhancement due to the hot spot localization. Presence of the QE, with level spacing $\lambda_{eg} = c/\omega_{eg}$ creates a growth in the SERS response according to Eq. (3.16). It can be observed that as the interaction strength decreases, the QE level spacing values shift to the shorter wavelengths to generate maximum enhancement.

In Fig. 3.3, the damping rate of the QE is taken to be γ_{eg}=$10^{-5}\omega$, which corresponds to a frequency around 5×10^9 Hz. This value is determined by taking the approximate damping ratio of adsorbed molecules in metal surfaces. However, such a good quality QE is not a requirement to achieve the enhanced Raman signal. In Fig. 3.4 it can be observed that even when the damping rate of the QE is increased to γ_{eg}=$10^{-2}\omega$ (which coincides with the decay rate of the plasmonic oscillations), an enhancement factor around 2 orders of magnitude would still emerge. This result shows that even by using a QE of poor quality in terms of its damping rate, the nonlinear path interference can take place.

3.2.4 Suppression

Besides the enhancement phenomenon, Eq. (3.16) also predicts the suppression of the SERS signal for the resonance condition $\omega_{eg} = \omega_{\mathrm{R}}$. This suppression takes place up to several orders of magnitude. As depicted in Section 2.4, when a discrete state interacts with a continuum, the excited state becomes weakly hybridized into two different

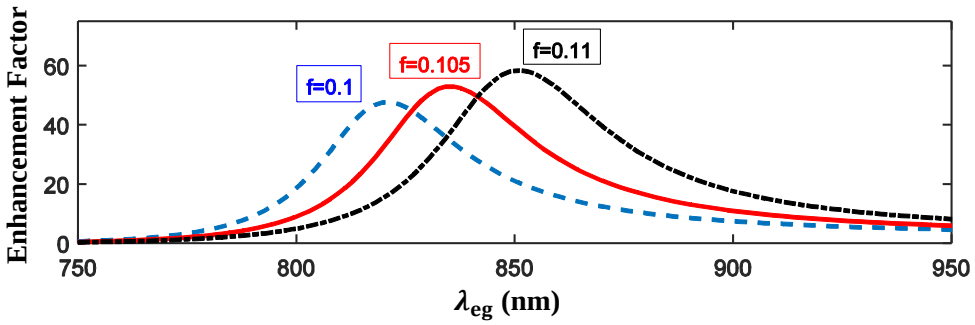

Figure 3.4: The effect of using a poor quality QE in terms of its damping rate on the Raman enhancement factors. The damping rate of the QE is increased to resemble the decay rate of the plasmon oscillation modes, $\gamma_{eg} = 10^{-2}\omega$. Even with this value of the damping rate, there still occurs an enhancement factor around ~ 100.

states albeit their resolution still remains in the broadening of the excited state. Since these two pathways are out of phase with each other, a transparency window occurs in the absorption spectra. In the plasmonic case, for the resonance condition $\omega_{eg} = \omega_{\mathrm{R}}$, the Fano resonance prevents the plasmon oscillations of the converted frequency ω_{R} from emerging into the $\hat{a}_{\mathrm{R}}$-mode. As compared with Eq. (3.16), the path interference in the nonlinear response resembles the interference that occurs in the linear response depicted in Eq. (2.16) [72]. The modification patterns created in the denominators of both equations have a common form [11, 12].

When the level spacing of the QE is chosen in resonance with $\hat{a}_{\mathrm{R}}$-mode, i.e., $\omega_{eg} = \omega_{\mathrm{R}}$, the term that contains the coupling strength in the denominator of Eq. (3.16) becomes $|f|^2 y/\gamma_{eg}$. Since $\gamma_{eg} \approx 10^{-5}\omega$ is very small compared to f =0.1ω, the aforementioned term makes the denominator very large. As a result, the SERS signal is restrained around $\sim 10^{10}$ factors. Fig. 3.5 is obtained by taking the numerical time evolution results of Eqs. (3.6)-(3.10). That means, Fig. 3.5 is generated through exact solutions and no approximations are used.

3.3 3 Dimensional Simulations

Besides the basic understanding provided by Eq. (3.16), simulations with exact solutions of 3D Maxwell equations are also performed to verify the presence of the

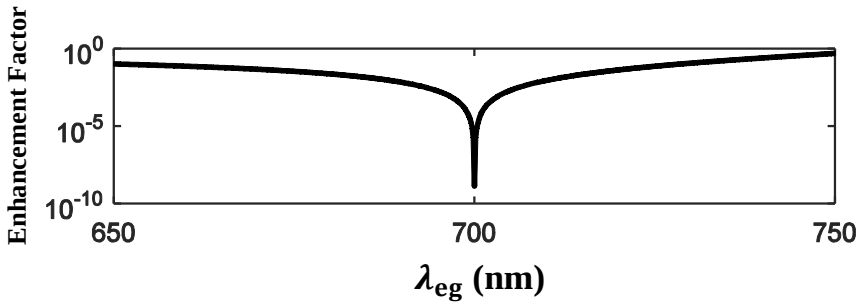

Figure 3.5: Suppression of the SERS signal due to path interference effects. From analytical point of view, presence of an auxiliary QE with a level spacing in resonance with the $\hat{a}_{\rm R}$-mode as $\omega_{\rm R} = \omega_{eg} = c/\lambda_{eg}$, yields a cancellation in the denominator of the SERS response in Eq. (3.16).

enhancement. It should be stressed that the aim here is neither to compare analytical solutions with 3D simulation results, nor to provide a perfectly working setup for future experiments. The basic purpose here is to show that if the retardation effects would wipe out the enhancement phenomenon predicted by the basic analytical model. Making a one to one comparison between the analytical solutions and the 3D simulations is out of scope of this research.

The 3D solutions of the system are performed by using MNPBEM, a toolbox that is created for use in Matlab, which simulates metallic nanoparticles (MNPs) by using a boundary element method (BEM) approach [56]. Simulating particle plasmons requires the solution of Maxwell's equations for MNPs embedded in a dielectric environment. Within the toolbox, environments with homogeneous and isotropic dielectric functions are split by abrupt interfaces, rather than allowing for a general inhomogeneous dielectric environment. The toolbox is proved to work at its best for frequencies in the optical and near-infrared regime, and for MNPs ranging from a few to a few hundreds of nanometers. For most plasmonic applications with embedded MNPs in a dielectric background, the BEM approach appears as the easy going choice of solution. In this approach, only the boundaries between the materials are discretized instead of the whole volume, therefore faster simulations that require moderate memories can be conducted. Over the years, the toolbox have been used and

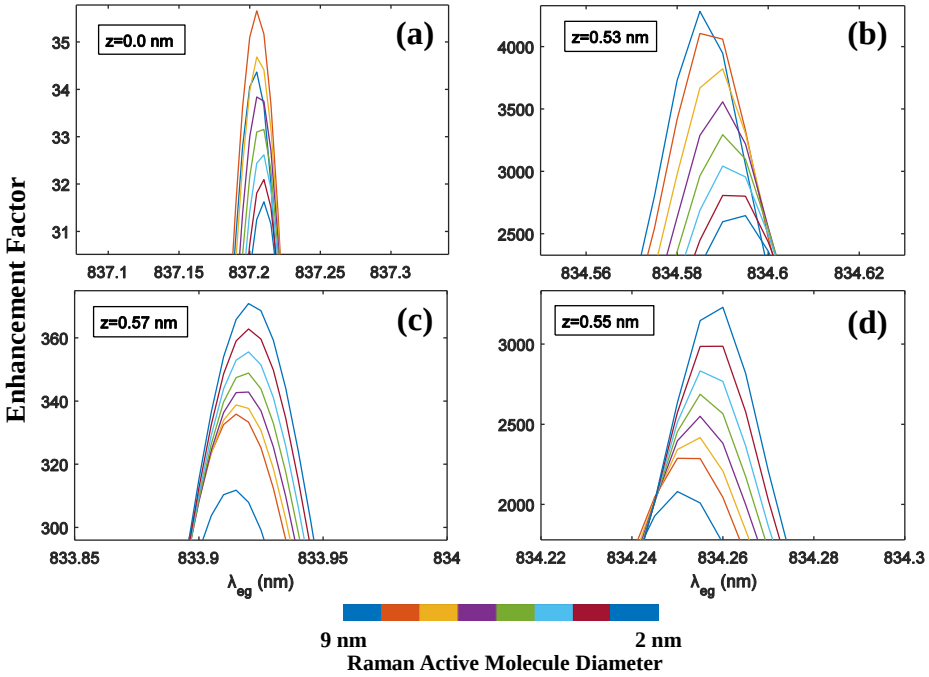

Figure 3.6: Different values of Raman enhancement factors for different sizes of Raman reporter molecule. All the sizes of Raman reporter molecule is simulated according to different spatial positions of auxiliary QE, (a) z=0.0 nm, (b) z=0.53 nm, (c) z=0.55 nm, (d) z=0.57 nm. It is observed that the size of the reporter does not alter the order of magnitude of the generated enhancement values.

tested for the simulations of optical properties of plasmonic particles [73,74], surface enhanced spectroscopy [75–77] and electron energy loss spectroscopy (EELS) [56]. Although the MNPs and the environment are well defined in the toolbox, the calculation of nonlinear Raman response for a plasmonic system was lacking. Therefore a Raman module is developed within the toolbox.

For the simulations, the setup in Fig. 3.1 is used. In Fig. 3.1 (a), a nano dimer is presented with two gold spheres of radii 90 nm and 55 nm. The linear response of the dimer under the driving field of λ=593 nm is shown in Fig. 3.1 (b). The dimer supports two plasmon modes at $\Lambda=c/\Omega$=530 nm and $\Lambda_{\mathrm{R}}=c/\Omega_{\mathrm{R}}$=780 nm, where the EM field of wavelength λ=593 nm drives the $\hat{a}$-mode. Two hot spots corresponding to the two plasmon modes of the dimer are shown in Fig. 3.2 (a)-(b). Apparent from the figure, the two hot spots spatially coincide.

A Raman reporter molecule with a radius of 4 nm [63] (blue), is placed in the close vicinity of the hot spots of the MNP dimer. Nonetheless, the size and shape of the Raman reporter molecule do not have a significant effect on its polarizability and hence, on the enhancement factor of the SERS signal. In Fig. 3.6, the Raman enhancement factors are shown for different diameter values for Raman converter molecule. The results are presented for different spatial positions of QE with respect to the MNP center; (a) z=0.0 nm, (b) 0.53 nm, (c) 0.55 nm and (d) 0.57 nm. From the figure, it is evident that only a 2-fold increase in the Raman enhancement occurs as the diameter of the Raman converter molecule is increased from 2 nm to 9 nm. Therefore, it can be stated that the diameter of the Raman converter molecule does not alter the order of magnitude in the enhancement factors. Typically, a protein molecule would have the diameter of approximately 3-4 nm [63], so the size of the Raman converter molecule is taken as 4 nm in the 3D simulations. Also, the relative permittivity of the Raman converter molecule is chosen very close to that of air, ~ 1.05, to exclude any further complications that may arise from the presence of the molecule.

The Raman reporter molecule is chosen to have only a single vibrational mode at $\nu = 2600\ \mathrm{cm}^{-1}$ [78]. This choice is fully functional since only a "proof-of-principle" demonstration is aimed in this study. With this vibrational mode of the reporter, the Stokes signal appears at λ_{R}=700 nm and couples to a_{R} mode of the double-resonant structure [13].

The final component of the system, the auxiliary QE with the resonance wavelength $\lambda_{eg} = c/\omega_{eg}$, is chosen to have 4 nm of radius with an assigned dielectric function of a sharp Lorentzian shape $\epsilon(\omega)$ [64] which can be observed in Fig. 3.7. The damping rate of the QE is denoted as γ_{eg}.

Likewise the analytical solutions, the enhancement factor (EF) is calculated according to Eq. (3.22). That is, by introducing the auxiliary QE with a sharp Lorentzian dielectric function [64], it is observed that how the SERS response of the system changes in proportion with the case where the QE is not present. In the absence of the QE, the SERS enhancement is only due to the localization of the incident field in the vicinity of hot spots. Numerically, by multiplying the localized electric field values for the excited (593 nm) and Stokes-shifted (700 nm) fields, the enhancement

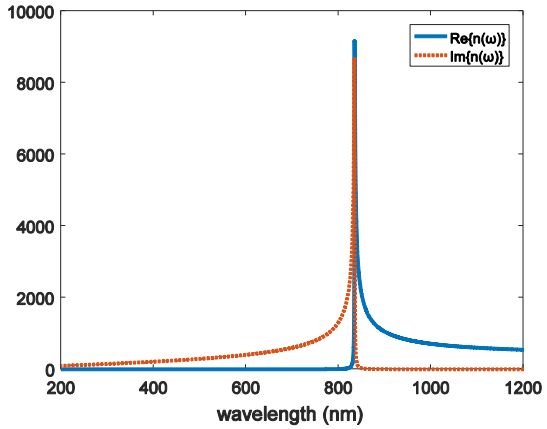

Figure 3.7: The sharp Lorentzian dielectric function, $\epsilon(\omega)$ that represents the auxiliary QE in 3D simulations. A sharp Lorentzian function in the form of $\epsilon = 1+2\omega_p^2/(\omega_{eg}^2 - \omega^2 - i2\gamma_{eg}\omega)$ is used in order to generate an object with discrete energy levels.

due to localization can be found as EF(ω)× EF(ω_{R}) [69], which can be high as 10^8 factors. It is worthy to note that this amount of enhancement is already present in the system in the form of regular SERS mechanism due to localization. On top of this, the simulations using the MNPBEM toolbox [56] enables the utilization of the enhancement via path interference with this phenomenon of localization.

When the QE coupling is introduced to the system, it is observed in Fig. 3.8 that the exact solutions of the 3D Maxwell equations yield to an extra enhancement as a result of path interference. From the figure, it is observed that the enhancement occurs where λ_{eg} is positioned at longer wavelengths than $\hat{a}_{\mathrm{R}}$-mode. This result is consistent with what is predicted by Eq. (3.17). In addition, the position of the auxiliary QE is slightly altered along the z-axis in Fig. 3.8. This is performed in order to manipulate the interaction of the QE with the MNS hot spots. In other words, this treatment corresponds to changing the QE-MNS coupling by altering f in Fig. 3.3. As the distance (z) of the QE to the hot spot center (z = 0 nm) increases, its interaction with the plasmon mode decreases drastically. Therefore, small values of z means stronger interaction coupling for QE-MNP. From Fig. 3.8, it is evident that as the MNP-QE coupling gets stronger, the enhancement shifts to longer wavelengths, as the analytical solutions predict in Fig. 3.3.

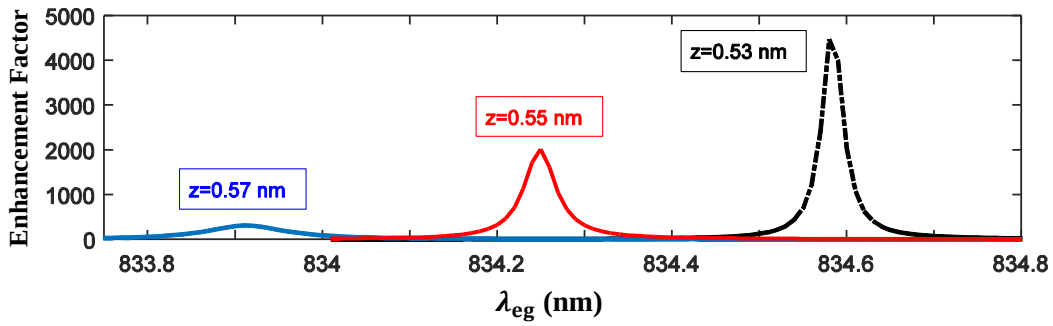

Figure 3.8: The additional enhancement of SERS via path interference which is obtained by using the exact solutions of 3D Maxwell equations. When the QE is introduced to the system, the localization of the fields on the Raman converter remains unchanged, however, the SERS signal is increased around 10^3-10^4 factors. This amount of increment multiplies with the enhancement that is already present in the system as a result of the localization. The additional enhancement occurs as predicted by the analytical model in Section 3.2.3 and shifts to longer wavelengths as the MNS-QE coupling increases. In the simulations, moving QE closer to the center of the dimer (z=0) implies that the interaction between QE and the hot spots are getting stronger, until the system reaches to a region where it enters to a strong coupling regime.

Furthermore, maximum enhancement in Raman signal occurs for the level spacing of the QE around $\lambda_{eg} \sim 834$ nm, which is farther apart from the Stokes line at λ_{R} = 700 nm. This is an important fact because if the hot spot enhancement would be the result of the linear Fano resonance, it should occur around $\lambda_{eg} \sim \lambda_{\mathrm{R}}$. Hence, to avoid a possible confusion, λ_{eg} is chosen to be far from Stokes line, both in the 3D simulations and in the analytical solutions.

However, in experimental conditions, it is prominent that placing a molecule at a certain point might not be a realistic expectation. Also it is not practical to assume that a bunch of molecules in a setup would have exactly the same level spacing values. Instead, it can be thought as a mixture of molecules with quite similar, but not equal level spacing values. Fig. 3.9, aims to provide some insight about the expectations of the simple treatment.

In Fig. 3.9 (a), the Raman enhancement factor is shown as a function of the QE position with respect to the center of MNP dimer. It can be observed that a sprinkled bunch of molecules in the vicinity of the hot spots would yield to an overall enhancement. It should be clarified that stronger interaction, f, does not always point out to an enhancement in the Raman signal. From Fig. 3.9 (a), the amount of enhancement can be observed as a function of the QE position. When the auxiliary QE is positioned too close to the center of the dimer (z < 0.5 nm), the interaction between the QE and the $\hat{a}_{\mathrm{R}}$-mode becomes higher and the system shifts into the strong interaction regime. The enhancement experiences a drop around 2 orders of magnitude. In this case, the excitations in the QE and the MNP dimer cannot be modeled with the simple analytical approach. Hence, Eq. (3.16) becomes invalid for this regime. This phenomenon also observed in the second harmonic generation (SHG) in Ref. [79].

Similarly, Fig. 3.9 (b) denotes maximum enhancement curve for a bundle of molecules with slightly different level spacing values. In that case, the overall enhancement displays similar behaviour to that of Fig. 3.9 (a). Unfortunately, it is not possible to demonstrate the suppression effect with the 3D simulations [56], neither for SHG nor for the Raman setups. Demonstration of the suppression phenomenon requires the self-consistent solution of Maxwell equations, as in the case for solving Eqs. (3.6)–(3.10). This cannot be realized with the BEM approach and 3D simula-

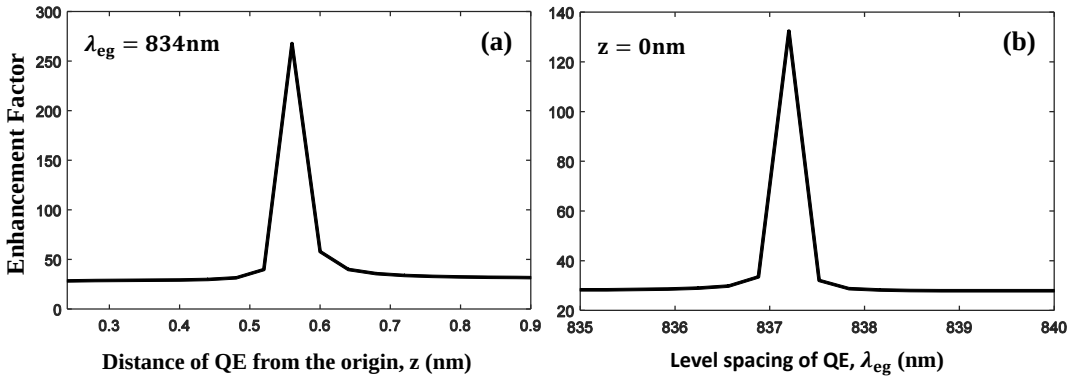

Figure 3.9: The results of 3D simulations for the maximum enhancement factors with respect to the (a) slightly different level spacing values and (b) slightly different positions of the QE. (a) When the QE is brought closer to the center of the dimer, the enhancement factor starts to decrease as the system moves into the strong coupling regime. The simple treatment that is presented here cannot model the excitations in the strong coupling regime. For practical reasons, it is not realistic to expect that a bunch of molecules could have the exact same level spacing values, as well as could be placed to certain positions without any errors. Instead, a bundle of molecules with similar level spacing values can be placed to a close vicinity near the desired point. This figure shows what might be the possible enhancement achievement according to realistic expectations.

tions only remain a first-order approach without self-consistency effects.

3.4 Coupling to a Long-live Dark Plasmon Mode: Analytical Approach

In Section 3.2.1, a simple analytical model is presented where coupling of a QE with a double-resonance MNS generates path interference effects and introduce an extra term in the denominator of the Raman signal amplitude. This additional term cancels with the nonresonant term of the Stokes signal. Here in this section, it is presented that a similar phenomenon occurs when instead of a QE, the $\hat{a}_{\mathrm{R}}$-mode is coupled to a dark state whose lifetime is larger than the plasmon oscillations in the $\hat{a}_{\mathrm{R}}$-mode.

Hamiltonian and EOM. In order to analyze dark-mode (DM) coupling with the MNP dimer, some terms in the Hamiltonian of Section 3.2.1 should be modified. The

energy of the dark-mode excitations is introduced as H_{DM} and the interaction of it with MNP dimer is given as H_{int}. The total Hamiltonian becomes,

$$\begin{aligned}
\hat{H} &= \hat{H}_{\mathrm{R}} + \hat{H}_0 + \hat{H}_{\mathrm{L}} + \hat{H}_{\mathrm{int}} + \hat{H}_{\mathrm{DM}},\\
\hat{H}_{\mathrm{R}} &= \hbar\chi(\hat{a}_{\mathrm{R}}^{\dagger}\hat{a}_{\mathrm{ph}}^{\dagger}\hat{a} + \hat{a}^{\dagger}\hat{a}_{\mathrm{ph}}\hat{a}_{\mathrm{R}}),\\
\hat{H}_0 &= \hbar\Omega_{\mathrm{R}}\hat{a}_{\mathrm{R}}^{\dagger}\hat{a}_{\mathrm{R}} + \hbar\Omega\hat{a}^{\dagger}\hat{a} + \hbar\Omega_{\mathrm{ph}}\hat{a}_{\mathrm{ph}}^{\dagger}\hat{a}_{\mathrm{ph}},\\
\hat{H}_{\mathrm{L}} &= i\hbar(\hat{a}^{\dagger}\varepsilon e^{-i\omega t} - \hat{a}\varepsilon^{*}e^{i\omega t}) + i\hbar(\hat{a}_{\mathrm{ph}}^{\dagger}\varepsilon_{\mathrm{ph}}e^{-i\omega_{\mathrm{ph}}t} - \hat{a}_{\mathrm{ph}}\varepsilon_{\mathrm{ph}}^{*}e^{i\omega_{\mathrm{ph}}t}),\\
\hat{H}_{\mathrm{int}} &= \hbar(f_c\hat{a}_{\mathrm{R}}\hat{a}_{\mathrm{c}}^{\dagger} + f_c^{*}\hat{a}_{\mathrm{R}}^{\dagger}\hat{a}_{\mathrm{c}}),\\
\hat{H}_{\mathrm{DM}} &= \hbar\omega_{\mathrm{c}}\hat{a}_{\mathrm{c}}^{\dagger}\hat{a}_{\mathrm{c}}.
\end{aligned} \tag{3.23}$$

The dark-mode supports plasmonic oscillations, $\hat{a}_{\mathrm{c}}$, due to its coupling to the near-field of the $\hat{a}_{\mathrm{R}}$-mode. Its resonance frequency is denoted as ω_{c} and the strength of its coupling with the MNP dimer is f_c. Furthermore, the equations of motion are obtained as,

$$\dot{\alpha_{\mathrm{R}}} = (-i\Omega_{\mathrm{R}} - \gamma_{\mathrm{R}})\alpha_{\mathrm{R}} - i\chi\alpha_{\mathrm{ph}}^{*}\alpha - if_c^{*}\alpha_{\mathrm{c}}, \tag{3.24}$$

$$\dot{\alpha} = (-i\Omega - \gamma)\alpha - i\chi\alpha_{\mathrm{ph}}\alpha_{\mathrm{R}} + \varepsilon e^{-i\omega t}, \tag{3.25}$$

$$\dot{\alpha_{ph}} = (-i\Omega_{\mathrm{ph}} - \gamma_{\mathrm{ph}})\alpha_{\mathrm{ph}} - i\chi\alpha_{\mathrm{R}}^{*}\alpha + \varepsilon_{\mathrm{ph}}e^{-i\omega_{\mathrm{ph}}t}, \tag{3.26}$$

$$\dot{\alpha}_{\mathrm{c}} = (-i\omega_{\mathrm{c}} - \gamma_{\mathrm{c}})\alpha_{\mathrm{c}} - if_c\alpha_{\mathrm{R}}, \tag{3.27}$$

where the plasmonic oscillation mode of the DM can be replaced with the corresponding complex number $\hat{a}_{\mathrm{c}} \rightarrow \alpha_{\mathrm{c}}$ [66]. The damping rate, γ_{c} for the DM is chosen to be smaller than the decay rate of the excited plasmon field, γ. In the steady-state, the expressions for the plasmonic modes α_{R}, α, α_{ph} and α_{c} are written as,

$$\begin{aligned}
\beta_{\mathrm{R}}\tilde{\alpha}_{\mathrm{R}} &= -i\chi\tilde{\alpha}_{\mathrm{ph}}^{*}\tilde{\alpha} - if^{*}\tilde{\alpha}_{\mathrm{c}},\\
\beta\tilde{\alpha} &= -i\chi\tilde{\alpha}_{\mathrm{ph}}\tilde{\alpha}_{\mathrm{R}} + \varepsilon,\\
\beta_{\mathrm{ph}}\tilde{\alpha}_{\mathrm{ph}} &= -i\chi\tilde{\alpha}_{\mathrm{R}}^{*}\tilde{\alpha} + \varepsilon_{\mathrm{ph}},\\
\beta_{\mathrm{c}}\tilde{\alpha}_{\mathrm{c}} &= -if\tilde{\alpha}_{\mathrm{R}},
\end{aligned} \tag{3.28}$$

where $\beta_c \equiv [i(\omega_c - \omega_{\mathrm{R}}) + \gamma_c]$, $\beta \equiv [i(\Omega - \omega) + \gamma]$, $\beta_{\mathrm{R}} \equiv [i(\Omega_{\mathrm{R}} - \omega_{\mathrm{R}}) + \gamma_{\mathrm{R}}]$ and $\beta_{\mathrm{ph}} \equiv [i(\Omega_{\mathrm{ph}} - \omega_{\mathrm{ph}}) + \gamma_{\mathrm{ph}}]$.

The enhancement factor, $|\tilde{\alpha}_{(\mathrm{R},c)}/\tilde{\alpha}_{(\mathrm{R},0)}|^2$, is obtained by neglecting the very small

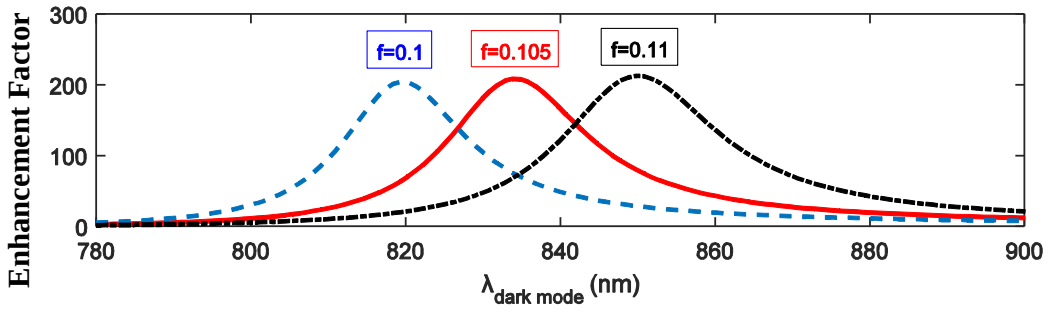

Figure 3.10: The analytical Stokes-shifted enhancement results of dark-mode coupling to the MNS. The similar positioning of maximum enhancement with respect to $\lambda_{\text{dark mode}}$ is observed compared to Fig. 3.8.

term including $|\chi|^2$, as

$$\frac{\tilde{\alpha}_{(\mathrm{R,c})}}{\tilde{\alpha}_{(\mathrm{R},0)}} = \frac{[i(\Omega_{\mathrm{R}} - \omega_{\mathrm{R}}) + \gamma_{\mathrm{R}}][i(\omega_{\mathrm{c}} - \omega_{\mathrm{R}}) + \gamma_{\mathrm{c}}]}{[i(\Omega_{\mathrm{R}} - \omega_{\mathrm{R}}) + \gamma_{\mathrm{R}}][i(\omega_{\mathrm{c}} - \omega_{\mathrm{R}}) + \gamma_{\mathrm{c}}] + |f_{\mathrm{c}}|^2}. \tag{3.29}$$

Here, $\alpha_{(\mathrm{R,c})}$ ($\alpha_{(\mathrm{R},0)}$) is the Stokes amplitude with (without) the coupling of the auxiliary structure supporting the DM. By time evolving Eqs. (3.24)-(3.27), the enhancement factors depicted in Fig. 3.10 can be obtained. Furthermore, from Fig. 3.11 it is evident that the suppression effect also takes place for the coupling of objects with larger damping rates around the range of γ_{c}. Also, Eq. (3.29) reveals the condition in which the cancellation occurs in the denominator due to the presence of $|f_c|^2$. It is important to stress that the Fano resonance have a classical correspondence, and the coupling of a DM to the MNS reveals this property of the Fano effect.

3.5 Comments on Possible Implementations

The analytical model that is presented in Section 3.2 is a basic model which provides a "proof of principal" demonstration of the SERS enhancement along with the 3D simulations in Section 3.3. Many complications may arise while performing 3D solutions of Maxwell equations, and obviously the basic analytical model is not brought up to overcome these complications. For instance, the change in the density of states, i.e. the Purcell effect, the coupling of the fields to possible dark modes and the retardation effects are not taken into account in the basic analytical model. The retardation

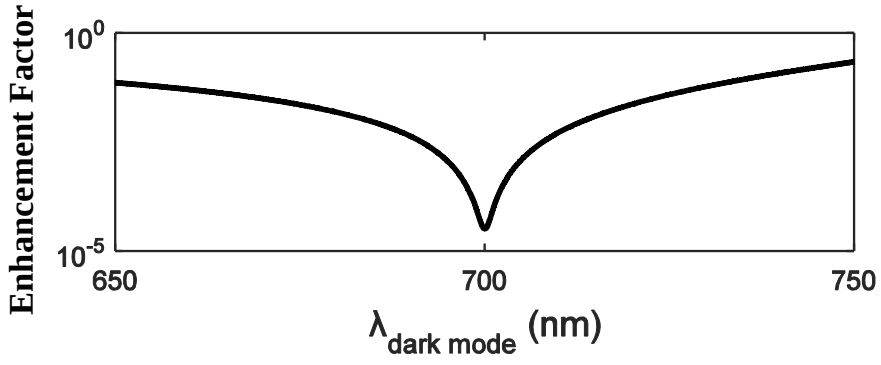

Figure 3.11: The suppression of the Stokes-shifted Raman signal in the case of DM coupling to the λ_{R}-mode of the MNS. At the resonance condition where $\lambda_{\mathrm{DM}} = \lambda_{\mathrm{R}}$ = 700 nm, the suppression takes place for several orders of magnitude.

effects show up in the 3D simulations as the narrower band structures in Fig. 3.8 compared to the analytical solutions in Fig. 3.3. A similar effect is observed in Ref. [62] for the SH process. Even with the simple setting presented in Fig. 3.1, attaching a QE to the hot spots of the MNP dimer generates an enhancement factor around 10^2-10^3.

Considering structures with wider hot spots, such as a metal-coated atomic force microscope (AFM) tip, the accurate placing of the QE may not be necessary, and similar factors of enhancement can be obtained. The setup that is presented here, along with the basic analytical model, can be utilized with several methods in nanotechnology such as e-beam lithography [80, 81] or DNA based bio-molecular recognition [82, 83] which provide nanoscale spatial control. For example, DNA strands can be utilized as rulers for positioning nanomaterials along with the metal nanoparticles [82]. By choosing proper length of DNA strands, self-assembled generation of nanoparticles can be achieved [83]. Moreover, plasmonic gaps of bow-tie nanoantennas can be selectively filled with dielectric nanoparticles by using electron beam lithography process [80, 81].

In Fig. 3.12, an AFM tip can be observed, which localizes the incident E-field into the plasmonic oscillations. When a Raman active molecule (green) is present on the substrate, tip enhanced Raman scattering (TERS) occurs as a result of the strong localized field. In Ref. [84], such a setup is demonstrated including a tip that supports

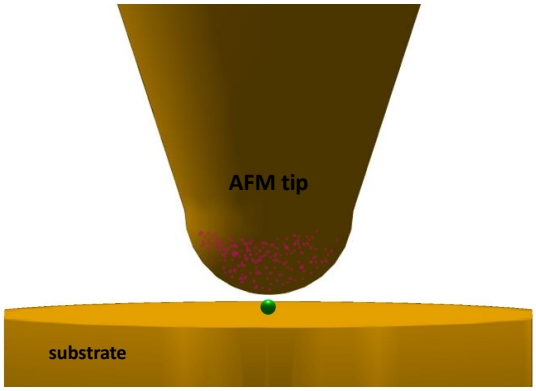

Figure 3.12: The setup of an AFM tip utilized with a Raman reporter molecule. The simple analytical model proposes that when the AFM tip is contaminated with appropriate auxiliary molecules, the path interference effects will be introduced and an enhanced TERS signal will be produced without increasing near-field intensity.

three plasmon modes in the optical regime. The second plasmon mode is excited in order to uncover a Stokes-shifted signal in the third plasmon mode with longer wavelength. Therefore, the second and third modes of the system act as double-resonance SERS (TERS) mechanism. The TERS signal can be further enhanced if the AFM tip is decorated (in other words, contaminated) with appropriately chosen molecules (QEs). Appearing as purple structures in Fig. 3.12, the molecules will introduce path interference effects and produce an enhanced TERS signal without increasing near-field intensity. A technique similar to dip-pen lithography can produce the decoration of the tip edge. For instance, in spasers where MNPs are surrounded by molecules, the plasmon lifetime and fluorescence intensity of the molecules are increased as a result of linear Fano resonances [85]. What is more, Fano resonances can also be utilized in all-plasmonic settings [43, 86].

To conclude, the nonlinear SERS response of a coupled MNP-QE system is studied in this chapter. Both the analytical results and the 3D solutions of Maxwell equations show that it is possible to enhance the SERS signal without altering the electric field profiles on the Raman active molecules. An enhancement around 10^2-10^3 factors occurs when the QE is coupled to the double-resonant MNP dimer as a result of the path interference effects. Although the presence of the enhancement phenomenon is verified both with the numerical time evolution results and the 3D Maxwell equations,

it is not aimed to make a one to one comparison between the analytical findings and the 3D simulations. The main purpose is to show that if the Fano resonance in the nonlinear regime is washed out with the retardation effects or not. It is observed that, although the retardation effects significantly narrow the enhancement bands with respect to the level spacing values, λ_{eg}, the silent Raman enhancement phenomenon is still present in the system.

CHAPTER 4

FANO CONTROL OF NONCLASSICALITY

4.1 Introduction

In the year of 1935, an article is published by Einstein, Podolsky and Rosen, unleashing a great controversy in quantum physics that would last for years [87]. In the article, two quantum systems are assumed to interact where both their spatial distance and linear momenta are connected with each other, even when the spatial distance between them is widely large. Since the two states are "entangled" in this sense (though the word "entangled" is assigned later on), determining the position of one system would also enable the prediction of the position of the other. The same is valid for the linear momenta of the systems. This phenomenon is used to argue that the quantum mechanics cannot be a complete theory in terms of local action conditions and fails to describe the physical reality. However, after the interpretation of Bell's inequalities, it is experimentally verified that the nonlocal character of these states are actual facts that are emerging from the quantum nature of the universe [88]. From the time it was posed as a paradox, the entanglement phenomenon now became the heart of development in quantum physics and information processing theory [25]. Among some applications of it, quantum cryptography [89], dense coding [90], entanglement swapping [91, 92] and quantum teleportation [93, 94] can be counted.

As a result of its significance in many fields of science, it is of importance to detect and quantify the entanglement that quantum systems possess. In a sense, entanglement is like energy; once generated, they both can be converted into different forms and consumed through executable tasks [24]. Beam splitter operations, one of the known devices that generate entangled states, are studied to show that nonclassicality

of the input state is a necessary condition to obtain entanglement at the output [25]. As a result of beam splitter-like operations, a single-mode nonclassical state (a squeezed state, for instance) can be converted into two-mode entangled states [25–27]. The generated entanglement at the output becomes stronger when the single-mode nonclassicality is larger. Therefore, the amount of two-mode entanglement at the beam splitter output can be used as a single-mode nonclassicality (SMNc) measure.

In the case of a two-level system, entanglement can be quantified with a single real number. In experimental point of view, the number of emerging photons or the phase of a beam can be used to identify the SMNc of an input state. There are various approaches to determine and quantify the SMNc of a system, all with their own ups and downs. One of the approaches, brought up by Asboth et al. [28], links the degree of nonclassicality of an input single-mode field with its ability to produce entangled two-mode states at the output of a beam splitter [24,29,95–97]. Additionally, a recent study by Vogel and Sperling [98, 99] demonstrates that the rank of the output two-mode entanglement is equal to the rank of the expansion of the nonclassical input state in terms of the classical coherent states [24].

A nonclassical single state (with an annihilation operator $\hat{a}$) can be represented in terms of the coherent states $|\alpha_i\rangle$ as,

$$|\psi_{\mathrm{Ncl}}\rangle = \sum_{i=1}^{r} \kappa_i \, |\alpha_i\rangle \, . \tag{4.1}$$

At the output of a beam splitter, this input state generates two-mode entangled states of the $\hat{a}_1$ and $\hat{a}_2$ modes as;

$$|\psi_{\mathrm{Ent}}\rangle = \sum_{i=1}^{r} \lambda_i \, |a_1^{(i)}\rangle \otimes |a_2^{(i)}\rangle \, . \tag{4.2}$$

Here, r is the entanglement rank and κ_i, λ_i are expansion coefficients. Moreover, the beam splitter transformation can be used to further connect the single-mode nonclassicality and the two-mode criteria [100].

In this chapter, the second harmonic response of a system similar to what is presented in Fig. 3.1 is studied. A QE is coupled to the hot spots of a double-resonant MNS. The QE is pumped with a small source in order to further control the nonlinear response of the system. The steady-state second harmonic response is evaluated by solving the

Heisenberg equations for the system. Processing numerical time evolution enables one to understand the behaviour of the system in the steady-state without making any assumptions. According to the results, source controlled QE can provide further enhancement of the SH signal. Here, a question arises whether this enhancement is a result of the path interference as expected, or is it just a direct result of the energy provided with the small source that drives the QE? To provide an answer to this question, the nonclassicality features of the system can be used. By utilizing the beam splitter approach, the entanglement amount of the SH signal, in other words the nonclassicality of the nonlinear response is determined. In order to witness and quantify the nonclassicality, the Simon-Peres-Horodecki entanglement criterion is utilized. The beam splitter transformations are used to obtain the two-mode variances of the output state, in terms of the noise fluctuations in the input state, $\langle \hat{a}^2 \rangle$ and $\langle \hat{a}^\dagger \hat{a} \rangle$. As a result, the nonclassicality measures can be evaluated as a function of the single-mode state variances. Analyzing the behaviour of entanglement with respect to the second converted field intensity generates an understanding about how the Fano type resonances effect the control of nonclassicality in a plasmonic structure.

4.2 Theoretical Model

Similar to the theoretical model presented in Section 3.2.1, the coupled double-resonant MNS-QE system is represented by a simple theoretical model. In this model, the QE is controlled by a small source of frequency 2ω. The following Hamiltonian is used to define the system [101];

$$\hat{\mathcal{H}} = \hat{\mathcal{H}}_0 + \hat{\mathcal{H}}_{\rm SHG} + \hat{\mathcal{H}}_{\rm QE} + \hat{\mathcal{H}}_{\rm int} + \hat{\mathcal{H}}_{\rm source} + \hat{\mathcal{H}}_{\rm pump}, \tag{4.3}$$

$$\hat{\mathcal{H}}_0 = \hbar\Omega_1 \hat{a}_1^\dagger \hat{a}_1 + \hbar\Omega_2 \hat{a}_2^\dagger \hat{a}_2, \tag{4.4}$$

$$\hat{\mathcal{H}}_{\rm SHG} = \hbar\chi^{(2)}(\hat{a}_2^\dagger \hat{a}_1 \hat{a}_1 + \hat{a}_1^\dagger \hat{a}_1^\dagger \hat{a}_2), \tag{4.5}$$

$$\hat{\mathcal{H}}_{\rm QE} = \hbar\omega_{eg} |e\rangle\langle e|, \tag{4.6}$$

$$\hat{\mathcal{H}}_{\rm int} = \hbar(f \hat{a}_2^\dagger \, |g\rangle \langle e| + f^* \hat{a}_2 \, |e\rangle \langle g|), \tag{4.7}$$

$$\hat{\mathcal{H}}_{\rm source} = i\hbar(\hat{a}_1^\dagger \varepsilon_{\rm s} e^{-i\omega t} - \textit{h.c.}) \tag{4.8}$$

$$\hat{\mathcal{H}}_{\rm pump} = i\hbar(|e\rangle \langle g| \, \varepsilon_{\rm p} e^{-i2\omega t} - \textit{h.c.}). \tag{4.9}$$

The total Hamiltonian of the system ($\hat{\mathcal{H}}$) consists of plasmonic mode energies ($\hat{\mathcal{H}}_0$); the energy of SHG process ($\hat{\mathcal{H}}_{\rm SHG}$); the energy of the QE with two discrete levels, ground and excited ($\hat{\mathcal{H}}_{\rm QE}$); the interaction energy between the $\hat{a}_2$-mode of the oscillator and the emitter ($\hat{\mathcal{H}}_{\rm int}$); the incident energy supplied by the source ($\hat{\mathcal{H}}_{\rm source}$); and the small driving source that pumps the QE ($\hat{\mathcal{H}}_{\rm pump}$).

In Eqs. (4.4)-(4.9), the double-resonance scheme supports two plasmon modes, $\hat{a}_1$ and $\hat{a}_2$, with resonance frequencies Ω_1 and Ω_2 respectively [13, 39]. The QE energy levels $|g\rangle\langle g|$ (ground) and $|e\rangle\langle e|$ (excited) are chosen such that the QE becomes a discrete object with a level spacing ω_{eg}. The QE is coupled to the higher energy plasmon mode, $\hat{a}_2$ of the gold MNS where the lower energy mode, $\hat{a}_1$, is excited with a source of frequency ω. The interaction strength between the $\hat{a}_2$-mode and QE is identified as f and the exciting strength of the source is defined by $\varepsilon_{\rm s}$. Under the illumination of the source $\varepsilon_{\rm s}e^{-i\omega t}$, the $\hat{a}_1$-mode of the MNS is activated to generate plasmon oscillations with resonance frequency Ω_1. Consequently, second harmonic polarization field at frequency 2ω is stimulated. The QE is pumped with a small source $\varepsilon_{\rm p}e^{-i2\omega t}$ with a frequency resonant to SH generated field. The generally complex structured information on electric and symmetry properties of the nonlinear MNS is collected in the second order susceptibility, $\chi^{(2)}$ [11].

The coupling of MNS-QE system allows to have control over SH response, and hence path interference scheme can be altered [102]. Driving the QE with a small source can be used to manipulate the nonlinear response of the system.

The use and control of quantum materials coupled with plasmonic or photonic structures lead the way to important applications such as all optical gates and switches, imaging with terahertz technologies, photonics based quantum information processing and generation of entangled photons [73, 102–111].

The equations of motion of the system is obtained through the Heisenberg relations,

$i\hbar\dot{\hat{a}} = [\hat{a}, \hat{H}]$ as follows,

$$\dot{\alpha}_1 = (-i\Omega_1 - \gamma_1)\alpha_1 - 2i\chi^{(2)}\alpha_1^*\alpha_2 + \varepsilon_{\rm s}e^{-i\omega t}, \tag{4.10}$$

$$\dot{\alpha}_2 = (-i\Omega_2 - \gamma_2)\alpha_2 - i\chi^{(2)}\alpha_1^2 - if\rho_{ge}, \tag{4.11}$$

$$\dot{\rho}_{ge} = (-i\omega_{eg} - \gamma_{eg})\rho_{ge} + (if^*\alpha_2 - \varepsilon_{\rm p}e^{-i2\omega t})(\rho_{ee} - \rho_{gg}), \tag{4.12}$$

$$\dot{\rho}_{ee} = -\gamma_{ee}\rho_{ee} + (if\alpha_2^* + \varepsilon_{\rm p}^*e^{i2\omega t})\rho_{ge} + (-if^*\alpha_2 + \varepsilon_{\rm p}e^{-i2\omega t})\rho_{ge}^*, \tag{4.13}$$

in which the decay rates for plasmonic oscillations are described as γ_1, γ_2 and the damping rates for the quantum states are γ_{ee}, $\gamma_{eg} = \gamma_{ee}/2$. The energy conservation yields to the constraint on the emitter modes as $\rho_{ee} + \rho_{gg} = 1$. The population inversion for the QE is defined as $y = \rho_{ee} - \rho_{gg}$.

In the long term limit, the plasmon modes and the quantum density matrix elements oscillate with the following frequencies; $\alpha_1(t) = \tilde{\alpha}_1 e^{-i\omega t}$, $\alpha_2(t) = \tilde{\alpha}_2 e^{-i2\omega t}$, $\rho_{\rm ge}(t) = \tilde{\rho}_{\rm ge}e^{-i2\omega t}$, $\rho_{\rm ee}(t) = \tilde{\rho}_{\rm ee}$. Using the solutions in Eqs. (4.10)-(4.13), the exponential terms are cancelled in each equation as a result of energy conservation. The steady-state equations can be written as,

$$[i(\Omega_1 - \omega) + \gamma_1]\tilde{\alpha}_1 = -2i\chi^{(2)}\tilde{\alpha}_1^*\tilde{\alpha}_2 + \varepsilon_{\rm s}, \tag{4.14}$$

$$[i(\Omega_2 - 2\omega) + \gamma_2]\tilde{\alpha}_2 = -i\chi^{(2)}\tilde{\alpha}_1^2 - if\tilde{\rho}_{\rm ge}, \tag{4.15}$$

$$[i(\omega_{eg} - 2\omega) + \gamma_{eg}]\tilde{\rho}_{\rm ge} = (if^*\tilde{\alpha}_2 - \varepsilon_{\rm p})(\tilde{\rho}_{\rm ee} - \tilde{\rho}_{\rm gg}), \tag{4.16}$$

$$\gamma_{\rm ee}\tilde{\rho}_{\rm ee} = (if\tilde{\alpha}_2^* + \varepsilon_{\rm p}^*)\tilde{\rho}_{\rm ge} + (-if^*\tilde{\alpha}_2 + \varepsilon_{\rm p})\tilde{\rho}_{\rm ge}^*. \tag{4.17}$$

Solving Eqs. (4.14)-(4.16) yields to an expression that provides information about the behaviour of the system in the long term limit,

$$\begin{aligned}\tilde{\alpha}_2 = &\frac{-i\chi^{(2)}}{[i(\Omega_2 - 2\omega) + \gamma_2] - \frac{|f|^2 y}{[i(\omega_{eg} - 2\omega) + \gamma_{eg}]}}\tilde{\alpha}_1^2 \\ &+ \frac{ify\varepsilon_{\rm p}}{[i(\omega_2 - 2\omega) + \gamma_2]\,[i(\omega_{eg} - 2\omega) + \gamma_{eg}] - |f^2|y}.\end{aligned} \tag{4.18}$$

The effects of path interference can be observed in Eq. (4.18). The nonlinear response of the system can be modified as a result of the QE coupling, represented by f. Furthermore, the effect of the pump strength $\varepsilon_{\rm p}$ that drives the QE can be observed.

The steady-state expressions for the plasmon and emitter modes are studied through the time evolution of Eqs. (4.10)-(4.13). It should be noted that no assumptions are

made during the numerical evaluations, the exact solutions are obtained for the analytical results. Eq. (4.18) is presented in order to provide an understanding on the enhancement and suppression phenomenon that occurs as a result of Fano coupling between MNS-QE [101]. Also, in this treatment the retardation effects are neglected and MNPs are considered as point objects with no spatial extent. It has been demonstrated that the simple treatment that is presented here, performs predictions of plasmonic behaviour well enough compared to the results of the three-dimensional simulations which utilizes the retardation effects [58, 60, 112, 113].

4.3 Nonclassicality Measure and Quantifying the Entanglement

A Gaussian state is a state which exhibit a form of Gaussian Wigner distribution. Complete information of a Gaussian state is harboured by the covariance (correlation) matrix which depends on the first and second statistical moments of the quadrature operators [114]. Without affecting the entanglement characteristics of the system, the first order variances can be set to zero [115]. Consequently, the covariance matrix for a Gaussian state can be written as,

$$V_{ij} = \frac{1}{2}\left\langle \hat{Y}_i\hat{Y}_j + \hat{Y}_j\hat{Y}_i \right\rangle - \left\langle \hat{Y}_i \right\rangle \left\langle \hat{Y}_j \right\rangle, \tag{4.19}$$

with implying the quadrature vector of the two-mode system as $\hat{Y} = [\hat{x}_1, \hat{p}_1, \hat{x}_2, \hat{p}_2]$. Here, the quadrature operators are defined as $\hat{x}_i = (\hat{a}_i^\dagger + \hat{a}_i)/\sqrt{2}$ and $\hat{p}_i = i(\hat{a}_i^\dagger - \hat{a}_i)/\sqrt{2}$.

Since it is obtained by noise variance and noise correlation measurements, the covariance matrix have entities which are real numbers. When multiplied with the frequency of the corresponding mode, $\hbar\omega$, the matrix elements gives the contribution term of the second moments to the free Hamiltonian of the system [114].

Considering a two-mode system, the covariance matrix becomes,

$$V = \begin{bmatrix} A & C \\ C^T & B \end{bmatrix}. \tag{4.20}$$

The 2×2 matrices *A*, *B* and *C* are given as,

$$A = \begin{bmatrix} \langle \hat{x}_1^2 \rangle - \langle \hat{x}_1 \rangle^2 & \langle \hat{x}_1 \hat{p}_1 + \hat{p}_1 \hat{x}_1 \rangle /2 - \langle \hat{x}_1 \rangle \langle \hat{p}_1 \rangle \\ \langle \hat{x}_1 \hat{p}_1 + \hat{p}_1 \hat{x}_1 \rangle /2 - \langle \hat{x}_1 \rangle \langle \hat{p}_1 \rangle & \langle \hat{p}_1^2 \rangle - \langle \hat{p}_1 \rangle^2 \end{bmatrix}, \tag{4.21}$$

$$B = \begin{bmatrix} \langle \hat{x}_2^2 \rangle - \langle \hat{x}_2 \rangle^2 & \langle \hat{x}_2 \hat{p}_2 + \hat{p}_2 \hat{x}_2 \rangle /2 - \langle \hat{x}_2 \rangle \langle \hat{p}_2 \rangle \\ \langle \hat{x}_2 \hat{p}_2 + \hat{p}_2 \hat{x}_2 \rangle /2 - \langle \hat{x}_2 \rangle \langle \hat{p}_2 \rangle & \langle \hat{p}_2^2 \rangle - \langle \hat{p}_2 \rangle^2 \end{bmatrix}, \tag{4.22}$$

$$C = \begin{bmatrix} \langle \hat{x}_1 \hat{x}_2 + \hat{x}_2 \hat{x}_1 \rangle /2 - \langle \hat{x}_1 \rangle \langle \hat{x}_2 \rangle & \langle \hat{x}_1 \hat{p}_2 + \hat{p}_2 \hat{x}_1 \rangle /2 - \langle \hat{x}_1 \rangle \langle \hat{p}_2 \rangle \\ \langle \hat{p}_1 \hat{x}_2 + \hat{x}_2 \hat{p}_1 \rangle /2 - \langle \hat{x}_2 \rangle \langle \hat{p}_1 \rangle & \langle \hat{p}_1 \hat{p}_2 + \hat{p}_2 \hat{p}_1 \rangle /2 - \langle \hat{p}_1 \rangle \langle \hat{p}_2 \rangle \end{bmatrix}. \tag{4.23}$$

Here, *C* gives the correlation noise. In terms of *A*, *B* and *C* matrices, the local invariants of the system are det(A), det(B) and det(C). Using the invariant quantity $\sigma(V)$ = det(A) + det(B) - 2det(C), the symplectic eigenvalues are found as,

$$\nu_{\pm} = \frac{1}{\sqrt{2}} \left(\sigma(V) \pm \left\{ [\sigma(V)]^2 - 4\text{det}(V) \right\}^{1/2} \right)^{1/2}. \tag{4.24}$$

4.3.1 Logarithmic Negativity

The separability condition for a partial transpose state implies that either one of the symplectic eigenvalues should be greater than $1/2$. Therefore, the presence of entanglement between the two-mode states is denoted by the condition $2\nu_- < 1$ since $\nu_- < \nu_+$. Therefore, $2\nu_-$ becomes an entanglement standard which gets smaller as the entanglement strength increases. For Gaussian states, the logarithmic negativity (log-neg),

$$E_N = \text{max}(0, -\text{log}(2\nu_-)), \tag{4.25}$$

is presented as an entanglement measure. As the symplectic eigenvalue gets smaller, E_N increases and eventually gives zero when $2\nu_- > 1$. This would imply that the entanglement is not present in the system at all. The maximum value of the entanglement at the output is calculated by maximizing the logarithmic negativity value.

Maximizing the logarithmic negativity $E_N(t, \phi)$ with respect to the beam splitter parameters, t and ϕ, points out to the maximum value of entanglement present in the system [116]. The maximum value of $E_N(t, \phi)$ defines the entanglement measure as $\mathcal{N}_{\text{SMNc}}$ [24].

4.3.2 Simon-Peres-Horodecki Criterion

Additional to the logarithmic negativity, there are other criteria to witness the entanglement for Gaussian states. Denoted by the expression,

$$\begin{aligned}\lambda_{\text{simon}} = \det(A)\det(B) + \left(\frac{1}{4} - |\det(C)|\right)^2 \\ - tr\left(AJCJBJC^TJ\right) \\ - \frac{1}{4}\left(\det(A) + \det(B)\right) < 0,\end{aligned} \tag{4.26}$$

the criterion derived in Ref. [100], the Simon-Peres-Horodecki (SPH) criterion is an entanglement witness not also for Gaussian states, but for non-Gaussian states too. Here, the J matrix is

$$J = \begin{bmatrix} 0 & 1 \\ -1 & 0 \end{bmatrix}. \tag{4.27}$$

The maximum value of $-\lambda_{\text{Simon}}$ is referred as η_{SMNc}, provides significant information about whether the entanglement is present in the two-mode state or not, indicating the nonclassicality of the input state [25, 100]. Unlike the logarithmic negativity SPH criterion is not presented as a measure that can quantify the entanglement. However, it is still a strong expression as it is formed in terms of the local invariants. In other words, λ_{Simon} is invariant under local rotations $\hat{a}_{1,2}(\phi_{1,2}) = e^{i\phi_{1,2}}\hat{a}_{1,2}$. The significance of the SPH criterion lies in the fact that it can be utilized to witness the entanglement of quantum states other than Gaussian states [24].

4.4 Beam Splitter Transformations

A beam splitter, one of the devices that can act as an entangler, can be used to determine the nonclassicality of the input single-mode field once the quantity of entanglement strength at the output is validated. Mixing of a single mode field $\hat{a}$ with a coherent state such as the vacuum, results into two output modes, $\hat{a}_1$ and $\hat{a}_2$, at the output of a beam splitter. In other means, quantifying the entanglement at the output by using the measure $\mathcal{N}_{\text{SMNc}}$, enables the determination of single mode nonclassicality (SMNc) amount of the input Gaussian state. Furthermore, λ_{Simon} can be used as

a single-mode nonclassicality witness, by determining whether the two-mode states at the output are entangled or not. In order to analyze the entanglement properties of the system, the beam splitter transformations can be utilized [25].

To determine the nonclassicality of a single-mode input state, the following procedure is followed:

(i) By using the beam splitter transformations, the variance terms of the two output modes, such as $\langle \hat{a}_{1,2}^2 \rangle$ and $\langle \hat{a}_1 \hat{a}_2 \rangle$ can be evaluated in terms of $\langle \hat{a}^2 \rangle$ and $\langle \hat{a}^\dagger \hat{a} \rangle$. Hence, both the nonclassicality measure $\mathcal{N}_{\mathrm{SMNc}}$ and the nonclassicality condition λ_{Simon} can be obtained in terms of the single-mode variances $\langle \hat{a}^2 \rangle$ and $\langle \hat{a}^\dagger \hat{a} \rangle$ [24].

(ii) The elements of the covariance matrix can be obtained in terms of $\langle \hat{a}^2 \rangle$, $\langle \hat{a}^\dagger \hat{a} \rangle$ and the beam splitter parameters, t, r and ϕ.

(iii) The nonclassicality measure $\mathcal{N}_{\mathrm{SMNc}}$ can be obtained by maximizing $E_N(t, \phi)$ with respect to t = [0,1] and ϕ = [0,2π] where $r^2 + t^2 = 1$. Similarly, the nonclassicality witness η_{SMNc} can be attained by chasing the smallest value of $\lambda_{\mathrm{Simon}}(t, \phi)$.

When the single-mode state $|\psi_a\rangle = \sum_{n=0}^{\infty} c_n |n\rangle$ mixes with the vacuum $|0\rangle$ at the input of a beam splitter, the initial state is denoted as $|\psi_a\rangle_1 \otimes |0\rangle_2$. After the transformation, two-mode output states $|\psi_{12}\rangle$ are produced at the output of a beam splitter, shown in Fig. 4.1 [25, 26]. The beam splitter operator with the expression

$$\hat{B}(\xi) = e^{\xi \hat{a}_2^\dagger \hat{a}_1 - \xi^* \hat{a}_1^\dagger \hat{a}_2} \tag{4.28}$$

generates transformed states as follows,

$$\hat{a}_1(\xi) = \hat{B}^\dagger(\xi) \hat{a}_1 \hat{B}(\xi) = t e^{i\phi} \hat{a}_1 + r \hat{a}_2, \tag{4.29}$$

$$\hat{a}_2(\xi) = \hat{B}^\dagger(\xi) \hat{a}_2 \hat{B}(\xi) = -r \hat{a}_1 + t e^{-i\phi} \hat{a}_2. \tag{4.30}$$

Here, $\hat{a}_1$ and $\hat{a}_2$ are the annihilation operators for the first and second output states. The two output modes can be written as $|\psi_{12}\rangle = f\left(\mu_1 \hat{a}_1^\dagger + \mu_2 \hat{a}_2^\dagger\right) |0\rangle_1 \otimes |0\rangle_2$ where $f(\hat{a}^\dagger) = \sum_{n=0}^{\infty} d_n (\hat{a}^\dagger)^n$ is the expansion of the input mode as

$$|\psi_a\rangle = \left(\sum_{n=0}^{\infty} d_n (\hat{a}^\dagger)^2 \right) |0\rangle_a. \tag{4.31}$$

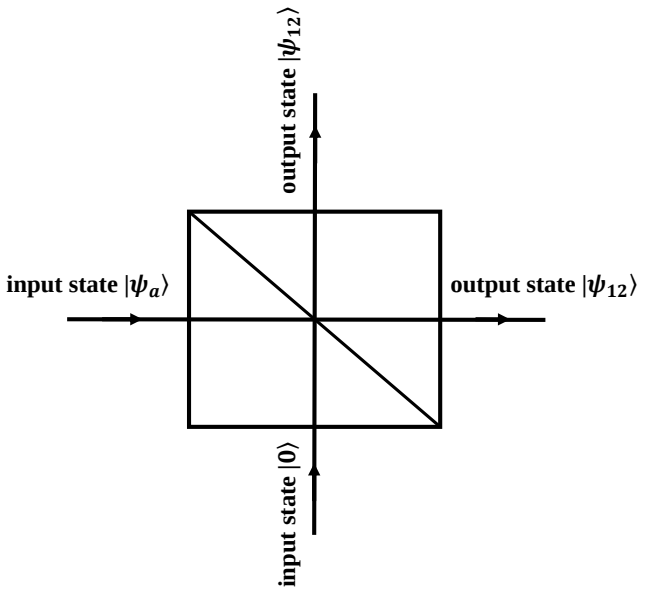

Figure 4.1: The schematic representation of the beam splitter operation. The input states are $|\psi_a\rangle$ and vacuum $|0\rangle$, composing the initial state as $|\psi_a\rangle_1 \otimes |0\rangle_2$. The two-mode output state after the transformation is $|\psi_{12}\rangle = f\left(\mu_1 \hat{a}_1^\dagger + \mu_2 \hat{a}_2^\dagger\right)|0\rangle_1 \otimes |0\rangle_2$.

In order to obtain the elements of the covariance matrix, one should obtain the expectation values in the entities of Eqs. (4.21) - (4.23). Since the quadrature operators are defined as $\hat{x}_i = (\hat{a}_i^\dagger + \hat{a}_i)/\sqrt{2}$ and $\hat{p}_i = i(\hat{a}_i^\dagger - \hat{a}_i)/\sqrt{2}$, all the entities in Eqs. (4.21)-(4.23) depend on the expectation values of two-mode output states, characterized by the annihilation (creation) operators $\hat{a}_1$ ($\hat{a}_1^\dagger$) and $\hat{a}_2$ ($\hat{a}_2^\dagger$). Applying the beam splitting operations allows to obtain the two-mode variances in terms of the single-mode input quantities.

By utilizing the beam splitter operations, the two-mode variances can be evaluated such as $\left\langle \hat{a}_{1,2}^2 \right\rangle$ and $\langle \hat{a}_1 \hat{a}_2 \rangle$ in terms of $\langle \hat{a}^2 \rangle$ and $\left\langle \hat{a}^\dagger \hat{a} \right\rangle$.

For instance, expectation value of $\langle \hat{a}_1 \hat{a}_2 \rangle$ can be obtained by applying beam splitter transformations to the initial state. In the Heisenberg picture, it can be written as

$$\langle \hat{a}_1 \hat{a}_2 \rangle = {}_2\langle 0| \otimes {}_1\langle \psi_a| \left(\hat{B}^\dagger(\xi) \hat{a}_1 \hat{a}_2 \hat{B}(\xi)\right) |\psi_a\rangle_1 \otimes |0\rangle_2 . \tag{4.32}$$

Applying beam splitter operation in Eq. (4.28), the expectation value becomes,

$$\langle \hat{a}_1 \hat{a}_2 \rangle = {}_2\langle 0| \otimes {}_1\langle \psi_a| \left(te^{i\phi}\hat{a}_1 + r\hat{a}_2\right)\left(-r\hat{a}_1 + te^{-i\phi}\hat{a}_2\right)|\psi_a\rangle_1 \otimes |0\rangle_2 . \tag{4.33}$$

In Eq. (4.33), all the terms vanish except the one including $\hat{a}_1^2$ which eventually becomes ${}_1\langle\psi_a|\,\hat{a}_1^2\,|\psi_a\rangle_1 = \langle\psi_a|\,\hat{a}^2\,|\psi_a\rangle = \langle\hat{a}^2\rangle$. Then the expectation value is written as,

$$\langle\hat{a}_1\hat{a}_2\rangle = -tre^{i\phi}\left\langle\hat{a}^2\right\rangle. \tag{4.34}$$

As an example, the $A(1, 1)$ entry of the Eq. (4.21) can be written as $\langle\hat{x}_1^2\rangle - \langle\hat{x}_1\rangle^2 = \frac{1}{2}\left[\langle\hat{a}_1^{\dagger 2}\rangle + \langle\hat{a}_1^2\rangle\right] - \frac{1}{2}\left[\langle\hat{a}_1^{\dagger}\rangle^2 + \langle\hat{a}_1\rangle^2\right]$. By performing similar calculations, the covariance matrix elements, A, B and C matrices, are obtained in terms of the input nonclassical state, $\hat{a}$, as

$$A = \begin{bmatrix} t^2[cos(\theta+2\phi)v_a + n_a] + \frac{1}{2} & t^2 v_a sin(\theta+2\phi) \\ t^2 v_a sin(\theta+2\phi) & t^2[-cos(\theta+2\phi)v_a + n_a] + \frac{1}{2} \end{bmatrix}, \tag{4.35}$$

$$B = \begin{bmatrix} r^2(cos\theta v_a + n_a) + \frac{1}{2} & r^2 v_a sin\theta \\ r^2 v_a sin\theta & r^2(-cos\theta v_a + n_a) + \frac{1}{2} \end{bmatrix}, \tag{4.36}$$

$$C = tr\begin{bmatrix} -[cos(\theta+\phi)v_a + cos\phi n_a] & [-sin(\theta+\phi)v_a + sin\phi n_a] \\ -[sin(\theta+\phi)v_a + sin\phi n_a] & [cos(\theta+\phi)v_a - cos\phi n_a] \end{bmatrix}. \tag{4.37}$$

Here, $\left\langle\hat{a}^{\dagger}\hat{a}\right\rangle = n_a$ and $\langle\hat{a}^2\rangle = v_a e^{i\theta}$ where v_a is a real and positive parameter.

The beam splitter operation which is denoted in Eq. (4.28) is a linear transformation which produces null expectation values for the quadrature operators, $\langle x_i\rangle$ = $\langle p_i\rangle$ = 0, or $\langle\hat{a}_i\rangle$ = 0 in general. Hence, the noise features deal with the entanglement properties in a system, are not affected by this linear transformations, where $\hat{a} = \langle\hat{a}\rangle + \delta\hat{a}$. In other means, n_a and v_a parameters become,

$$v_a e^{i\theta} = \left\langle\hat{a}^2\right\rangle = \left\langle(\delta\hat{a})^2\right\rangle, \tag{4.38}$$

$$n_a = \left\langle\hat{a}^{\dagger}\hat{a}\right\rangle = \left\langle(\delta\hat{a})^{\dagger}(\delta\hat{a})\right\rangle. \tag{4.39}$$

Here $\delta\hat{a} = \hat{a} - \langle\hat{a}\rangle$ is the operator of the input nonclassical state with a zero expectation itself, i.e., $\langle\delta\hat{a}\rangle = 0$ [117].

Similarly, the variances of the two-mode output states, $\hat{a}_i - \delta\hat{a}_i = \langle\hat{a}_i\rangle$, are set to zero by the linear transformation, $\langle\hat{a}_i\rangle = 0$. The noise features are not changed with this transformation and hence, the nonclassicality measure is unaffected.

With this treatment, the nonclassicality measure $\mathcal{N}_{\mathrm{SMNc}}$ and the nonclassicality condition η_{SMNc} can be written with respect to the variances of single-mode state. By

acknowledging $\langle \hat{a}^2 \rangle$ and $\langle \hat{a}^\dagger \hat{a} \rangle$, the nonclassicality of a single-mode state can be calculated and the entanglement features at the beam splitter output can be quantified.

4.5 Nonclassicality Analysis of a Plasmonic Second Harmonic Conversion

The coupled system of a doubly resonant MNS with a QE, described in Section 4.2, can be examined through its ability to produce nonclassical second harmonic response. The formulation presented in Section 4.3, can be applied to the MNS-QE system to witness and quantify the possible entanglement of the second harmonic output.

4.5.1 Plasmonic Mode Fluctuations in the Steady-State Limit

The input (output) field $\hat{a}_1$ ($\hat{a}_2$), that is the lower (higher) energy mode of the MNS, has the steady-state forms as $\hat{a}_{1,\mathrm{s}} \to \alpha_1 + \delta\hat{a}_1$ and $\hat{a}_{2,\mathrm{s}} \to \alpha_2 + \delta\hat{a}_2$. Therefore, in the steady-state limit the fluctuations in the plasmon modes can be introduced as

$$\delta\dot{\hat{a}}_1 = -\beta_1 \delta\hat{a}_1 - 2i\chi^{(2)}\alpha_1^* \delta\hat{a}_2 - 2i\chi^{(2)}\alpha_2 \delta\hat{a}_1^\dagger + g_1 \hat{a}_{1,\mathrm{in}}(t) \tag{4.40}$$

$$\delta\dot{\hat{a}}_1^\dagger = -\beta_1^* \delta\hat{a}_1^\dagger + 2i\chi^{(2)*}\alpha_1 \delta\hat{a}_2^\dagger + 2i\chi^{(2)*}\alpha_2^* \delta\hat{a}_1 + g_1^* \hat{a}_{1,\mathrm{in}}^\dagger(t) \tag{4.41}$$

$$\delta\dot{\hat{a}}_2 = -\beta_2 \delta\hat{a}_2 - i\chi^{(2)} \delta\hat{a}_1^2 - 2i\chi^{(2)}\alpha_1 \delta\hat{a}_1 + g_2 \hat{a}_{2,\mathrm{in}}(t) \tag{4.42}$$

$$\delta\dot{\hat{a}}_2^\dagger = -\beta_2^* \delta\hat{a}_2^\dagger + i\chi^{(2)*} \delta\hat{a}_1^{\dagger 2} + 2i\chi^{(2)*}\alpha_1^* \delta\hat{a}_1^\dagger + g_2^* \hat{a}_{2,\mathrm{in}}^\dagger(t) \tag{4.43}$$

The fluctuations in the annihilation and creation operators of the plasmon modes can be used to determine the quadrature phase operators as $\delta x_i = 1/\sqrt{2}(\delta\hat{a}_i^\dagger + \delta\hat{a}_i)$ and $\delta p_i = i/\sqrt{2}(\delta\hat{a}_i^\dagger - \delta\hat{a}_i)$. The noise properties of the system are analyzed through the Langevin equations for the quantum fluctuations,

$$\delta\dot{\hat{x}}_1 = -\beta_{1\mathrm{R}}\delta\hat{x}_1 + \beta_{1\mathrm{I}}\delta\hat{p}_1 + \mu_{1\mathrm{R}}\delta\hat{p}_2 - \mu_{1\mathrm{I}}\delta\hat{x}_2 - \mu_{2\mathrm{R}}\delta\hat{p}_1 + \mu_{2\mathrm{I}}\delta\hat{x}_1 + g_1\hat{X}_{1,\mathrm{in}}(t) \tag{4.44}$$

$$\delta\dot{\hat{p}}_1 = -\beta_{1\mathrm{R}}\delta\hat{p}_1 - \beta_{1\mathrm{I}}\delta\hat{x}_1 - \mu_{1\mathrm{R}}\delta\hat{x}_2 - \mu_{1\mathrm{I}}\delta\hat{p}_2 - \mu_{2\mathrm{R}}\delta\hat{x}_1 - \mu_{2\mathrm{I}}\delta\hat{p}_1 + g_1\hat{P}_{1,\mathrm{in}}(t) \tag{4.45}$$

$$\delta\dot{\hat{x}}_2 = -\beta_{2\mathrm{R}}\delta\hat{x}_2 + \beta_{2\mathrm{I}}\delta\hat{p}_2 + \mu_{1\mathrm{R}}\delta\hat{p}_1 + \mu_{1\mathrm{I}}\delta\hat{x}_1 + g_2\hat{X}_{2,\mathrm{in}}(t) \tag{4.46}$$

$$\delta\dot{\hat{p}}_2 = -\beta_{2\mathrm{R}}\delta\hat{p}_2 - \beta_{2\mathrm{I}}\delta\hat{x}_2 - \mu_{1\mathrm{R}}\delta\hat{x}_1 + \mu_{1\mathrm{I}}\delta\hat{p}_1 + g_2\hat{P}_{2,\mathrm{in}}(t). \tag{4.47}$$

Here, the second-order noise terms such as $\delta\hat{a}_1\delta\hat{a}_2$ are ignored as they are negligibly small compared to the other quantities. The parameters are defined as $\beta_1 = [i(\Omega_1 - \omega) + \gamma_1]$ and $\beta_2 = [i(\Omega_2 - 2\omega) + \gamma_2]$ with real ($\beta_{1\mathrm{R}}$, $\beta_{2\mathrm{R}}$) and imaginary ($\beta_{1\mathrm{I}}$, $\beta_{2\mathrm{I}}$) parts. μ_1 and μ_2 are written in terms of plasmon fields and second order susceptibility as $\mu_1 = 2\chi^{(2)}\alpha_1$ and $\mu_1 = 2\chi^{(2)}\alpha_2$.

Furthermore, the noise fluctuations form a 4×4 matrix denoted as,

$$\underset{\approx}{A} = \begin{bmatrix} -\beta_{1\mathrm{R}} + \mu_{2\mathrm{I}} & \beta_{1\mathrm{I}} - \mu_{2\mathrm{R}} & -\mu_{1\mathrm{I}} & \mu_{1\mathrm{R}} \\ -\beta_{1\mathrm{I}} - \mu_{2\mathrm{R}} & -\beta_{1\mathrm{R}} - \mu_{2\mathrm{I}} & -\mu_{1\mathrm{R}} & -\mu_{1\mathrm{I}} \\ \mu_{1\mathrm{I}} & \mu_{1\mathrm{R}} & -\beta_{2\mathrm{R}} & \beta_{2\mathrm{I}} \\ -\mu_{1\mathrm{R}} & \mu_{1\mathrm{I}} & -\beta_{2\mathrm{I}} & -\beta_{2\mathrm{R}} \end{bmatrix}. \tag{4.48}$$

The $\underset{\approx}{A}$ matrix satisfy the Langevin equation,

$$\dot{\underset{\sim}{\hat{u}}} = \underset{\approx}{A}.\underset{\sim}{\hat{u}} + \underset{\sim}{\hat{u}}_{\mathrm{in}}, \tag{4.49}$$

where the eigenvectors $\underset{\sim}{\hat{u}}(0)$ and $\underset{\sim}{\hat{u}}_{\mathrm{in}}(0)$ are

$$\underset{\sim}{u}(0) = \begin{bmatrix} \delta\hat{x}_1 \\ \delta\hat{p}_1 \\ \delta\hat{x}_2 \\ \delta\hat{p}_2 \end{bmatrix}, \quad \underset{\sim}{u}_{\mathrm{in}}(0) = \begin{bmatrix} g_1\delta\hat{x}_{1,\mathrm{in}} \\ g_1\delta\hat{p}_{1,\mathrm{in}} \\ g_2\delta\hat{x}_{2,\mathrm{in}} \\ g_2\delta\hat{p}_{2,\mathrm{in}} \end{bmatrix}. \tag{4.50}$$

The coupling strength of plasmon modes to the vacuum are denoted as g_i which satisfies the relation with the damping rates of the oscillations, $\gamma_i\pi D(\omega_i)g_i^2$. Here, $D(\omega_i)$ are the density of states at the corresponding frequencies ω_i.

A close examination of Eq. (4.48) reveals that A matrix can be evaluated numerically, since β_1 and β_2 are complex numbers that can exactly be evaluated and the values of plasmon modes α_1 and α_2 are used in their steady-state form. Hence, there is no time dependence of the matrix A.

The input vacuum noise which linearizes the noise operators are written as $g_i\delta\hat{a}_{i,in}(t) = -i\sum_k e^{-i\omega_k t}\hat{b}_k(0)$ where $\hat{b}_k(0)$ denote the vacuum operators. Therefore, the general solution for $\hat{u}(t)$ is,

$$\underset{\sim}{\hat{u}}(t) = e^{\underset{\approx}{A}t}\underset{\sim}{\hat{u}}(0) + \int_0^t dt' e^{\underset{\approx}{A}t'}\underset{\sim}{\hat{u}}_{in}(t - t'), \tag{4.51}$$

where the exponential term $e^{\underset{\approx}{A}t}$ is defined as another matrix labeled as $\underset{\approx}{M}(t)$.

By using the properties of matrices in linear algebra, the Langevin equation in Eq. (4.49) can be interpreted in a more simple and analyzable form. In order to achieve this, the following theorem is used; A matrix S is diagonalizable if there exists an invertible matrix P and a diagonal matrix D, that satisfies the relation $P^{-1}SP = D$. The exponential form of a diagonal matrix is obtained by taking the exponential value of all the matrix elements. So, considering the matrix S that obeys the relation $S = PDP^{-1}$ where D is diagonal, the exponential of S can be found as $e^S = Pe^D P^{-1}$.

Therefore if the $\underset{\approx}{A}$ matrix in Eq. (4.48) can be written as $\underset{\approx}{A} = P^{-1}\underset{\approx}{D}P$, then $e^{\underset{\approx}{A}t'} = Pe^{\underset{\approx}{D}t'}Q$, where $P^{-1} = Q$. So, $\underset{\approx}{A}$ is said to be a diagonal matrix with the following exponential operation,

$$\underset{\approx}{D} = \begin{bmatrix} \lambda_1 & & \\ & \ddots & \\ & & \lambda_4 \end{bmatrix} \rightarrow \quad e^{\underset{\approx}{D}t} = \begin{bmatrix} e^{\lambda_1 t} & & \\ & \ddots & \\ & & e^{\lambda_4 t} \end{bmatrix}. \tag{4.52}$$

(4.53)

As a result, $\underset{\approx}{M}(t)$ can be expressed as,

$$\underset{\approx}{M}(t) = e^{\underset{\approx}{A}t} = \begin{bmatrix} P_{11} & P_{12} & P_{13} & P_{14} \\ P_{21} & P_{22} & P_{23} & P_{24} \\ P_{31} & P_{32} & P_{33} & P_{34} \\ P_{41} & P_{42} & P_{43} & P_{44} \end{bmatrix} \quad \times \quad \begin{bmatrix} Q_{11}e^{\lambda_1 t} & Q_{12}e^{\lambda_1 t} & Q_{13}e^{\lambda_1 t} & Q_{14}e^{\lambda_1 t} \\ Q_{21}e^{\lambda_2 t} & Q_{22}e^{\lambda_2 t} & Q_{23}e^{\lambda_2 t} & Q_{24}e^{\lambda_2 t} \\ Q_{31}e^{\lambda_3 t} & Q_{32}e^{\lambda_3 t} & Q_{33}e^{\lambda_3 t} & Q_{34}e^{\lambda_1 t} \\ Q_{41}e^{\lambda_4 t} & Q_{42}e^{\lambda_4 t} & Q_{43}e^{\lambda_4 t} & Q_{44}e^{\lambda_1 t} \end{bmatrix} \tag{4.54}$$

With this general expression, the elements of $\underset{\approx}{M}(t)$ can be written explicitly. For example, the first element of the matrix becomes

$$M_{11}(t) = P_{11}Q_{11}e^{\lambda_1 t} + P_{12}Q_{21}e^{\lambda_2 t} + P_{13}Q_{31}e^{\lambda_3 t} + P_{14}Q_{41}e^{\lambda_4 t}. \tag{4.55}$$

To generalize, the $\underset{\approx}{M}(t)$ matrix elements become

$$M_{mn}(t) = \sum_{k=1}^{4} P_{mk}Q_{kn}e^{\lambda_k t}. \tag{4.56}$$

For instance, if one sets the parameter m=1 and vary n from 1 to 4, the first row of

Eq. (4.54) can be obtained as,

$$M_{1i}(t) = \sum_{l=1}^{4} \sum_{i=1}^{4} P_{1l} Q_{li} e^{\lambda_l t}. \tag{4.57}$$

Furthermore, the eigenvector expression $\hat{\underset{\sim}{u}}(t)$ in Eq. (4.51) becomes

$$\hat{\underset{\sim}{u}}(t) = \underset{\approx}{M}(t)\hat{\underset{\sim}{u}}(0) + \int_0^t dt^{'} \underset{\approx}{M}(t^{'})\hat{\underset{\sim}{u}}_{in}(t - t^{'}), \tag{4.58}$$

where in the steady-state limit $t \to \infty$, $\hat{\underset{\sim}{u}}(0) \sim 0$. Then Eq. (4.58) can be written as

$$\hat{\underset{\sim}{u}}(t) = \int_0^t dt^{'} \underset{\approx}{M}(t^{'})\hat{\underset{\sim}{u}}_{in}(t - t^{'}). \tag{4.59}$$

4.5.2 Expectation Values of Input Plasmonic Mode Fluctuations

The noise operators of the plasmonic modes $\hat{a}_1$ and $\hat{a}_2$ in the form of Eq. (4.48) satisfies the Langevin equation in Eq. (4.49). In the steady-state limit, the solution for the eigenvectors in the form of Eq. (4.59) can be used to calculate the expectation values of the input plasmonic mode, $\langle \delta\hat{a}_1^2 \rangle$ and $\langle \delta\hat{a}_1^{\dagger} \delta\hat{a}_1 \rangle$.

$\langle \delta\hat{a}_1^2 \rangle$ ***Calculations***

In the form of quadrature operation fluctuations, $\langle \delta\hat{a}_1^2 \rangle$ is expressed as,

$$\begin{aligned} \left\langle \delta\hat{a}_1(t)\delta\hat{a}_1(t^{'}) \right\rangle = \frac{1}{2} \Big[&\left\langle \delta\hat{x}_1(t)\delta\hat{x}_1(t^{'}) \right\rangle - \left\langle \delta\hat{p}_1(t)\delta\hat{p}_1(t^{'}) \right\rangle \\ &+ i \left\langle \delta\hat{x}_1(t)\delta\hat{p}_1(t^{'}) \right\rangle + i \left\langle \delta\hat{p}_1(t)\delta\hat{x}_1(t^{'}) \right\rangle \Big]. \end{aligned} \tag{4.60}$$

Since $\delta\hat{x}_i(t)$ and $\delta\hat{p}_i(t)$ are the elements of $\hat{\underset{\sim}{u}}(t)$ in Eq. (4.50), they can be written by using the solution in the form of Eq. (4.59) as,

$$\delta\hat{x}_1(t) = \int_0^t dt^{'} \sum_{l=1}^{4} \underset{\approx}{M}_{1l_1}(t^{'})\hat{\underset{\sim}{u}}_{in,l_1}(t - t^{'}) \tag{4.61}$$

$$\delta\hat{p}_1(t) = \int_0^t dt^{'} \sum_{l=1}^{4} \underset{\approx}{M}_{2l_2}(t^{'})\hat{\underset{\sim}{u}}_{in,l_2}(t - t^{'}). \tag{4.62}$$

Therefore Eq. (4.60) can be calculated bu utilizing Eqs. (4.61) and (4.62). As an example, the calculation of the first term in Eq. (4.60) will be shown in detail. After

performing the transformation $t^{''} = t - t^{'}$ into Eqs. (4.61) and (4.62), one gets

$$\langle \delta\hat{x}_1(t)\delta\hat{x}_1(t^{'})\rangle = \sum_{l_1,l_2=1}^{4} \int_0^t ds \int_0^{t^{'}} ds^{'} \underset{\approx}{M}_{1l_1}(t-s)\underset{\approx}{M}_{1l_2}(t^{'}-s^{'})\langle \hat{\underset{\sim}{u}}_{in,l_1}(s)\hat{\underset{\sim}{u}}_{in,l_2}(s^{'})\rangle. \tag{4.63}$$

The expectation value $\langle \hat{\underset{\sim}{u}}_{in,l_1}(s)\hat{\underset{\sim}{u}}_{in,l_2}(s^{'})\rangle$ can be defined in the form $\Upsilon_{l_1,l_2}\delta(s-s^{'})$, shaping Eq. (4.63) into a simpler form as,

$$\langle \delta\hat{x}_1(t)\delta\hat{x}_1(t^{'})\rangle = \sum_{l_1,l_2=1}^{4} \Upsilon_{l_1l_2} \int_0^t ds \underset{\approx}{M}_{1l_1}(t-s)\underset{\approx}{M}_{1l_2}(t^{'}-s). \tag{4.64}$$

Eq. (4.64) is the simplest form of the first term of Eq. (4.60). The same treatment can be applied to the rest of the terms. Additionally, Eq. (4.57) is inserted to obtain the following expression for the expectation value $\langle \delta\hat{a}_1^2\rangle$,

$$\begin{aligned}\langle \delta\hat{a}_1(t)\delta\hat{a}_1(t^{'})\rangle = \frac{1}{2}\sum_{i,j}^{4}\Upsilon_{ij}\sum_{l_1,l_2}^{4}\int_0^t ds\, e^{(\lambda_{l_1}+\lambda_{l_2})(t-s)}\,[P_{1l_1}Q_{l_1i}P_{1l_2}Q_{l_2j} \\ -\, P_{2l_1}Q_{l_1i}P_{2l_2}Q_{l_2j} + iP_{1l_1}Q_{l_1i}P_{2l_2}Q_{l_2j} + iP_{2l_1}Q_{l_1i}P_{1l_2}Q_{l_2j}]\,.\end{aligned} \tag{4.65}$$

The integral term $\int_0^t ds\ e^{(\lambda_{l_1}+\lambda_{l_2})(t-s)}$ can easily be computed to obtain the result $1/(\lambda_{l_1}+\lambda_{l_2})$. Finally, Eq. (4.65) takes the form

$$\begin{aligned}\langle \delta\hat{a}_1(t)\delta\hat{a}_1(t^{'})\rangle = \frac{1}{2}\sum_{i,j}^{4}\Upsilon_{ij}\sum_{l_1,l_2}^{4}\frac{1}{\lambda_{l_1}+\lambda_{l_2}}\,[P_{1l_1}Q_{l_1i}P_{1l_2}Q_{l_2j} \\ -\, P_{2l_1}Q_{l_1i}P_{2l_2}Q_{l_2j} + iP_{1l_1}Q_{l_1i}P_{2l_2}Q_{l_2j} + iP_{2l_1}Q_{l_1i}P_{1l_2}Q_{l_2j}]\,.\end{aligned} \tag{4.66}$$

In Eq. (4.66), the matrix elements P_{mk} and Q_{kn} can be evaluated numerically. Therefore, in order to obtain the numerical value for the expectation value of the initial plasmon mode fluctuations, $\Upsilon_{ij} = \langle \hat{u}_{in,i}(t)\hat{u}_{in,j}(t^{'})\rangle$ should also be evaluated.

Υ_{ij} *Calculations*

The first element of Υ_{ij} matrix can be written as follows,

$$\begin{aligned}\Upsilon_{11} &= \langle \hat{u}_{in,1}(t)\hat{u}_{in,1}(t^{'})\rangle = g_1^2\langle \hat{x}_{in,1}(t)\hat{x}_{in,1}(t^{'})\rangle \\ &= \frac{g_1^2}{2}\langle(\hat{a}_{1,in}^{\dagger}(t)+\hat{a}_{1,in}(t))(\hat{a}_{1,in}^{\dagger}(t^{'})+\hat{a}_{1,in}(t^{'}))\rangle\end{aligned} \tag{4.67}$$

Considering the explicit form, only the term $\langle \hat{a}^{\dagger}_{1,in}(t)\hat{a}^{\dagger}_{1,in}(t^{'})\rangle$ becomes nonzero. Written in terms of the density of states $D(\omega_k)$, Υ_{11} has the shape

$$\Upsilon_{11} = g_1^2 \pi D(\omega_k)\delta(t-t^{'}) \tag{4.68}$$

where $g_1^2\pi D(\omega_k)$ is defined as Γ_k. The parameter Γ_k corresponds to the damping rate of the plasmon mode coupled with vacuum and can be approximated around 10^9 Hz. The rest of the elements of Υ_{ij} are calculated in a similar manner. Finally, Υ_{ij} is written in terms of a 4×4 matrix as

$$\Upsilon_{ij} = \begin{bmatrix} g_1^2 & g_1^2 & 0 & 0 \\ -ig_1^2 & g_1^2 & 0 & 0 \\ 0 & 0 & g_2^2 & ig_2^2 \\ 0 & 0 & -ig_2^2 & g_2^2 \end{bmatrix} \pi D(\omega_k)\delta(t-t^{'}). \tag{4.69}$$

Utilizing Eq. (4.66) with the matrix in Eq. (4.69), allows one to calculate numerically the value of expectation value of $\langle \delta\hat{a}_1(t)\delta\hat{a}_1(t^{'})\rangle$.

$\langle \delta\hat{a}_1^{\dagger}\delta\hat{a}_1\rangle$ ***Calculations***

Similar to the above treatment, the expectation value $\langle \delta\hat{a}_1^{\dagger}\delta\hat{a}_1\rangle$ can also be evaluated.

$$\begin{aligned}\left\langle \delta\hat{a}_1^{\dagger}(t)\delta\hat{a}_1(t^{'})\right\rangle = \frac{1}{2}\Big[&\left\langle \delta\hat{x}_1(t)\delta\hat{x}_1(t^{'})\right\rangle + \left\langle \delta\hat{p}_1(t)\delta\hat{p}_1(t^{'})\right\rangle \\ &+ i\left\langle \delta\hat{x}_1(t)\delta\hat{p}_1(t^{'})\right\rangle - i\left\langle \delta\hat{p}_1(t)\delta\hat{x}_1(t^{'})\right\rangle\Big].\end{aligned} \tag{4.70}$$

All of the 4 terms in the Eq. (4.70) are the same with Eq. (4.60) except their coefficients. Hence, the quick examination of Eq. (4.70) yields into the result,

$$\begin{aligned}\langle \delta\hat{a}_1(t)\delta\hat{a}_1(t^{'})\rangle = \frac{1}{2}\sum_{i,j}^{4}\Upsilon_{ij}\sum_{l_1,l_2}^{4}\frac{1}{\lambda_{l_1}+\lambda_{l_2}}\big[&P_{1l_1}Q_{l_1i}P_{1l_2}Q_{l_2j} \\ &+ iP_{1l_1}Q_{l_1i}P_{2l_2}Q_{l_2j} - iP_{2l_1}Q_{l_1i}P_{1l_2}Q_{l_2j} + P_{2l_1}Q_{l_1i}P_{2l_2}Q_{l_2j}\big].\end{aligned} \tag{4.71}$$

4.6 Results

The expressions in Eqs. (4.66) and (4.71) are calculated in order to examine the entanglement features of the system described in Section 4.2. The main aim is to understand whether the Fano mechanism can be controlled by driving the QE with a

pump source. In order to realize if this is possible, the nonclassicality of the plasmon oscillation modes are examined. If the nonclassicality of the plasmon modes increases as the second harmonic signal is enhanced, then it can be concluded that the presented enhancement occur as a result of the path interference. In other words, the direct pumping of the QE with the source can not produce entangled states. The nonclassicality of the plasmonic mode can only be increased if the response is altered by the nonlinear Fano mechanism.

Applying a pump source on the QE alters the path interference effects. By using the beam splitter transformation approach, the plasmonic system can be examined in terms of its entanglement features. The nonclassicality measure $\mathcal{N}_{\mathrm{SMNc}}$ is denoted as the maximum value of logarithmic negativity $E_N(\mathrm{t}, \phi)$. Furthermore, the nonclassicality criterion η_{SMNc} provides a further witness whether the entanglement is present in the system or not.

By applying the pump source to the QE, the response of the SH generated mode can be tuned. In Fig. (4.2) (a), the enhancement factor in the second harmonic converted plasmon mode is presented with respect to the QE level spacing values. The enhancement factor is calculated with and without the presence of QE interaction according to

$$EF = \frac{|\alpha_2(f \neq 0)|^2}{|\alpha_2(f = 0)|^2}. \tag{4.72}$$

Along with the enhancement factor, nonclassicality measure $\mathcal{N}_{\mathrm{SMNc}}$ and nonclassicality witness η_{SMNc} are shown. All the given parameters are expressed in proportion with the incident pump field, ω. The lower energy mode of the MNP, $\Omega_2 = 1.9\omega$ is slightly off-resonant with the second converted frequency. The pumping strength of the source that drives the $\hat{a}$-mode is denoted by $\varepsilon_{\mathrm{s}} = 10^{-2}\omega$, and the second order susceptibility is $\chi^{(2)} = 10^{-3}\omega$. The interaction strength between the MNS-QE is taken as $f = 0.1\omega$. For the source that drives the QE, the strength value is taken as $\varepsilon_{\mathrm{p}} = 0.01\omega$. If the wavelength of the incident field is taken around $\sim$550 nm in the visible optical region, $\varepsilon_{\mathrm{p}} = 10^{-2}\omega$ can be approximated around 2meV, while $\varepsilon_{\mathrm{p}} = 10^{-5}\omega$ would be around 0.002meV. The second harmonic signal is enhanced around 1500 factors when the QE level spacing is resonant with the higher energy plasmon mode Ω_2. As the SH converted photons reaches to the maximum entangle-

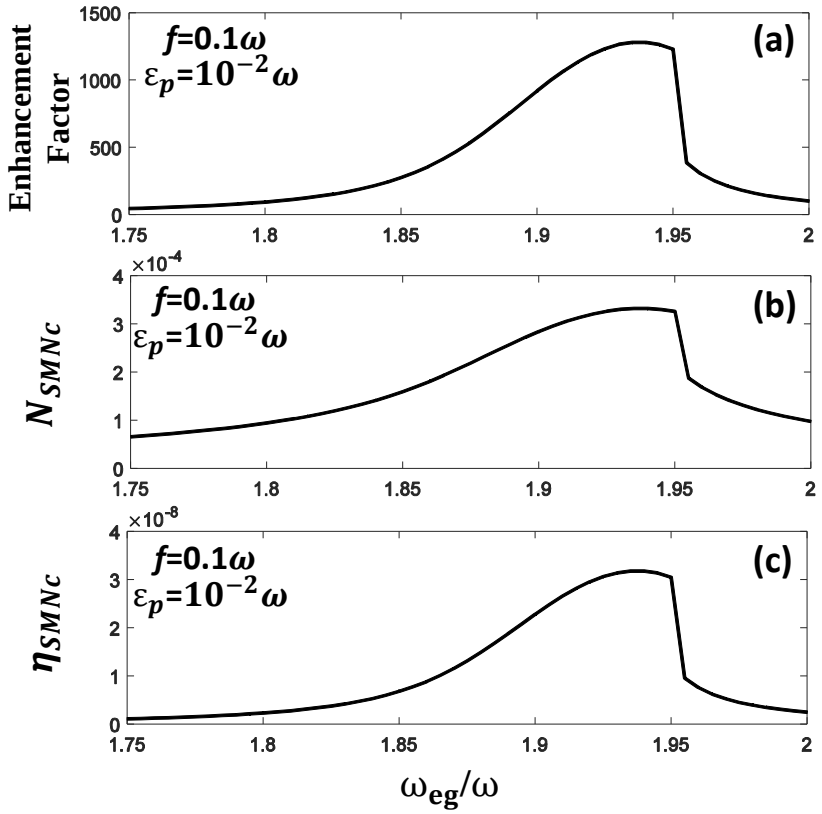

Figure 4.2: (a) The enhancement factor of the SH converted photons with respect to the different level spacing values of the QE. Corresponding (b) nonclassicality measure $\mathcal{N}_{\mathrm{SMNc}}$ and (c) nonclassicality witness η_{SMNc} are presented. Here, all the parameters are given in proportion with the incident light that stimulates $\hat{a}$-mode of the plasmonic structure with the frequency ω. The MNS supports the SH mode at $\Omega_2 = 1.9\omega$ and the second order susceptibility is taken as $\chi^{(2)} = 10^{-3}\omega$. The interaction strength between the MNS-QE is taken as $f = 0.1\omega$. The strength of the source that drives the $\hat{a}$-mode is $\varepsilon_{\mathrm{s}} = 10^{-2}\omega$. The pumping strength for the source that drives the QE is also determined as $\varepsilon_{\mathrm{p}} = 10^{-2}\omega$. It can be observed that at the region where SH converted photons reach their maximum enhancement around $\Omega_2 = 1.9\omega$, both of the nonclassicality measure and witness reveal the same form of increment. This indicates that the presented enhancement around 10^3 factors occurs as a result of the nonlinear path interference phenomenon.

ment point, it can be observed from Fig. (4.2) (b) - (c) that both the nonclassicality measure $\mathcal{N}_{\mathrm{SMNc}}$ and the nonclassicality witness η_{SMNc} also reaches their maximum value. They possess the same form as the enhancement factor. The simultaneous enhancement of α_2 photons with the nonclassicality measure $\mathcal{N}_{\mathrm{SMNc}}$ implies that the presented enhancement factor is a result of the nonlinear path interference effects. In other words, the nonlinear process that occurs in the coupled system increases the nonclassicality while providing energy from outside of the system cannot have this effect on its own. In Fig. (4.2) (c) the nonclassicality witness η_{SMNc} is presented whose positive value indicates the presence of entanglement between two-mode states.

Besides the 3 orders of magnitude enhancement in the SH signal when the QE pump strength is $\varepsilon_{\mathrm{p}} = 10^{-2}\omega$, the same effect also take place when the pumping source is reduced to $\varepsilon_{\mathrm{p}} = 10^{-5}\omega$. Even with very small driving voltage for QE, the nonlinear process can be increased around $\sim$100 factors.

One might raise the question that how the interaction strength between MNS-QE affects the tuning of Fano resonance in the system. In Figs. (4.4) and (4.5), the interaction strength is decreased to $f = 0.05\omega$. The QE pump source have a strength of $\varepsilon_{\mathrm{p}} = 10^{-2}\omega$ in Fig. (4.4) and $\varepsilon_{\mathrm{p}} = 10^{-4}\omega$ in Fig. (4.5). All the other parameters are kept the same to that of previous figures. The enhancement of SH response and the corresponding increase in the nonclassicality measure is still present, although the maximum enhancement values are decreased as a result of decreasing the interaction strength.

It is important to note that even when the interaction amount and the QE pump strength is reduced orders of magnitude, the enhancement of the nonlinear process is still present in the system. It can be observed that the QE level spacing values that generate SH enhancement is in the range of $\omega_{\mathrm{eg}} = 1.8$ - $2.0\,\omega$. In experimental means, it is not possible to implement quantum emitter structures with exact level spacing values to predetermined positions with respect to the MNS by sustaining certain interaction amounts. Figs. (4.2) - (4.5) represents that with having a bunch of molecules which have alternating level spacing values, even the molecules that interact less with the plasmonic structure can contribute to the overall nonlinear enhancement.

Furthermore, the effect of QE pump strength can be observed in Figs. (4.6) and (4.7).

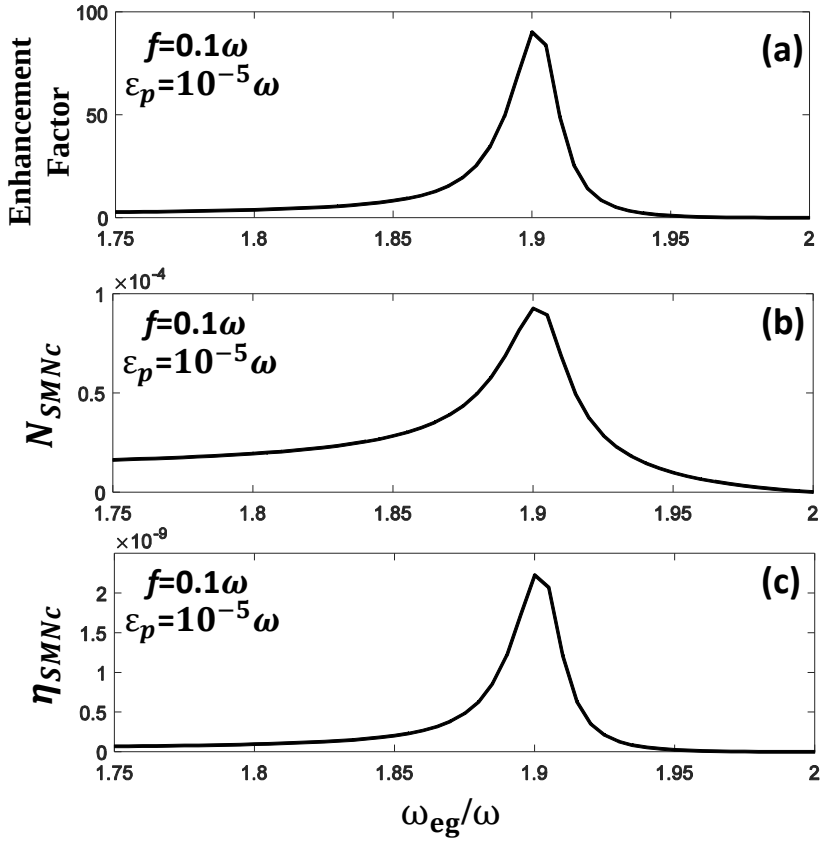

Figure 4.3: (a) The amount of enhancement in the SH converted plasmon mode is presented. The pumping strength of the QE is decreased 3 orders of magnitude compared to Fig. (4.2), becoming $\varepsilon_{\rm p} = 10^{-5}\omega$. The other parameters are kept the same as; $\Omega_2 = 1.9\omega$, $\chi^{(2)} = 10^{-3}\omega$, $\varepsilon_{\rm s} = 10^{-2}\omega$ and $f = 0.05\omega$. (b) The nonclassicality measure $\mathcal{N}_{\rm SMNc}$ and (c) nonclassicality witness $\eta_{\rm SMNc}$ increase in the same trend with the SH converted plasmon mode, implying that the enhancement phenomenon accommodate nonlinear effects. With decreasing the QE pump strength, the maximum enhancement factor decreased to $\sim 10^2$.

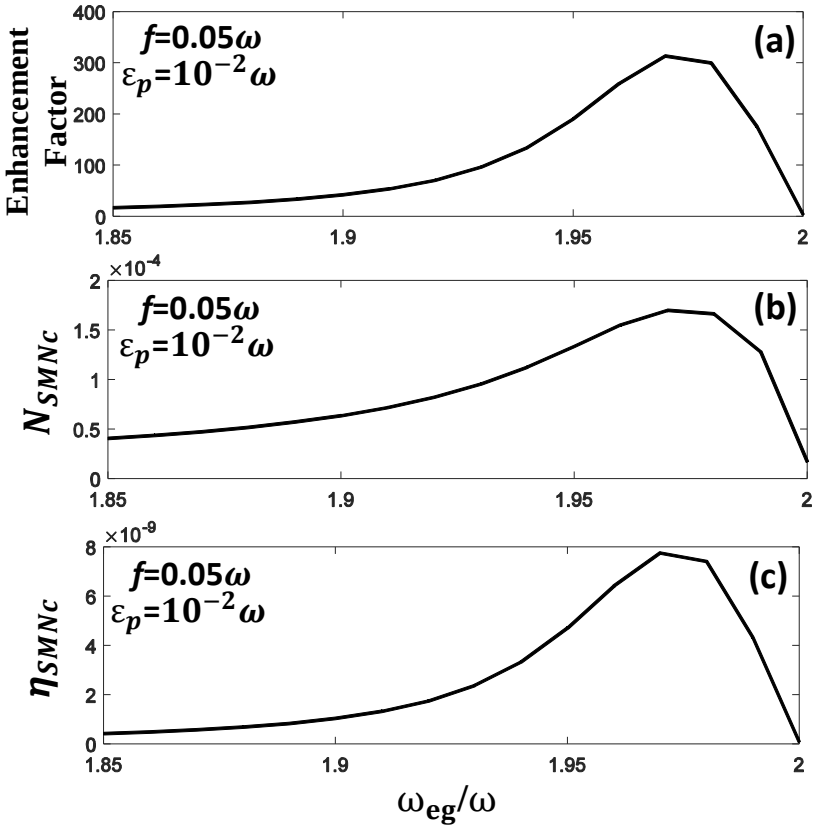

Figure 4.4: (a) The SH enhancement factor is presented along with the (b) nonclassicality measure $\mathcal{N}_{\mathrm{SMNc}}$ and (c) SPH nonclassicality witness η_{SMNc}. The interaction strength between MNS-QE, $f = 0.05\omega$ is reduced to half compared to that of Figs. (4.2) and (4.3). All other parameters are unchanged as follows; $\Omega_2 = 1.9\omega$, $\chi^{(2)} = 10^{-3}\omega$ and $\varepsilon_{\mathrm{s}} = 10^{-2}\omega$. Similar to previous figures, (b) the nonclassicality measure $\mathcal{N}_{\mathrm{SMNc}}$ and (c) nonclassicality witness η_{SMNc} also increase with increasing SH response. This implies the presence of path interference effects in the enhancement process. Comparing to the case where the interaction strength is higher as $f = 0.1\omega$, the maximum enhancement value is decreased an order of magnitude when the interaction is reduced.

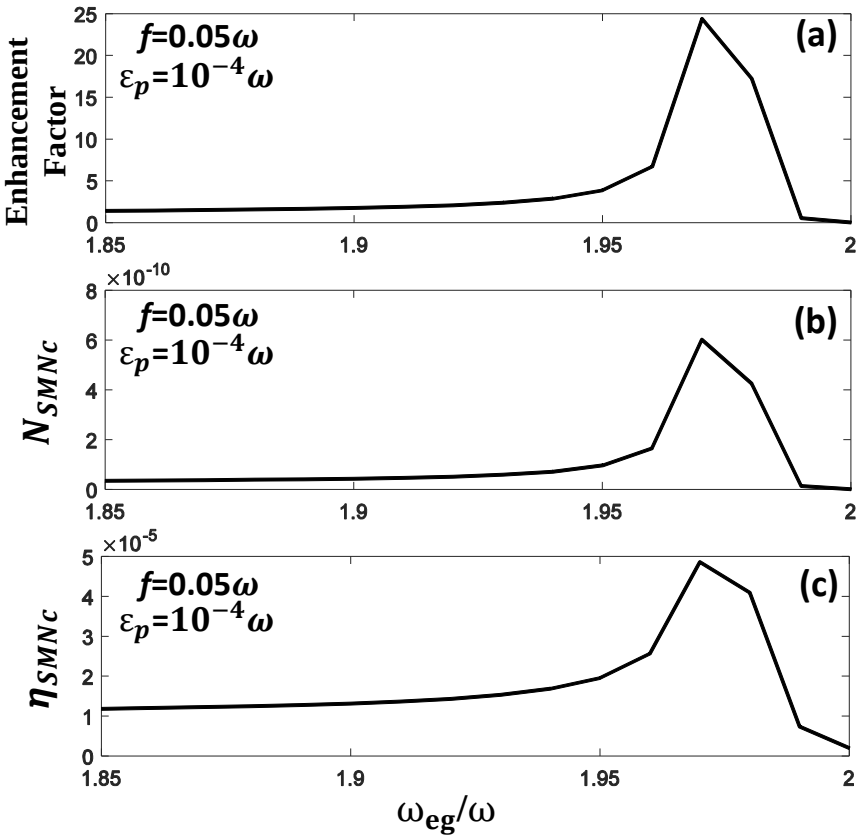

Figure 4.5: (a) The results of enhancement in the SH signal where the QE pump strength is $\varepsilon_{\rm s} = 10^{-4}\omega$ and the interaction strength is $f = 0.05\omega$. (b), (c) The nonclassicality measurement and witness denote that path interference effects take place. Since both the interaction strength and the QE pump strength is taken relatively very small, the maximum enhancement factor is around 25, however this implies that even when the interaction is very small, the SH signal can be altered due to the presence of Fano resonance.

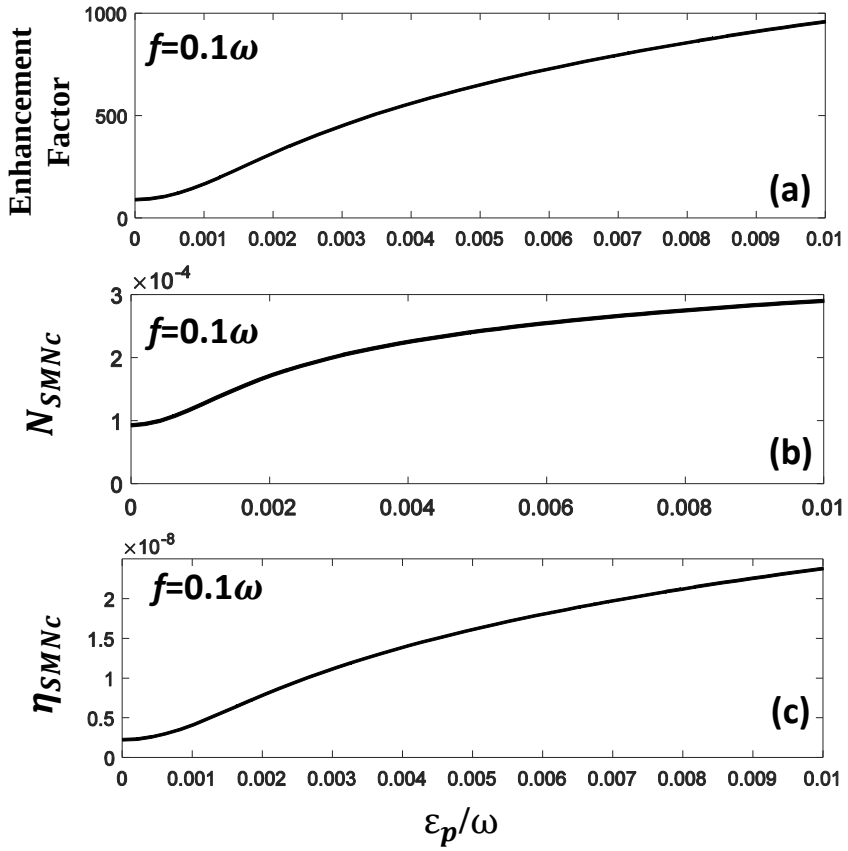

Figure 4.6: (a) The SH converted field enhancement with respect to the QE pump strength value. As the pump strength is increased, the enhancement factor also increases. The parameters are taken the same as Figs. (4.2) and (4.3). (b)-(c) The corresponding nonclassicality measure and witness indicate the presence of nonlinear processes. At the values greater than $\varepsilon_{\rm p} = 0.01\omega$, the system do not reach a steady-state.

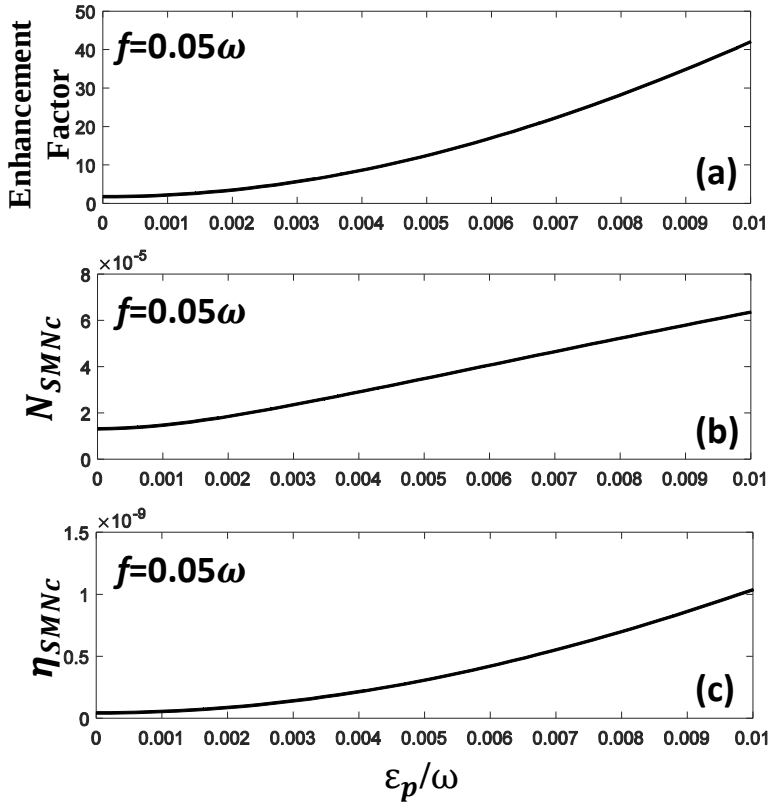

Figure 4.7: (a) The enhancement results with respect to the QE pump strength are presented with reduced interaction value of $f = 0.05\omega$. Since the MNS-QE interaction is small compared to Fig. (4.6), the maximum enhancement factor is also reduced. However, by observing nonclassicality measure and witness in (b) and (c), it can be acknowledged that although it is mostly reduced, the SH response can still be manipulated as a result of path interference.

When the interaction strength is $f = 0.1\omega$ in Fig. (4.6), nonlinear enhancement is increased 3 orders of magnitude with increasing pump strength. Even when the QE molecules interact less with the plasmonic structure, the SH converted signal can slightly be enhanced. These results imply that even when the interaction strength between MNS-QE is small compared to the incident field strength, one can obtain enhanced SH signal at least an order of magnitude with appropriate pumping of the QE. The nonclassicality measure $\mathcal{N}_{\mathrm{SMNc}}$ and nonclassicality witness η_{SMNc} for both results imply that path interference effects played a part in the enhancement process.

In this chapter, the enhancement of SH converted nonlinear response of a coupled MNS-QE system is demonstrated. The SH response of the system is examined through a simple theoretical model, followed by the formulation of nonclassicality measure and witness in terms of the input single-mode state variances. By utilizing these treatments, the quantity of single-mode nonclassicality along with the photon density of the SH converted plasmon mode is presented. When the QE is pumped with a voltage source, the SH response alters. Since the amount of nonclassicality in the system is observed to increase, it is important to acknowledge the source of this enhancement process. The main aim is to understand whether the presented SH enhancement is really result form the path interference effects, or is it just the consequence of providing energy to the system by the QE pump. In Figs. (4.2) - (4.7) it is demonstrated that the generated enhancement occurs by means of nonlinear processes. In all of the figures, the (b) nonclassicality measure $\mathcal{N}_{\mathrm{SMNc}}$ and (c) the nonclassicality witness η_{SMNc} are presented along with the SH conversion enhancement results. Since $\mathcal{N}_{\mathrm{SMNc}}$ is a measure that quantifies the nonclassicality, it can be acknowledged that the nonclassicality of the system increases simultaneously with the emerging nonlinear signal. This implies that path interference effects play a role in the emergence of the SH enhancement.

CHAPTER 5

CONCLUSION AND REMARKS

The nonlinear responses of plasmonic metal nanostructures (MNS) are revealed as the incident light is confined in nm-size dimensions through the MNS hot spots. This confinement of light, combined with the path interference effects introduced by the Fano mechanism, enables one to control and manipulate the nonlinear responses of the system in many ways. Fano resonance occurs when a structure with a response in the shape of a continuum (a gold nanoparticle, for instance) interacts with a discrete state, such as a quantum emitter. The aim of this study is to analytically understand the effect of path interference on nonlinear responses for coupled MNS-QE systems. In Chapter 3, the surface enhanced Raman scattering (SERS) response of a MNS-QE system is examined to introduce a new enhancement mechanism which does not alter the hot spot fields. In Chapter 4, the nonclassicality of the emerged SH signal of a coupled MNS-QE system is investigated. The beam splitter approach is utilized in order to obtain a nonclassicality measure, $\mathcal{N}_{\mathrm{SMNc}}$ and a nonclassicality witness, η_{SMNc}.

Chapter 2 provided an introduction on the surface plasmon resonances and the nonlinear plasmonics. The specific types of nonlinear responses that are studied in this thesis are surface enhanced Raman scattering (SERS) and second harmonic generation (SHG). Continuing with the introduction, Fano resonances are described both in linear and nonlinear responses for plasmonic structures.

Chapter 3 introduced a new enhancement mechanism that occurs as a result of path interference between a gold MNS and a QE. A double-resonance scheme is adopted for the gold MNS where the QE is represented by a discrete state. The equations of motion that describes the dynamics of the system is obtained. In the analytical ap-

proach, the steady-state solutions are used to obtain the simple equation, Eq. (3.16), that provides insight on how the path interference affects the enhancement and suppression of the SERS signal. The enhancement factors that are presented in the results are defined with respect to the different level spacing values of the QE, ω_{eg}. In other words, the enhancement factor is the ratio of the Raman mode intensity with and without the presence of the QE. Moreover, the results are further examined in detail to demonstrate how the MNS-QE coupling strength f has an influence on the system. Furthermore, the response of the system with respect to different parameters is presented in order to gain further understanding. Also, the coupling of a long-live dark plasmon mode instead of a discrete structure, such as the QE is presented. The similar enhancement and suppression phenomenon is observed in that case.

Besides the analytical treatment, the 3D simulations of Maxwell equations are also studied. The purpose of utilizing 3D simulations are to understand if the retardation effects wash out the results of analytical treatment. The conclusions from Chapter 3 can be listed as follows;

(i) According to analytical results, as the coupling strength of MNS-QE, f, increases, the peak of the maximum enhancement shifts to the longer wavelengths of the QE level spacing. It is of importance to stress that the presented increment in the SH signal adds up to the enhancement that occurs because of localization in the MNS. The localization of excited and Stokes-shifted plasmon hot spots can already provide an enhancement around 10^8 factors. The extra enhancement around $\sim$ 300 factors that is presented in Fig. 3.3, is an additional element that multiplies with the localized hot spot enhancement, making a total around 10^{10} factors. This type of enhancement is beneficial for systems that operate in the breakdown limit or tunneling regime as well as for the imaging of fragile molecules at strong electromagnetic fields.

(ii) By observing Eq. (3.16), it is acknowledged that the suppression of the SERS signal is also possible when the QE is resonant with the Raman-shifted mode of the plasmonic system. A suppression around 10^{-10} factors can be possible.

(iii) The results of the 3D simulations agree well with the analytical results. As can be seen in Fig. 3.8, when the retardation effects are taken into account, the enhancement bands tend to narrow into very small wavelength shifts of QE level spacing. However,

the aim of 3D simulations is not to reproduce exactly the same results with analytical treatment. The purpose here is to see whether the path interference effects are washed out by the impacts of retardation. It is observed that path interference effects are still present in 3D simulations and an enhancement factor around 5000 can be achieved with certain amount of coupling, f.

(iv) Furthermore, another significant result of the analytical treatment is that the phenomenon of path interference is also present when the plasmonic system is coupled to a longer-live object, such as a dark plasmonic mode. Analytically, an enhancement factor around 200 is observed when the system is coupled to long lifetime object.

Proceeding ahead to Chapter 4, the nonclassicality features of the SH response from a coupled double-resonant MNS-QE system is studied. The aim here is to understand the effect of path interference on the nonclassicality and entanglement properties that is brought to the system by the presence of QE. The phenomenon of entanglement is now at the heart of quantum mechanics and quantum information processing theory. Linear transformations such as beam splitting operators, produce two-mode entangled states at the output, provided that the input state is a nonclassical one.

One of the approaches brought up by Asboth et al., associates the degree of nonclassicality of the input single state with its ability to produce two-mode entangled states at the output of a beam splitter like operator. The nonclassical single state $|\Psi_{\mathrm{Ncl}}\rangle$ is defined in terms of the coherent states. An analytical approach similar to that is presented in Chapter 3 is used for SHG in a double-resonance scheme. Furthermore, the covariance matrix is defined for a Gaussian state in terms of 2×2 matrices whose elements can be calculated numerically. The nonclassicality of the SH converted signal can be determined in terms of the variances in the single-mode input state. By using the invariants derived from the covariance matrix, the symplectic eigenvalues are defined implying the condition that for a partially transpose state the separability condition requires that either one of the symplectic eigenvalues are greater than $1/2$. Since ν_- is always smaller than ν_+, the entanglement measure becomes $E_N = \max(0, -\log(2\nu_-))$, referred as the logarithmic negativity. $\mathcal{N}_{\mathrm{SMNc}}$ is defined as the nonclassicality measure, arise when the logarithmic negativity reaches its maximum value. Besides the logarithmic value, another nonclassicality witness η_{SMNc}

is utilized from the SPH criterion, λ_{Simon}. The significance of the nonclassicality witness lies in the fact that it can also be used for non-Gaussian states too.

The purpose of utilizing the nonclassicality measure and witness is to acknowledge whether the presented enhancement is really result form the path interference effects, or is it just the consequence of providing energy to the system by the QE pumping source. In Figs. (4.2) - (4.7), it is demonstrated that as the emerging SH signal enhances, the nonclassicality measure $\mathcal{N}_{\mathrm{SMNc}}$ shows the same trend of increase simultaneously. Since $\mathcal{N}_{\mathrm{SMNc}}$ is a measure to quantify the nonclassicality, it can be said that the nonlinear signal have increasing nonclassical features in the regions of enhancement. This implies that path interference effects play a role in the emergence of the SH signal enhancement in the coupled MNS-QE system. In other words, the nonlinear response of the system can be manipulated by driving the QE with a small source, utilizing the Fano resonance mechanism.

REFERENCES

[1] Harry A Atwater. The promise of plasmonics. *Scientific American*, 296(4):56–63, 2007.

[2] Paul R West, Satoshi Ishii, Gururaj V Naik, Naresh K Emani, Vladimir M Shalaev, and Alexandra Boltasseva. Searching for better plasmonic materials. *Laser & Photonics Reviews*, 4(6):795–808, 2010.

[3] Mark S Tame, KR McEnery, ŞK Özdemir, Jinhyoung Lee, Stefan A Maier, and MS Kim. Quantum plasmonics. *Nature Physics*, 9(6):329–340, 2013.

[4] Pierre Berini and Israel De Leon. Surface plasmon–polariton amplifiers and lasers. *Nature photonics*, 6(1):16–24, 2012.

[5] Jeffrey N Anker, W Paige Hall, Olga Lyandres, Nilam C Shah, Jing Zhao, and Richard P Van Duyne. Biosensing with plasmonic nanosensors. In *Nanoscience and Technology: A Collection of Reviews from Nature Journals*, pages 308–319. World Scientific, 2010.

[6] Mark I Stockman. Nanoplasmonics: past, present, and glimpse into future. *Optics express*, 19(22):22029–22106, 2011.

[7] Martti Kauranen and Anatoly V Zayats. Nonlinear plasmonics. *Nature photonics*, 6(11):737–748, 2012.

[8] Amanda J Haes, Christy L Haynes, Adam D McFarland, George C Schatz, Richard P Van Duyne, and Shengli Zou. Plasmonic materials for surface-enhanced sensing and spectroscopy. *MRS bulletin*, 30(5):368–375, 2005.

[9] Patrice Genevet, Jean-Philippe Tetienne, Evangelos Gatzogiannis, Romain Blanchard, Mikhail A Kats, Marlan O Scully, and Federico Capasso. Large enhancement of nonlinear optical phenomena by plasmonic nanocavity gratings. *Nano letters*, 10(12):4880–4883, 2010.

[10] Boris Luk'yanchuk, Nikolay I Zheludev, Stefan A Maier, Naomi J Halas, Peter Nordlander, Harald Giessen, and Chong Tow Chong. The fano resonance in plasmonic nanostructures and metamaterials. *Nature materials*, 9(9):707–715, 2010.

[11] Mehmet Emre Taşgın, Alpan Bek, and Selen Postacı. Fano resonances in the linear and nonlinear plasmonic response. In *Fano Resonances in Optics and Microwaves*, pages 1–31. Springer, 2018.

[12] Mehmet Emre Taşgın. Metal nanoparticle plasmons operating within a quantum lifetime. *Nanoscale*, 5(18):8616–8624, 2013.

[13] Yizhuo Chu, Mohamad G Banaee, and Kenneth B Crozier. Double-resonance plasmon substrates for surface-enhanced raman scattering with enhancement at excitation and stokes frequencies. *ACS nano*, 4(5):2804–2810, 2010.

[14] Niclas S Mueller, Sebastian Heeg, and Stephanie Reich. Surface-enhanced raman scattering as a higher-order raman process. *Physical Review A*, 94(2):023813, 2016.

[15] Ado Jorio, Niclas S Mueller, and Stephanie Reich. Symmetry-derived selection rules for plasmon-enhanced raman scattering. *Physical Review B*, 95(15):155409, 2017.

[16] Bhavya Sharma, Renee R Frontiera, Anne-Isabelle Henry, Emilie Ringe, and Richard P Van Duyne. Sers: Materials, applications, and the future. *Materials today*, 15(1-2):16–25, 2012.

[17] Yu Zhang, Yu-Rong Zhen, Oara Neumann, Jared K Day, Peter Nordlander, and Naomi J Halas. Coherent anti-stokes raman scattering with single-molecule sensitivity using a plasmonic fano resonance. *Nature communications*, 5(1):1–7, 2014.

[18] Renhe Zhang, Yao Zhang, ZC Dong, S Jiang, C Zhang, LG Chen, L Zhang, Y Liao, J Aizpurua, Y ea Luo, et al. Chemical mapping of a single molecule by plasmon-enhanced raman scattering. *Nature*, 498(7452):82–86, 2013.

[19] Taka-aki Yano, Yasushi Inouye, and Satoshi Kawata. Nanoscale uniaxial pressure effect of a carbon nanotube bundle on tip-enhanced near-field raman spectra. *Nano letters*, 6(6):1269–1273, 2006.

[20] Chris B Schaffer, Andre Brodeur, and Eric Mazur. Laser-induced breakdown and damage in bulk transparent materials induced by tightly focused femtosecond laser pulses. *Measurement Science and Technology*, 12(11):1784, 2001.

[21] Wenqi Zhu and Kenneth B Crozier. Quantum mechanical limit to plasmonic enhancement as observed by surface-enhanced raman scattering. *Nature communications*, 5(1):1–8, 2014.

[22] Otfried Gühne and Géza Tóth. Entanglement detection. *Physics Reports*, 474(1-6):1–75, 2009.

[23] Martin B Plenio and Shashank S Virmani. An introduction to entanglement theory. *Quantum information and coherence*, pages 173–209, 2014.

[24] Mehmet Emre Tasgin. Measuring nonclassicality of single-mode systems. *Journal of Physics B: Atomic, Molecular and Optical Physics*, 53(17):175501, 2020.

[25] MS Kim, W Son, Vladimír Bužek, and PL Knight. Entanglement by a beam splitter: Nonclassicality as a prerequisite for entanglement. *Physical Review A*, 65(3):032323, 2002.

[26] Wang Xiang-Bin. Theorem for the beam-splitter entangler. *Physical Review A*, 66(2):024303, 2002.

[27] Y Aharonov, D Falkoff, E Lerner, and H Pendleton. A quantum characterization of classical radiation. *Annals of Physics*, 39(3):498–512, 1966.

[28] János K Asbóth, John Calsamiglia, and Helmut Ritsch. Computable measure of nonclassicality for light. *Physical review letters*, 94(17):173602, 2005.

[29] W Vogel and J Sperling. Unified quantification of nonclassicality and entanglement. *Physical Review A*, 89(5):052302, 2014.

[30] Mark L Brongersma and Pieter G Kik. *Surface plasmon nanophotonics*, volume 131. Springer, 2007.

[31] Kathryn M Mayer and Jason H Hafner. Localized surface plasmon resonance sensors. *Chemical reviews*, 111(6):3828–3857, 2011.

[32] Katherine A Willets and Richard P Van Duyne. Localized surface plasmon resonance spectroscopy and sensing. *Annu. Rev. Phys. Chem.*, 58:267–297, 2007.

[33] JM Pitarke, VM Silkin, EV Chulkov, and PM Echenique. Theory of surface plasmons and surface-plasmon polaritons. *Reports on progress in physics*, 70(1):1, 2006.

[34] Eliza Hutter and Janos H Fendler. Exploitation of localized surface plasmon resonance. *Advanced materials*, 16(19):1685–1706, 2004.

[35] Eleonora Petryayeva and Ulrich J Krull. Localized surface plasmon resonance: Nanostructures, bioassays and biosensing—a review. *Analytica chimica acta*, 706(1):8–24, 2011.

[36] Joseph M Luther, Prashant K Jain, Trevor Ewers, and A Paul Alivisatos. Localized surface plasmon resonances arising from free carriers in doped quantum dots. *Nature materials*, 10(5):361–366, 2011.

[37] Jeremy Butet, Pierre-Francois Brevet, and Olivier JF Martin. Optical second harmonic generation in plasmonic nanostructures: from fundamental principles to advanced applications. *ACS nano*, 9(11):10545–10562, 2015.

[38] Catalin C Neacsu, Georg A Reider, and Markus B Raschke. Second-harmonic generation from nanoscopic metal tips: Symmetry selection rules for single asymmetric nanostructures. *Physical Review B*, 71(20):201402, 2005.

[39] Krishnan Thyagarajan, Simon Rivier, Andrea Lovera, and Olivier JF Martin. Enhanced second-harmonic generation from double resonant plasmonic antennae. *Optics express*, 20(12):12860–12865, 2012.

[40] Hayk Harutyunyan, Giorgio Volpe, Romain Quidant, and Lukas Novotny. Enhancing the nonlinear optical response using multifrequency gold-nanowire antennas. *Physical review letters*, 108(21):217403, 2012.

[41] Cristian Ciraci, Ekaterina Poutrina, Michael Scalora, and David R Smith. Second-harmonic generation in metallic nanoparticles: Clarification of the role of the surface. *Physical Review B*, 86(11):115451, 2012.

[42] Gregory A Wurtz, Robert Pollard, Willam Hendren, GP Wiederrecht, DJ Gosztola, VA Podolskiy, and Anatoly V Zayats. Designed ultrafast optical nonlinearity in a plasmonic nanorod metamaterial enhanced by nonlocality. *Nature nanotechnology*, 6(2):107–111, 2011.

[43] Krishnan Thyagarajan, Jeremy Butet, and Olivier JF Martin. Augmenting second harmonic generation using fano resonances in plasmonic systems. *Nano letters*, 13(4):1847–1851, 2013.

[44] Martin Fleischmann, Patrick J Hendra, and A James McQuillan. Raman spectra of pyridine adsorbed at a silver electrode. *Chemical physics letters*, 26(2):163–166, 1974.

[45] Robin R Jones, David C Hooper, Liwu Zhang, Daniel Wolverson, and Ventsislav K Valev. Raman techniques: fundamentals and frontiers. *Nanoscale research letters*, 14(1):1–34, 2019.

[46] Fl J García-Vidal and JB Pendry. Collective theory for surface enhanced raman scattering. *Physical Review Letters*, 77(6):1163, 1996.

[47] Alan Campion and Patanjali Kambhampati. Surface-enhanced raman scattering. *Chemical society reviews*, 27(4):241–250, 1998.

[48] Katrin Kneipp, Yang Wang, Harald Kneipp, Lev T Perelman, Irving Itzkan, Ramachandra R Dasari, and Michael S Feld. Single molecule detection using surface-enhanced raman scattering (sers). *Physical review letters*, 78(9):1667, 1997.

[49] Janina Kneipp, Harald Kneipp, and Katrin Kneipp. Sers-A single-molecule and nanoscale tool for bioanalytics. *Chemical Society Reviews*, 37(5):1052–1060, 2008.

[50] Jiao Cao, Hai-Ling Liu, Jin-Mei Yang, Zhong-Qiu Li, Dong-Rui Yang, Li-Na Ji, Kang Wang, and Xing-Hua Xia. Sers detection of nucleobases in single silver plasmonic nanopores. *ACS sensors*, 5(7):2198–2204, 2020.

[51] Ximei Qian, Xiang-Hong Peng, Dominic O Ansari, Qiqin Yin-Goen, Georgia Z Chen, Dong M Shin, Lily Yang, Andrew N Young, May D Wang, and Shuming Nie. In vivo tumor targeting and spectroscopic detection with surface-enhanced raman nanoparticle tags. *Nature Biotechnology*, 26(1):83–90, 2008.

[52] Andrey E Miroshnichenko, Sergej Flach, and Yuri S Kivshar. Fano resonances in nanoscale structures. *Reviews of Modern Physics*, 82(3):2257, 2010.

[53] Ugo Fano. Sullo spettro di assorbimento dei gas nobili presso il limite dello spettro d'arco. *Il Nuovo Cimento (1924-1942)*, 12(3):154–161, 1935.

[54] Ugo Fano. Effects of configuration interaction on intensities and phase shifts. *Physical Review*, 124(6):1866, 1961.

[55] Mohsen Rahmani, Boris Luk'yanchuk, and Minghui Hong. Fano resonance in novel plasmonic nanostructures. *Laser & Photonics Reviews*, 7(3):329–349, 2013.

[56] Ulrich Hohenester and Andreas Trügler. Mnpbem–a matlab toolbox for the simulation of plasmonic nanoparticles. *Computer Physics Communications*, 183(2):370–381, 2012.

[57] Yong S Joe, Arkady M Satanin, and Chang Sub Kim. Classical analogy of fano resonances. *Physica Scripta*, 74(2):259, 2006.

[58] BC Yıldız Karakul. Enhancement of plasmonic nonlinear conversion and polarization lifetime via fano resonances. *Middle East Technical University*, 2017.

[59] Yang Yang, John M Callahan, Tong-Ho Kim, April S Brown, and Henry O Everitt. Ultraviolet nanoplasmonics: a demonstration of surface-enhanced raman spectroscopy, fluorescence, and photodegradation using gallium nanoparticles. *Nano letters*, 13(6):2837–2841, 2013.

[60] Selen Postaci, Bilge Can Yildiz, Alpan Bek, and Mehmet Emre Tasgin. Silent enhancement of sers signal without increasing hot spot intensities. *Nanophotonics*, 7(10):1687–1695, 2018.

[61] Nicolai B Grosse, Jan Heckmann, and Ulrike Woggon. Nonlinear plasmon-photon interaction resolved by k-space spectroscopy. *Physical Review Letters*, 108(13):136802, 2012.

[62] Deniz Turkpence, Gursoy B Akguc, Alpan Bek, and Mehmet Emre Tasgin. Engineering nonlinear response of nanomaterials using fano resonances. *Journal of Optics*, 16(10):105009, 2014.

[63] Yih Horng Tan, Maozi Liu, Birte Nolting, Joan G Go, Jacquelyn Gervay-Hague, and Gang-yu Liu. A nanoengineering approach for investigation and regulation of protein immobilization. *ACS nano*, 2(11):2374–2384, 2008.

[64] Xiaohua Wu, Stephen K Gray, and Matthew Pelton. Quantum-dot-induced transparency in a nanoscale plasmonic resonator. *Optics express*, 18(23):23633–23645, 2010.

[65] Marlan O Scully and M Suhail Zubairy. Quantum optics, 1999.

[66] Malin Premaratne and Mark I Stockman. Theory and technology of spasers. *Advances in Optics and Photonics*, 9(1):79–128, 2017.

[67] Mikolaj K Schmidt, Ruben Esteban, Alejandro González-Tudela, Geza Giedke, and Javier Aizpurua. Quantum mechanical description of raman scattering from molecules in plasmonic cavities. *ACS nano*, 10(6):6291–6298, 2016.

[68] Philippe Roelli, Christophe Galland, Nicolas Piro, and Tobias J Kippenberg. Molecular cavity optomechanics as a theory of plasmon-enhanced raman scattering. *Nature nanotechnology*, 11(2):164–169, 2016.

[69] Jian Ye, Fangfang Wen, Heidar Sobhani, J Britt Lassiter, Pol Van Dorpe, Peter Nordlander, and Naomi J Halas. Plasmonic nanoclusters: near field properties of the fano resonance interrogated with sers. *Nano letters*, 12(3):1660–1667, 2012.

[70] Marco Finazzi and Franco Ciccacci. Plasmon-photon interaction in metal nanoparticles: second-quantization perturbative approach. *Physical Review B*, 86(3):035428, 2012.

[71] J Butet, G Bachelier, I Russier-Antoine, F Bertorelle, A Mosset, N Lascoux, C Jonin, E Benichou, and P-F Brevet. Nonlinear fano profiles in the optical second-harmonic generation from silver nanoparticles. *Physical Review B*, 86(7):075430, 2012.

[72] CL Garrido Alzar, MAG Martinez, and P Nussenzveig. Classical analog of electromagnetically induced transparency. *American Journal of Physics*, 70(1):37–41, 2002.

[73] Andreas Trügler and Ulrich Hohenester. Strong coupling between a metallic nanoparticle and a single molecule. *Physical Review B*, 77(11):115403, 2008.

[74] Andreas Trügler, Jean-Claude Tinguely, Joachim R Krenn, Andreas Hohenau, and Ulrich Hohenester. Influence of surface roughness on the optical properties of plasmonic nanoparticles. *Physical Review B*, 83(8):081412, 2011.

[75] Sebastian Gerber, Frank Reil, Ulrich Hohenester, Thomas Schlagenhaufen, Joachim R Krenn, and Alfred Leitner. Tailoring light emission properties of fluorophores by coupling to resonance-tuned metallic nanostructures. *Physical Review B*, 75(7):073404, 2007.

[76] Frank Reil, Ulrich Hohenester, Joachim R Krenn, and Alfred Leitner. Forster-type resonant energy transfer influenced by metal nanoparticles. *Nano letters*, 8(12):4128–4133, 2008.

[77] DM Koller, U Hohenester, A Hohenau, H Ditlbacher, F Reil, N Galler, FR Aussenegg, A Leitner, A Trügler, and JR Krenn. Superresolution moiré mapping of particle plasmon modes. *Physical review letters*, 104(14):143901, 2010.

[78] Sara D Costa, Cristiano Fantini, Ariete Righi, Alicja Bachmatiuk, Mark H Rümmeli, Riichiro Saito, and Marcos A Pimenta. Resonant raman spectroscopy on enriched 13 c carbon nanotubes. *Carbon*, 49(14):4719–4723, 2011.

[79] Mehmet Emre Tasgin, Ildar Salakhutdinov, Dania Kendziora, Musa Kurtulus Abak, Deniz Turkpence, Luca Piantanida, Ljiljana Fruk, Marco Lazzarino, and Alpan Bek. Fluorescence excitation by enhanced plasmon upconversion under

continuous wave illumination. *Photonics and Nanostructures-Fundamentals and Applications*, 21:32–43, 2016.

[80] Kotni Santhosh, Ora Bitton, Lev Chuntonov, and Gilad Haran. Vacuum rabi splitting in a plasmonic cavity at the single quantum emitter limit. *Nature Communications*, 7:ncomms11823, 2016.

[81] Mario Hentschel, Bernd Metzger, Bastian Knabe, Karsten Buse, and Harald Giessen. Linear and nonlinear optical properties of hybrid metallic–dielectric plasmonic nanoantennas. *Beilstein journal of nanotechnology*, 7:111, 2016.

[82] Gang L Liu, Yadong Yin, Siri Kunchakarra, Bipasha Mukherjee, Daniele Gerion, Stephen D Jett, David G Bear, Joe W Gray, A Paul Alivisatos, Luke P Lee, et al. A nanoplasmonic molecular ruler for measuring nuclease activity and dna footprinting. *Nature Nanotechnology*, 1(1):47, 2006.

[83] Steven J Barrow, Xingzhan Wei, Julia S Baldauf, Alison M Funston, and Paul Mulvaney. The surface plasmon modes of self-assembled gold nanocrystals. *Nature Communications*, 3:1275, 2012.

[84] Lingyan Meng, Tengxiang Huang, Xiang Wang, Shu Chen, Zhilin Yang, and Bin Ren. Gold-coated afm tips for tip-enhanced raman spectroscopy: theoretical calculation and experimental demonstration. *Optics express*, 23(11):13804–13813, 2015.

[85] Christiane Höppener, Zachary J Lapin, Palash Bharadwaj, and Lukas Novotny. Self-similar gold-nanoparticle antennas for a cascaded enhancement of the optical field. *Physical Review Letters*, 109(1):017402, 2012.

[86] Hui-Hsin Hsiao, Aimi Abass, Johannes Fischer, Rasoul Alaee, Andreas Wickberg, Martin Wegener, and Carsten Rockstuhl. Enhancement of second-harmonic generation in nonlinear nanolaminate metamaterials by nanophotonic resonances. *Optics express*, 24(9):9651–9659, 2016.

[87] Albert Einstein, Boris Podolsky, and Nathan Rosen. Can quantum-mechanical description of physical reality be considered complete? *Physical review*, 47(10):777, 1935.

[88] Jürgen Schlienz and Günter Mahler. Description of entanglement. *Physical Review A*, 52(6):4396, 1995.

[89] Artur K Ekert. Quantum cryptography based on bell's theorem. *Physical review letters*, 67(6):661, 1991.

[90] Klaus Mattle, Harald Weinfurter, Paul G Kwiat, and Anton Zeilinger. Dense coding in experimental quantum communication. *Physical Review Letters*, 76(25):4656, 1996.

[91] Marek Zukowski, Anton Zeilinger, Michael A Horne, and Aarthur K Ekert. " event-ready-detectors" bell experiment via entanglement swapping. *Physical Review Letters*, 71(26), 1993.

[92] Jian-Wei Pan, Dik Bouwmeester, Harald Weinfurter, and Anton Zeilinger. Experimental entanglement swapping: entangling photons that never interacted. *Physical review letters*, 80(18):3891, 1998.

[93] Charles H Bennett, Gilles Brassard, Claude Crépeau, Richard Jozsa, Asher Peres, and William K Wootters. Teleporting an unknown quantum state via dual classical and einstein-podolsky-rosen channels. *Physical review letters*, 70(13):1895, 1993.

[94] Dik Bouwmeester, Jian-Wei Pan, Klaus Mattle, Manfred Eibl, Harald Weinfurter, and Anton Zeilinger. Experimental quantum teleportation. *Nature*, 390(6660):575–579, 1997.

[95] J Solomon Ivan, S Chaturvedi, E Ercolessi, G Marmo, G Morandi, N Mukunda, and R Simon. Entanglement and nonclassicality for multimode radiation-field states. *Physical Review A*, 83(3):032118_1032118_20, 2011.

[96] Mark Hillery and M Suhail Zubairy. Entanglement conditions for two-mode states. *Physical review letters*, 96(5):050503, 2006.

[97] H Gholipour and F Shahandeh. Entanglement and nonclassicality: A mutual impression. *Physical Review A*, 93(6):062318, 2016.

[98] Clive Emary and Tobias Brandes. Chaos and the quantum phase transition in the dicke model. *Physical Review E*, 67(6):066203, 2003.

[99] Mehmet Emre Tasgin. Single-mode nonclassicality criteria via holstein-primakoff transformation. *arXiv preprint arXiv:1502.00988*, 2015.

[100] Rajiah Simon. Peres-horodecki separability criterion for continuous variable systems. *Physical Review Letters*, 84(12):2726, 2000.

[101] Mehmet Günay, Zafer Artvin, Alpan Bek, and Mehmet Emre Tasgin. Controlling steady-state second harmonic signal via linear and nonlinear fano resonances. *Journal of Modern Optics*, 67(1):26–34, 2020.

[102] A Ridolfo, O Di Stefano, N Fina, R Saija, and S Savasta. Quantum plasmonics with quantum dot-metal nanoparticle molecules: influence of the fano effect on photon statistics. *Physical review letters*, 105(26):263601, 2010.

[103] Arka Majumdar, Michal Bajcsy, Dirk Englund, and Jelena Vuckovic. All optical switching with a single quantum dot strongly coupled to a photonic crystal cavity. *IEEE Journal of Selected Topics in Quantum Electronics*, 18(6):1812–1817, 2012.

[104] Kevin Hennessy, Antonio Badolato, Martin Winger, D Gerace, Mete Atatüre, S Gulde, S Fält, Evelyn L Hu, and A Imamoğlu. Quantum nature of a strongly coupled single quantum dot–cavity system. *Nature*, 445(7130):896–899, 2007.

[105] Wei Wu, Dibyendu Dey, and Hooman Mohseni. A voltage tunable quantum dot photodetector for terahertz detection. *Journal of Physics D: Applied Physics*, 43(15):155101, 2010.

[106] JM Villas-Bôas, AO Govorov, and Sergio E Ulloa. Coherent control of tunneling in a quantum dot molecule. *Physical Review B*, 69(12):125342, 2004.

[107] Alexander Högele, Stefan Seidl, Martin Kroner, Khaled Karrai, Richard J Warburton, Brian D Gerardot, and Pierre M Petroff. Voltage-controlled optics of a quantum dot. *Physical review letters*, 93(21):217401, 2004.

[108] Chitraleema Chakraborty, Laura Kinnischtzke, Kenneth M Goodfellow, Ryan Beams, and A Nick Vamivakas. Voltage-controlled quantum light from an atomically thin semiconductor. *Nature nanotechnology*, 10(6):507–511, 2015.

[109] Parinda Vasa and Christoph Lienau. Strong light–matter interaction in quantum emitter/metal hybrid nanostructures. *Acs Photonics*, 5(1):2–23, 2018.

[110] Peter Lodahl, Sahand Mahmoodian, and Søren Stobbe. Interfacing single photons and single quantum dots with photonic nanostructures. *Reviews of Modern Physics*, 87(2):347, 2015.

[111] Raman A Shah, Norbert F Scherer, Matthew Pelton, and Stephen K Gray. Ultrafast reversal of a fano resonance in a plasmon-exciton system. *Physical Review B*, 88(7):075411, 2013.

[112] Bilge Can Yildiz, Mehmet Emre Tasgin, Musa Kurtulus Abak, Sahin Coskun, Husnu Emrah Unalan, and Alpan Bek. Enhanced second harmonic generation from coupled asymmetric plasmonic metal nanostructures. *Journal of Optics*, 17(12):125005, 2015.

[113] Bilge Can Yildiz, Alpan Bek, and Mehmet Emre Tasgin. Plasmon lifetime enhancement in a bright-dark mode coupled system. *Physical Review B*, 101(3):035416, 2020.

[114] Julien Laurat, Gaëlle Keller, José Augusto Oliveira-Huguenin, Claude Fabre, Thomas Coudreau, Alessio Serafini, Gerardo Adesso, and Fabrizio Illuminati. Entanglement of two-mode gaussian states: characterization and experimental production and manipulation. *Journal of Optics B: Quantum and Semiclassical Optics*, 7(12):S577, 2005.

[115] Matteo Brunelli, Claudia Benedetti, Stefano Olivares, Alessandro Ferraro, and Matteo GA Paris. Single-and two-mode quantumness at a beam splitter. *Physical Review A*, 91(6):062315, 2015.

[116] Guifré Vidal and Reinhard F Werner. Computable measure of entanglement. *Physical Review A*, 65(3):032314, 2002.

[117] Claudiu Genes, A Mari, P Tombesi, and D Vitali. Robust entanglement of a micromechanical resonator with output optical fields. *Physical Review A*, 78(3):032316, 2008.

CURRICULUM VITAE

PERSONAL INFORMATION

Surname, Name: Postacı, Selen
Nationality: Turkish
Date and Place of Birth: 28.11.1989, Ankara
Marital Status: Married with one child (2021)
Phone: +90 262 6753375
email: selen.postaci@tubitak.gov.tr

EDUCATION

Degree	Institution	Year of Graduation
M.Sc.	Department of Physics, METU	2013
B.S.	Department of Physics, METU	2011
High School	METU Development Foundation Schools	2007

WORK EXPERIENCE

Year	Place	Enrollment
2018-present	UEKAE, TUBITAK	Senior Researcher
2011-2018	Department of Physics, METU	Research Assistant

FOREIGN LANGUAGES

English (Advanced)

COMPUTER SKILLS

Languages Fortran 77, C and C++ (Beginner Level)
Tools Matlab, MS Office, LATEX, Origin, MNPBEM, Comsol Multiphysics
Platforms Unix, Linux, Windows

PUBLICATIONS

Proceedings Presented in National/International Meetings

1. S. Postacı, B.C. Yıldız, A. Bek, M.E. Taşgın, Fano Enhancement of Raman Conversion, Kuantum Optiği ve Bilişim Toplantısı (KOBİT 1), February 2-3 2017, İzmir, Turkey (Poster Presentation)

2. S. Postacı, B.C. Yıldız, A. Bek, M.E. Taşgın, Silent Enhancement of SERS with Unmodified Hot Spot Intensities, 19. Ulusal Optik, Elektro-Optik ve Fotonik Çalıştayı (FOTONİK 2017), September 29 2017, İstanbul, Turkey (Poster Presentation)

3. S. Postacı, B.C. Yıldız, A. Bek, M.E. Taşgın, Silent Enhancement of SERS with Unmodified Hot Spot Intensities, COST Action MP1403, Nanoscale Quantum Optics, ESR Workshop, 26-27 October 2017, Budapest, Hungary (Oral Presentation)

4. S. Postacı, B.C. Yıldız, A. Bek, M.E. Taşgın, Fano Enhancement of Plasmonic Raman Conversion, 25. İstatiksel Fizik Günleri (IFG 25), 28-30 June 2018, İzmir, Turkey (Oral Presentation)

International Journal Publications

1. Postaci, Selen, et al. "Silent enhancement of SERS signal without increasing hot spot intensities." Nanophotonics 7.10 (2018): 1687-1695.

2. Taşgın, Mehmet Emre, Alpan Bek, and Selen Postacı. "Fano resonances in the linear and nonlinear plasmonic response." Fano Resonances in Optics and Microwaves. Springer, Cham, 2018. 1-31.